The influence of complex volcanic vent morphology on eruption dynamics:

lessons learned from direct observation in field and laboratory

Dissertation von Markus Schmid

München 2022

The influence of complex volcanic vent morphology on eruption dynamics:

lessons learned from direct observation in field and laboratory

Dissertation
zur Erlangung des Grades eines Doktors
an der Fakultät für Geowissenschaften
der Ludwig-Maximilians-Universität München

eingereicht von
Markus Schmid

München, 06.09.2021

Erstgutachter/in:	Professor Dr. Donald B. Dingwell
Zweitgutachter/in:	PD Dr. Corrado Cimarelli
Tag der mündlichen Prüfung:	24.01.2022

Inhaltsverzeichnis

Abbildungsverzeichnis

Tabellenverzeichnis

Vorwort

Chapter 2 and 3 of this dissertation are published in peer reviewed journals. Chapter 4 is submitted to Bulletin of Volcanology. The content of these publications have not been altered for this dissertation but adapted for format and consistency of the overall thesis design. The full references of the published papers are the following:

Chapter 2

Schmid, M., U. Kueppers, R. Civico, T. Ricci, J. Taddeucci, and D. B. Dingwell (2021). Characterising vent and crater shape changes at Stromboli: implications for risk areas. Volcanica 4(1), 87-105. doi:https://doi.org/10.30909/vol.04.01.87105

Chapter 3

Schmid, M., U. Kueppers, V. Cigala, J. Sesterhenn, and D. B. Dingwell (2020). Release characteristics of overpressurised gas from complex vents: implications for volcanic hazards. Bulletin of Volcanology 82(11), 1-12. doi:https://doi.org/10.1007/s00445-020-01407-2

Chapter 4, submitted

Schmid, M., U. Kueppers, V. Cigala and D. B. Dingwell. Complex vent geometry and asymmetric particle ejection: experimental insights.

Contributions

During this doctoral project I made contributions to the following publications:

Civico, R., T. Ricci, P. Scarlato, D. Andronico, M. Cantarero, B. B. Carr, E. De Beni, E. Del Bello, J. B. Johnson, U. Kueppers, L. Pizzimenti, ***M. Schmid***, K. Strehlow, and J. Taddeucci (2021). Unoccupied Aircraft Systems (UASs) Reveal the Morphological Changes at Stromboli Volcano (Italy) before, between, and after the 3 July and 28 August 2019 Paroxysmal Eruptions. Remote Sensing 13(15), 2870.

Vossen C.E.J., C. Cimarelli, A. J. Bennett, ***M. Schmid***, U. Kueppers, T. Ricci, J. Taddeucci, D. B. Dingwell. Electrical activity and lightning during basaltic explosions at Stromboli volcano, Italy. (submitted).

Zusammenfassung

Vulkanausbrüche gelten als eine der spektakulärsten Naturgewalten unserer Erde. Gleichzeitig stellen sie jedoch auch eine Gefahr für die menschliche Gesundheit und Infrastruktur dar. Aufgrund ihrer Dynamik und ihres unberechenbaren Charakters geht von explosiven Vulkanausbrüchen eine besonders große Gefährdung des Menschen und seiner Umwelt aus. Im Zuge eines explosiven Ausbruchs werden heiße Gase und Pyroklasten in die Atmosphäre ausgeworfen. Obwohl das Monitoring aktiver Vulkane in den letzten Jahren immer weiter verbessert wurde, ist es immer noch schwierig eine konkrete Vorhersage zu den Ausbrüchen zu erstellen. Aufgrund ihrer Komplexität ist das Verhalten von Vulkanen nicht kalkulierbar. Bis heute ist weder eine Beobachtung, noch eine Messung der unterirdischen Rahmenbedingungen möglich, welche den Ausbruch steuern. Trotz dieser Unwägbarkeiten unterliegen Vulkanausbrüche dennoch physikalischen Gesetzmäßigkeiten, sodass die Möglichkeit besteht, die Prozesse im Untergrund eines Vulkans zu modellieren oder durch Experimente zu beschreiben. Aufgrund der Komplexität der Wechselwirkungen innerhalb des Systems Vulkan ist es erforderlich Experimente zunehmend realistischer zu gestalten.

Sobald das ausgeworfene Material aus dem Krater austritt können wir den Ausbruch visuell Beobachten. In diesem Bereich ist das Verhalten des Ausbruchs vollständig von den Prozessen im Untergrund und von der Geometrie des Kraters abhängig. Im Vergleich zu den symmetrischen Kraterformen, welche in Experimenten und Modellen oft angenommen werden, sind die Krater in der Natur deutlich unregelmäßiger geformt. Ihre Geometrien sind oft eingekerbt und haben eine schräge Oberfläche. Zudem können sich die Kratergeometrien innerhalb kürzester Zeit verändern. Um den Einfluss der Prozesse im Untergrund zu verstehen müssen wir zuerst den Einfluss der beobachtbaren Parameter (z. B. Kratergeometrie) ergründen. Schlussendlich wird ein tiefergehendes Verständnis der Parameter, die Vulkanausbrüche steuern, zu einem Fortschritt und der Verbesserung der Gefährdungsanalysen führen.

Um dies zu erreichen, habe ich Beobachtungen aus Feldkampagnen und Laborexperimenten kombiniert. Zunächst habe ich die Geometrien von Vulkankratern erfasst und deren zeitliche Entwicklung dokumentiert. Dazu haben ich die Geometrie der Krater in der Kraterterrasse des Strombolis in einer hohen Auflösung vermessen und die jeweils zugehörigen Explosionen beobachtet. Dabei konnte ich feststellen, dass sowohl die Intensität, als auch die Art und die Richtung der Ausbrüche durch Formveränderungen der Oberflächentopo-

grafie beeinflusst werden. Mittels Drohneneinsatz habe ich innerhalb eines Zeitraums von neun Monaten (Mai 2019–Januar 2020) fünf topografische Datensätze erstellt. In diesem Zeitraum war es möglich „normale“ Strombolianische Aktivität, starke Ausbrüche und sogar zwei Paroxysmen zu beobachten (3. Juli und 28. August 2019), sodass es möglich war, die verschiedenen Ausbruchstypen mit den vorherrschenden Ablagerungs- und Abtragungsprozessen zu verknüpfen. Zudem konnte ich die Anzahl der aktiven Krater, deren Positionen sowie deren Umgestaltung nachverfolgen. Da Veränderungen der Kratergeometrie und der Kraterposition auf eine Modifikation des Ausbruchsgeschehens hinweisen können, sind auch dies wichtige Faktoren für eine Gefährdungsanalyse. Die aus den Feldforschungen gewonnenen Daten zeigen deutlich die Komplexität, Vielseitigkeit und Variabilität der Formen vulkanischer Krater in einer nie dagewesenen zeitlichen und räumlichen Auflösung. Darüber hinaus haben die Beobachtungen der Vulkanausbrüche deutlich gemacht, wie stark die Beziehung zwischen dem Krater, der Kratergeometrie und dem Auswurf von pyroklastischem Material ist. Diese Erkenntnis hat eine große Bedeutung für die Gefährdungsanalyse, vor allem für Gebiete, die potentiell durch vulkanische Bomben und pyroklastischem Fallout bedroht sind.

Im Anschluss habe ich eine Reihe von Dekompressionsexperimenten mit Kratergeometrien durchgeführt, welche auf den Beobachtungen am Stromboli aufbauen. Durch diese Experimente wurde der Zusammenhang zwischen Kratergeometrie und Ausbruchsdynamik bestätigt. Die verwendeten Geometrien haben eine geneigte Oberfläche mit einem Winkel von 5°, 15° und 30° und jeweils einer zylindrischen und einer trichterförmigen inneren Geometrie. Daraus ergeben sich sechs experimentelle Krater die mit folgenden experimentellen Bedingungen getestet wurden: Vier unterschiedliche Startdrücke (5, 8, 15 und 25 MPa) und zwei Gasvolumina (127.4 cm^3, 31.9 cm^3). Alle Experimente wurden bei Raumtemperatur und mit Argon durchgeführt. Trotz des vertikalen Aufbaus konnte man auf beiden Seiten des Kraters unterschiedlich große Winkel des austretenden Gases beobachten. Weiterhin war der Gasstrahl geneigt. Die Richtung der Neigung wurde durch die innere Geometrie bestimmt. Bei einer zylindrischen Geometrie neigte sich der Gasstrahl in die Einfallsrichtung der geneigten Oberfläche. Im Falle einer trichterförmigen inneren Geometrie neigt sich der Gasstrahl entgegen der Einfallsrichtung. Der Winkel des Gasaustritts war bei einer zylindrischen inneren Geometrie immer größer als bei der trichterförmigen Geometrie. Sowohl die Winkel des Gasaustritts als auch die Neigung des Gasstrahls zeigten eine starke Reaktion auf eine Veränderung der Druckbedingung und Oberflächenneigung. Dabei zeigten sowohl der Austrittswinkel als auch die Neigung eine positive Korrelation mit dem Druck und der Oberflächenneigung. Hohe Druckbedingungen haben außerdem dafür gesorgt, dass für einen längeren Zeitraum Überdruckverhältnisse am Kraterausgang herrschten. Ein höheres Gasvolumen hat größere Gasaustrittswinkel ermöglicht.

Zuletzt habe ich die Dekompressionsexperimente durch den Einsatz von Partikeln ergänzt, um so den Auswurf von Gas und Partikeln während eines explosiven Vulkanausbruchs nachzustellen. Dabei habe ich die beiden experimentellen Kratergeometrien aus den vorangegangenen Experimenten ausgewählt, welche den stärksten Einfluss auf die Gasdynamik aufgezeigt haben. Zusätzlich habe ich eine dritte Kratergeometrie verwendet, die dem aktiven Krater S1 auf Stromboli nachempfunden ist. Die Geometrie entspricht der Kratergeometrie aus der Vermessung im Mai 2019. Die S1 Geometrie zeichnet sich durch einen asymmetrischen Öffnungswinkel aus (~ 10° auf einer Seite, ~ 40° auf der anderen Seite). Zusätzlich zu den drei Kratergeometrien wurden unterschiedliche Partikel verwendet (Schlacke und Bims), mit jeweils drei unterschiedlichen Korngrößen (0.125–0.25, 0.5–1 und 1–2 mm) und zwei Druckstufen (8 und 15 MPa). Die Partikeldynamik, in der Nähe des experimentellen Kraters, wurde anhand der Winkel des Partikelauswurfs und der Geschwindigkeit der Partikel definiert und beschrieben. Dabei wurde festgestellt, dass die Geometrie des Kraters die Richtung und Neigung des Partikelauswurfswinkels und die Geschwindigkeit der Partikel bestimmt. Bei allen Kratergeometrien kam es zu einem asymmetrischen Partikelauswurf und im Falle von Bimspartikeln zudem zu einer ungleichmäßigen Geschwindigkeitsverteilung.

Die Kombination aus Daten aus Feldkampagnen, Experimenten mit Gas und Experimenten mit zusätzlichen Partikeln zeigte deutlich den starken Einfluss der Kratergeometrie auf Eruptionen. In der Natur, führt eine modifizierte Kratergeometrie zu einem verändertem Auswurfsmuster der Pyroklasten. Im Labor haben komplexe Kratergeometrien zu geneigten Gasstrahlen, asymmetrischen Auswurfswinkeln von Gas- und Gaspartikeln und einer asymmetrischen Verteilung der Geschwindigkeit von Partikeln geführt. Auf Basis dieser Beobachtungen komme ich zu dem Schluss, dass asymmetrische Vulkankrater eine asymmetrische Verteilung von pyroklastischem Auswurf hervorrufen. Das führt zu einer bevorzugten Richtung für vulkanischen Fallout — und falls es zu einer kollabierenden Ausbruchsäule kommt — zu einer bevorzugten Richtung für pyroklastische Ströme.

Der technische Fortschritt durch Drohnen, Photogrammmetrie und 3D Druck bietet einige Chancen für die Vulkanologie. Luftaufnahmen durch Drohnen ermöglichen eine schnelle, günstige und sichere Vermessung von Vulkankratern, auch in Zeiten erhöhter Aktivität. Zusammen mit Photogrammmetrie und 3D Druck lassen sich realitätsnahe Kratergeometrien erzeugen, für zunehmend realistische skalierte Laborexperimente.

Abstract

Volcanic eruptions are among the most violent displays of the Earth's natural forces and threaten human health and infrastructure. Explosive eruptions are hazardous due to their impulsive and dynamic nature, ejecting gas and pyroclasts at high velocity and temperature into the atmosphere. In recent years, monitoring efforts have increased, but forecasting eruptions is still challenging as volcanoes are complex systems with the potential for inherently unpredictable behaviours. To date, the underlying boundary conditions are beyond observation and quantification. Still, they are constrained by physical laws and can be described through models and experiments. The complexity and interdependency of the parameters governing the dynamics of volcanic eruptions ask for increasingly realistic experiments to investigate the sub-surface conditions driving volcanic eruptions.

Above the vent, in the near-vent region, the dynamics of explosive eruptions can first be visually observed. The characteristics at this stage are purely the result of the underlying boundary conditions and the exit (vent) geometry. Volcanic vents are rarely the symmetric features that are often assumed in models and experiments. They often exhibit highly irregular shapes with notched or slanted rims that can be transient. To eventually understand the unobservable boundary conditions, it is necessary to initially gain knowledge about the effect of the observable factors (i.e. vent geometry). This knowledge will ultimately improve the understanding of the parameters affecting an explosive event to develop accurate probabilistic hazard maps.

To this end, a combination of field observations and laboratory experiments was used. First, I characterised vent and crater shape changes at a frequently erupting volcano (Stromboli) to collect high-resolution geometric data of volcanic vents and observe the related explosion dynamics. As a result of topographic changes, variable eruption intensity, style and directionality could be detected. Five topographic data sets were acquired by unoccupied aerial vehicles (UAVs) over nine months (May 2019-January 2020). During this period, changes associated with "normal" Strombolian activity, "major explosions" and paroxysmal episodes (3 July and 28 August 2019) occurred. Hence, the topographic data made it possible to link the predominant constructive and destructive processes to these eruption styles. Furthermore, the number and position of active vents changed significantly, which is a critical parameter for hazard assessment as vent geometry and position can be linked to shifts in eruptive mechanisms. These field surveys highlight the geometric complexity and variability of volcanic vents at an unprecedented spatiotemporal resolution. Additionally, the observations of explosions suggested the paramount influence of crater and vent geometry on pyroclast ejection characteristics, a fact that has strong implications for areas potentially affected by bomb impact and pyroclastic fall out.

Secondly, I designed a series of shock-tube experiments incorporating the geometry elements observed at Stromboli to quantify the influence of vent geometry and several boundary conditions. These experiments validated the link between vent geometry and explosion dynamics that was observed in the field. The novel geometry element is an inclined exit plane of 5°, 15° and 30° slant angle combined with a cylindrical and diverging inner geometry resulting in six vent geometries. All experiments were conducted with gas-only (Argon) at room temperature, four different starting pressures (5, 8, 15, 25 MPa) and two reservoir volumes (127.4 cm^3, 31.9 cm^3). Despite the vertical setup, the slanted geometry yielded both a laterally variable gas spreading angle and an inclination of the jets. The inner geometry controlled the jet inclination towards the dip direction of the slanted exit plane (cylindrical) and against the dip direction of the slanted exit plane (diverging). Cylindrical vents produced larger gas spreading angles than diverging vents. Both gas spreading angle and jet inclination were highly sensitive to the experimental pressure and the slant angle. They had a positive correlation with maximum gas spreading angle and jet inclination. Additionally, the pressure was positively correlated with the maximum duration of under-expanded characteristics of the jet. The gas volume only showed a positive correlation with the maximum gas spreading angle.

Thirdly, I added particles to the experiments to mimic the ejection of gas-particle jets during explosive volcanic eruptions. For this set of experiments, the two geometries with the 30° slant angle from the previous experimental series were used as they exhibited the strongest effect on the gas ejection dynamics. They were supplemented by a third vent that resembled the "real" geometry of Stromboli's active S1 vent as it was mapped in May 2019 and fabricated by 3D printing. The S1's geometry is characterised by a ~10° divergence on one side and a ~40° divergence on the other side. Besides three vent geometries, two types of particles (scoria and pumice), each with three different grain size distributions (0.125–0.25, 0.5–1, 1–2 mm) and two starting pressures (8, 15 MPa) were used. The near-vent vent dynamics were characterised as a function of particle spreading angle and particle ejection velocity. The vent geometry governed the direction and the magnitude of particle spreading, and the velocity of particles. All geometries yielded asymmetric particle spreading as well as a non-uniform velocity distribution in experiments with pumice particles.

The combination of field observations, gas-only and gas-particle experiments demonstrated the prime control exerted by vent geometry. In nature, a modification of the vent led to modified pyroclast ejection patterns. In the laboratory the complex geometries facilitated inclined gas jets, an asymmetric gas and particle spreading angle, and an asymmetric particle ejection velocity distribution. These findings suggest that the asymmetry of volcanic vents and/or craters can promote the asymmetric distribution of volcanic ejecta.

Which, in turn, will lead to a preferred direction of volcanic fallout and — in case a column collapse occurs — to a preferred direction of the ensuing pyroclastic density currents.

The availability of new technology like unoccupied aerial vehicles, photogrammetry and 3D printing provides several opportunities for the volcanological community. Aerial observations allow a fast, inexpensive and safe way to collect geometrical data of volcanic vents and craters, even in times of elevated volcanic activity. In combination with photogrammetry and 3D printing, "real" vents can be produced for increasingly realistic scaled laboratory experiments.

Chapter 1

Introduction

1.1 Motivation

Volcanic eruptions are among the most violent and spectacular displays of the Earth's natural forces. Globally, there are around 1,500 volcanoes with Holocene activity and around 50 volcanoes are erupting each year (Global Volcanism Program, 2013). Volcanic eruptions pose risk to inhabitants, visitors and the infrastructure in areas surrounding active volcanoes. In 2015 more than 1 billion people (14.3 % of the world's population) lived within a 100 km radius around a Holocene volcano and the numbers are increasing (Freire et al., 2019). The population density continues to rise within the proximity to volcanoes, peaking at around 15–20 km away from the volcano (Freire et al., 2019). Large cities in the neighbourhood of active volcanoes can be found worldwide e.g., Auckland in New Zealand (Auckland Volcanic Fields), Jogjakarta in Indonesia (Merapi), Manila in the Philippines (Pinatubo), Mexico City (Popocatepetl), Naples in Italy (Campi Flegrei and Vesuvius), Seattle in Washington, USA (Mt. Rainier), Tokyo, Nagasaki and Kagoshima in Japan (Fuji, Unzen and Sakurajima), Goma in the Democratic Republic of Congo (Nyiragongo) and a number of others (Erfurt-Cooper, 2014). As a result of population growth and land development society's exposure to volcanic risk increases and the numbers of fatal incidents are on the rise (Auker et al., 2013).

Volcanic regions also attract tourists every year. Since the 1990s global tourism is booming with a strong trend towards nature-based tourism, with geo-tourism being one of the fastest growing sectors with Millions of visitors spending time near active volcanoes each year (Erfurt-Cooper et al., 2015). Volcanic regions are appreciated for their scenic landscapes (e.g., Azores Islands, Portugal), their wellness effect (e.g., hot springs in Toyako, Japan), the adventure of ongoing eruptions (e.g., Stromboli Island, Italy; Fagradalsfjall, Iceland) and the cultural sites (e.g., Pompeii, Italy). Elevated volcanic activity draws volcano tourists to explore volcanic features such as Strombolian eruptions, lava flows, lava lakes and fumaroles as well as associated boiling mud ponds, geysers, travertine terraces, crater lakes and hot springs. From a touristic point of view, prolonged Strombolian or Hawaiian eruptions are the most attractive types of volcanic eruptions. They can be observed from reasonably up close with relative safety and if they last months, years or decades, the local economy can thrive on tourism.

Touristic regions like Stromboli Island (Italy), Tanna and Ambrym Island (Republic of Vanuatu) and White Island (New Zealand) owe their popularity to the volcanic activity. They are to some extent depending on stable levels of activity as a cessation of volcanic activity would decrease their appeal, while an intensification could lead to a higher risk and closures by the civil protection authorities. Inhabitants as well as tourists are facing potential dangers directly related to volcanic activity. While inhabitants might be better prepared and informed when dealing with gas emissions, toxic fumes, hot springs and steam vents they are just as vulnerable in case of unexpected eruptions, lava flows, pyroclastic fall out, pyroclastic density currents (PDCs) and earthquakes. In recent years monitoring efforts were increased and advances in the forecasting of eruptions have been made (e.g., Dempsey et al., 2020; Johnson et al., 2018; Layana et al., 2020). Still, unexpected or larger-than-expected eruptions claim human lives, even at well-monitored volcanoes. In 2010 an explosive dome destruction at Merapi (Indonesia) formed a PDC causing more than 370 fatalities, damage to more than 2,200 buildings and a temporary displacement of about 400,000 people (Komorowski et al., 2013). In 2014 an unexpected phreatic eruption of Mt Ontake (Japan) claimed the lives of at least 58 hikers (Yamaoka et al., 2016). In 2019 22 visitors of Whaakari/White Island (New Zealand) were killed by a small phreatic eruption. These are only a small number of examples of recent eruptions causing fatalities amongst the local population or visitors. For an extensive collection of volcanic fatalities refer to Brown et al. (2017). Volcanoes are complex and dynamic systems controlled by interdependencies of many processes and have the potential for behaviours that are inherently unpredictable (Sparks, 2003). However, volcanic eruptions are constrained by physical laws and the combination of observations, experiments, models, monitoring data, knowledge of historical eruptions and analysis of volcanic deposits can help to develop a probabilistic approach for forecasting. To provide more reliable information about the eruptive activity in terms of type, energy, duration and affected areas a deeper understanding of the underlying processes and a link to observable features is essential.

1.2 Background

Explosive eruptions are especially dangerous due to their impulsive and dynamic nature. They are the result of energetic magmatic fragmentation within the conduit driven by gas overpressure derived from exsolution of magmatic volatiles and/or interaction with meteoric water, groundwater or ice. As magma ascends from depth towards the surface, decompression causes exsolution of volatile phases and crystallisation. These phase transitions have an impact on the density, rheology and, to a lesser extent, the temperature of the mixture (Cashman and Sparks, 2013). Solubility of volatiles is higher at high pressures (e.g., Newman and Lowenstern, 2002; Papale et al., 2006; Wallace et al., 2015). As a result, decompression of a volatile-saturated melt causes exsolution of the volatile phase as (gas) bubbles. If the gas is retained in the magma instead of being lost to the atmosphere or the wall rocks, overpressure can build up within the bubbles. If this overpressure exceeds the tensile strength of the magma, fragmentation occurs (e.g., Alidibirov and Dingwell, 1996a,b).

During fragmentation, the magma which is considered as a continuous liquid (± crystals and bubbles), is disrupted. As not all potential (gas pressure and thermal) energy has been consumed, excess energy is transformed into the kinetics of acceleration of the newly-formed fragments and a gas-particle jet is ejected through a vent into the atmosphere. Above the vent, the surficial manifestation of the eruption can be observed while the driving forces remain concealed in the subsurface and therefore beyond our direct observation. What we can observe is the result of the interplay of various source (e.g., temperature, depth, rheology, overpressure), pathway (e.g., fragmentation depth, conduit geometry, ascent velocity) and exit conditions (e.g., vent geometry, overpressure at the vent, open or clogged vents, crater geometry). The ejected gas-pyroclast mixture frequently shows the characteristics of an underexpanded starting jet (e.g., Carcano et al., 2013; Kieffer, 1984; Woods and Bower, 1995). The near-vent characteristics of volcanic jets are an important feature, since they are the first observable manifestation of the processes below the surface. Directly above the vent, the attributes of the jet are purely the result of the combination of the underlying boundary conditions and the vent geometry, while, further downstream, atmospheric conditions can substantially alter the jet dynamics. The attributes of this jet thrust region significantly affect the further development of the eruption column, i.e. if a buoyant plume will rise or a (partial) collapse may occur forming PDCs.

Vent geometry has a considerable impact on the ejection of gas-particle jets at volcanoes as well as in the laboratory. Vent geometry is linked to plume dynamics by affecting ejection velocity (e.g., Cigala et al., 2017; Kieffer, 1989; Ogden, 2011; Wilson et al., 1980; Wilson and Head, 1981), jet radius (e.g., Jessop et al., 2016; Koyaguchi et al., 2010; Woods, 1995) and entrainment efficiency (Suzuki et al., 2020). In experiments and numerical models, the vent geometry is usually simplified and assumed to be cylindrical or a symmetric funnel. However, volcanic vents frequently show complex and asymmetric geometries with irregular shapes, encompassing craters and variable exit heights and divergence angles. Furthermore, vent geometry can be transient and change during a single volcanic explosion or remain stable over the course of several months. Nowadays, vent and crater geometry and their changes can be analysed by unoccupied aerial vehicles (UAVs) at unprecedented spatiotemporal resolution. UAVs are a suitable tool for repeated surveys, as they are cheap to operate and allow data acquisition even during times of heightened activity from a safe distance. Their ability to acquire high-resolution imagery, conduct measurements or collect samples in hazardous or inaccessible areas makes them an ideal tool for the volcanological community (refer to James et al. (2020b) for a comprehensive review of volcanological applications).

Laboratory experiments provide a unique possibility to control source, path and vent conditions in a repetitive regime. Although necessarily simplified with respect to nature, they allow parameter isolation and deterministic testing. The acceleration of low- to non-cohesive powders following gas decompression has been studied since the early 1990s (e.g., Anilkumar et al., 1993; Cagnoli et al., 2002; Cigala et al., 2017). Shortly afterwards, the fragmentation of viscous magma by the same process was demonstrated by (Alidibirov and Dingwell, 1996a,b). Since that time, several studies have investigated the relationship of particle generation with different starting conditions (e.g., Alatorre-Ibargüengoitia et al., 2010, 2011; Kueppers et al., 2006a,b; Montanaro et al., 2016). Chojnicki et al. (2006) quantified the general dependence of gas-particle velocity and particle size. Large scale experiments by Dellino et al. (2014) helped to link jet conditions, plume development and entrainment characteristics. Experiments with buried explosive charges in loose, granular material were used to investigate jet spreading angle and velocity for explosions in pre-existing craters (Taddeucci et al., 2013b; Valentine et al., 2012b). Solovitz et al. (2014) conducted laboratory experiments with a compressed air jet expanding through vents fabricated from sand and steel powders. By using erodible vents, they showed the influence of vent enlargement on sustained jets. Increasing vent size is considered to facilitate column collapse (Koyaguchi et al., 2010). Jessop et al. (2016) investigated the role of vent shape, aspect ratio and inertial particles on the likelihood of column collapse by utilising scaled laboratory experiments. They injected a particle-water mixture at a constant rate into a tank of water through symmetric elongated or annular vents to observe entrainment dynamics.

There is a strong need for increasingly realistic experiments to better explore the link between observable eruption dynamics and the underlying, concealed boundary conditions that, to date, have remained beyond observation and measurement. Here, I quantified natural complexity of vent geometries and, for the first time, incorporated this complexity in the design of an experimental series. I elucidated the influence of various subsurface boundary conditions and complex vent geometries on the dynamics of gas-particle ejection and the related hazards, pushing experiments closer towards nature by:

1. Characterising volcanic vents and their temporal evolution by UAV to identify common asymmetry features at a persistently erupting volcano. (Chapter 2)
2. Quantifying topographic changes related to "normal" Strombolian, major and paroxysmal explosions at Stromboli volcano. (Chapter 2)
3. Conducting gas-only experiments with complex, but still simplified, vent geometries defined by a slanted exit plane to evaluate the pure impact on fluid dynamics for varying boundary conditions (six vent geometries, four gas pressures and two gas volumes). (Chapter 3)
4. Conducting gas-particle experiments with complex, known vent geometries defined by a slanted exit plane to quantify the effect of gas-particle interaction and the particle's

response to the geometry under varying boundary conditions (two gas pressures, two particle densities with three particle size classes each). (Chapter 4)

5. Utilising UAV photogrammetry and 3D printing to fabricate a realistic vent geometry for gas-particle experiments with varying boundary conditions (two gas pressures, two particle densities with three particle size classes each). (Chapter 4)

6. Combining scaled laboratory experiments and direct observations of explosive volcanic eruptions to identify a link between asymmetric vent geometry and the distribution of proximal and distal hazards. (Chapter 3 & 4)

1.3 Vent and crater shape changes at Stromboli

Active volcanoes are usually subject to frequent substantial topographic changes as well as variable eruption intensity, style and/or directionality. Here, I analysed five high-resolution topographic data sets of volcanic craters and vents from Stromboli volcano, Italy, that were acquired by UAV during five field campaigns between May 2019 and January 2020. During this period, two unexpected paroxysmal episodes occurred on 3 July 2019 and 28 August 2019. I used this data to characterise the geometries of the active craters and vents and I found that, independent of the shape, the vents often exhibited a variable vent exit height. Considering the maximum difference between highest and lowest point of the vent (Δh_{rim}) and the diameter of the vent, I calculated the theoretical slant angle of the exit plane which was then used to define slant angels for the design of the experimental vents. At Stromboli, they range from 10° to 39° with an average slant angle of ~16° calculated from 22 vent/crater geometries. For the experiments I decided on using slant angles of 5°, 15° and 30°.

Additionally, vent evolution is a critical parameter for volcanic hazard assessment as shifts of vent geometry and positions can be linked to shifts in eruptive mechanisms (Graettinger et al., 2015b; Taddeucci et al., 2013b; Valade et al., 2016). During the 9 months when the field campaigns were carried out the "normal" Strombolian activity was punctuated by "major explosions" and the two paroxysms. In May 2019, by chance, a "major explosion" occurred during the field campaign, which enabled an assessment of the immediate changes of vent geometry and the resulting eruption dynamics. Furthermore, the two paroxysms on 3 July and 28 August 2019 allowed for observations of changes where deeper parts of the shallow plumbing system were affected.

Photogrammetry at Stromboli volcano

Stromboli is the ideal target volcano for campaigns focusing on geometry changes and eruption dynamics because its continuous activity almost guarantees the observation of eruptions. The vents are located at the crater terrace, a break in the slope of the Sciara del Fuoco at around 800 m above sea level. The number of active vents varied over the last years between 3 and 15 and they are commonly grouped into two or three vent areas: the north-eastern vent area (NE), the southern (S) and central (C) vent area which are sometimes grouped together (CS). During ‘normal’ activity there are explosions every few to tens of minutes ejecting ash, lapilli, and incandescent bombs up to heights of a few hundreds of meters above the vents.

The field campaigns were conducted over 11–16 May 2019, 5–13 June 2019, 4–5 August 2019, 21–26 September 2019 and 25–27 January 2020. During these days aerial images and videos were collected with a DJI *Mavic 2Pro* and a DJI *Phantom 4Pro+*. The flights were done at heights between 50 and 150 m above the crater terrace resulting in a ground sample distance between 3.8 and 5.3 cm/pixel. Through Structure from Motion (SfM) photogrammetry 3D models, digital elevation models (DEMs) and orthomosaics were created. The resulting products were analysed for changes of geometry, surface elevation, vent and crater shape and location as well as changes in the eruptive behaviour.

Key findings

During the observational period the prevailing classification of vents into two-to-three main centres of activity was valid. The position of craters and vents appears to be structurally controlled with S2 and the central vents being aligned along a NE-SW trending feature that is parallel to an old dyke to the west of the crater terrace. The DEMs showed that during the 3 July 2019 paroxysm a minimum of 30 m of material was removed by explosive excavation in the area of S2. It seems that the initial explosion was produced by S2 and N2 destroying the uppermost (few tens of meters) plumbing system below the crater terrace. In a relatively short amount of time the excavated material was replaced by a heterogeneous zone of variably cohesive and sized fall-back material providing additional pathways for magma to reach the surface. This facilitated the large number of active vents in the N vent area in August 2019. However, the deeper portions of the plumbing system remained unaffected, because the activity was soon re-focused on fewer active vents inside the N1 and N2 craters.

The changes of individual vents that could be observed on a timescale of days were accompanied by changes in style and direction of explosions. The changes of eruptive behaviour and directionality were solely a result of the modified, now asymmetric, vent geometry. Because of the short timescale, these changes cannot be explained by tilting of the crater terrace or the underlying plumbing system. These observations highlight the link between vent/crater asymmetry and directed explosions and should be considered as a source for a preferential distribution of proximal and distal hazards.

1.4 Release of overpressurised gas from complex vents

Explosive volcanic eruptions often exhibit the characteristics of underexpanded starting gas-particle jets over a wide range of eruption styles (e.g., Strombolian, Vulcanian, Plinian eruptions and phreatomagmatic explosions (Gouhier and Donnadieu, 2011; Koyaguchi and Woods, 1996; Scharff et al., 2015; Taddeucci et al., 2012). The jet dynamics can be affected by several parameters, including magma texture, gas overpressure, erupted volume and vent geometry. With respect to the latter, volcanic vents and craters are often highly asymmetrical.

Experimentally, shock-tube experiments have been used extensively to mimic such starting jets at controlled, reproducible conditions (e.g., Alidibirov and Dingwell, 1996a; Anilkumar et al., 1993; Cigala et al., 2017; Dellino et al., 2014; Kieffer and Sturtevant, 1984; Kueppers et al., 2006b) and serve as a basis for numerical models (e.g., Lagmay et al., 1999; Ogden et al., 2008a; Sommerfeld, 1994). Cigala et al. (2017) revealed a general nonlinear decay of particle exit velocity, governed by (1) tube length, (2) particle load, (3) vent geometry, (4) temperature and (5) particle size. They showed that vent geometry controls gas flow which in turn affects particle dynamics. Here, I focused on gas-only shock-tube experiments to reveal the influence of complex vent geometries on gas expansion dynamics without possible feedback from particles. In order to do this, I modified two of the radially symmetric geometries of Cigala et al. (2017) with a slanted exit plane.

Experiments

I conducted the scaled shock-tube experiments in the "fragmentation laboratory" at LMU Munich. This setup is an evolved version of the "fragmentation bomb" developed by Alidibirov and Dingwell (1996a). Argon was used for the pressurisation to the desired experimental conditions. All experiments were conducted at constant temperature (25° C) and four pressure ratios (5, 8, 15, 25 MPa) as well as two autoclave volumes (127.4 cm^3, and 31.9 cm^3). As basis, two geometrical configurations were used: cylindrical and diverging (15°) inner geometry, both with 5°, 15° and 30° slant angles resulting in six vent geometries.

The rapid decompression experiments were recorded with a high-speed camera at 10,000 frames per second. Once the decompression was initiated the resulting pressure drop was recorded by a pressure sensor inside the autoclave, triggering the movie acquisition. Due to the decompression, the expanding Argon cools and condenses allowing the visual observation of the gas phase. Scaled single frames were exported and manually analysed with a focus on gas spreading angle and jet inclination.

Key findings

Both, spreading angle and jet inclination were sensitive to reservoir pressure and the vent's slant angle. The spreading angles evolved with time, exhibiting a fast buildup to the maximum value followed by a slower decay. The experimental pressure was of paramount influence on the maximum gas jet spreading angle where higher pressures caused larger spreading angles. The cylindrical vent geometry also produced larger spreading angles than diverging vents. Initial gas volume showed a positive correlation with spreading angle. In case of cylindrical vents, the slant angle has little effect on the spreading angle and the difference between lower and upper sides is generally small (around 2°). For diverging vents with 30° slant angle the difference is between 8° and 14° with the smallest difference in experiments with 25 MPa.

As a result of the slanted exit plane, the jets were inclined: for cylindrical vents, the jets were inclined in the dip direction of the vent surface, while diverging vents showed inclination towards the opposite side. In case of cylindrical vents, slant angel had the strongest effect on jet inclination, followed by pressure. The maximum inclination of 13° could be observed for the cylindrical, 30° slanted vent with 25 MPa overpressure. Jet inclination of diverging vents was less variable and generally between 2° and 7° for all conditions. There was no clear correlation between the degree of jet inclination and pressure and/or slant angle.

In nature inclined jets have been observed and attributed to inclined conduits (Zanon et al., 2009), heterogeneities of the high viscosity layer inside the conduit (Kelfoun et al., 2020) and asymmetry of the vent and/or crater (Cole et al., 2015; Lagmay et al., 1999). Here, for the first time, I demonstrated experimentally that both laterally variable spreading angles as well as inclined jets can be emitted as a consequence of complex vent geometry despite a vertical conduit. These findings have implications for the generation of asymmetrical distribution of hazards around volcanic vents.

1.5 Complex vent geometry and asymmetric particle ejection

Explosive volcanic eruptions eject gas and pyroclasts at high velocity and temperature into the atmosphere. The related threat to life and infrastructure is a consequence of style and magnitude of the eruption. Although, monitoring efforts have been increased in recent years, unforeseen or larger-than-expected eruptions still claim human lives. To achieve a better understanding of the boundary conditions and the related tipping point that inevitably leads to an explosive event it is essential to better constrain the unobservable sub-surface processes. In nature, gas-particle ejection can be influenced by inclined conduits, debris coverage, variable explosion depth, pre-existing craters or an inhomogeneous high-viscosity layer. In the laboratory, we can exclude any of these factors and investigate the sole effect of sub-surface boundary conditions and vent geometry. As the near-vent characteristics of an explosive eruption are a direct result of these sub-surface processes I used scaled shock-tube experiments with controlled boundary conditions to mimic explosive eruptions and analysed their near-vent characteristics. To this end, I used three complex vent geometries, two types of particles (each with three particle size classes), two experimental pressures to further elucidate the effect of vent geometry and gas-particle coupling on particle spreading angle and particle velocity. Additionally, I discussed the effect of complex vent geometry on gas-particle ejection in respect to implications for the distribution of volcanic hazards.

Experiments

The same experimental setup was used as in Schmid et al. (2020) in the "fragmentation laboratory" at LMU Munich. Hereby, two of the vent geometries (cyl30 and fund30) and two experimental pressures (8 and 15 MPa) were selected and complemented by a new geometry (S1). Two types of natural volcanic particles were used (scoria and pumice), both with particle sizes of 0.125–0.25, 0.5–1 and 1–2 mm. Temperature (25° C), volume of the autoclave and Argon as driving medium were kept identical throughout the experimental series. The S1 vent is a miniaturized version of the active S1 vent at Stromboli volcano in May 2019. The experimental vent was fabricated by additive 3D printing of the 3D model produced by UAV photogrammetry (Schmid et al., 2021). The defining geometry element of the S1 vent was the asymmetric divergence with ~10° on one side and ~40° on the opposing side.

Key findings

The performed experiments show that the particle spreading angle was affected by vent geometry, particle size, particle density and experimental pressure. A comparison of the maximum spreading angle of the cyl30 and fun30 vents showed a larger angle for the cyl30 experiments. This was particularly pronounced on the lower vent side and for the fine particle size fraction. However, both geometries had an asymmetric particle spreading angle with the largest value on the lower vent side. The S1 geometry exhibited asymmetry as well, the largest particle spreading angle was visible at the more diverging side of the vent. For all geometries, a higher experimental pressure, smaller particles and a lower particle density facilitated a larger particle spreading angle. While vent geometry governed the direction and the degree of asymmetry of the particle spreading angle, particle size and density as well as experimental pressure influenced the magnitude of the particle spreading.

The difference in particle ejection velocity was a function of particle density, vent geometry, pressure and subordinately particle size. Particle density accounted for up to ~100 m/s higher velocities for pumice samples, while an increased pressure (8 to 15 MPa) accounted for ~50 m/s. As a result, the highest particle velocity was measured in experiments with pumice particles and 15 MPa overpressure. Up to ~30 m/s of velocity difference could be attributed to vent geometry. The fun30 exhibited the fastest particle ejection velocity. In experiments with the S1 geometry and pumice samples, a up to ~60 m/s higher velocity was measured on the right (more diverging) side of the vent compared to its left side.

The experiments showed that particle trajectory and particle ejection velocity were substantially controlled by vent geometry. In case of volcanic eruptions, both, pyroclast trajectories and velocities are known to affect volcanic ballistics and eruption column stability. Hence, irregular vent geometry and the resulting asymmetric distribution of pyroclasts directly affects the areas prone to volcanic hazards. If the criteria for (partial) collapse are achieved irregular vent and/or crater geometries can lead to a preferentially focused emplacement direction of associated PDCs.

Chapter 2

Characterising vent and crater shape changes at Stromboli: implications for risk areas

2.1 Abstract

Active volcanoes are typically subject to frequent substantial topographic changes as well as variable eruption intensity, style and/or directionality. Gravitational instabilities and local accumulation of pyroclasts affect conditions at the active vents, through which gas-particle jets are released. In turn, the vent geometry strongly impacts the eruption characteristics. Here, we compare five high-resolution topographic data sets (<4 cm/pixel) of volcanic craters and vents from Stromboli volcano, Italy, that were acquired by unoccupied aerial vehicle (UAV) during five field campaigns between May 2019 and January 2020. This period includes two paroxysmal explosions (3 July and 28 August 2019) and exhibited significant changes on day-to-month timescales. Our results highlight changes to vent geometry and their strong control on the directionality of explosions. Recurrent UAV surveys enable the monitoring of temporal morphologic changes and aid the interpretation of observed changes in eruption style. Ultimately, this may contribute to repeatedly revised risk areas on permanently active volcanoes, especially those that are important tourist destinations.

2.2 Introduction

Vent evolution is a critical parameter for volcanic hazard assessment as shifts of vent geometry and position can be linked to shifts in eruptive mechanisms (Graettinger et al., 2015b; Taddeucci et al., 2013b; Valade et al., 2016). The geometrical evolution of craters can be correlated with processes of crater formation to enhance the understanding of active volcanic processes (Hanagan et al., 2020). Direct observations detecting changes in the activity at persistently active volcanoes can provide insights into the shallow conduit system, which, in turn, also improves hazard assessment (Capponi et al., 2016; Salvatore et al., 2018; Simons et al., 2020). Not only can the geometry be affected by the eruptive activity but vent geometry can also modulate the dynamics of volcanic explosions.

While vent geometry can be measured directly, our knowledge about conduit geometry has been constrained based on inactive fissures, eroded volcanoes, laboratory experiments or through indirect geophysical methods (Chouet et al., 2003; Keating et al., 2008; Parcheta et al., 2016; Zorn et al., 2020a). Some morphological features are unlikely to be a direct proxy of the uppermost plumbing system before eruption/explosion. For example, excavated craters/conduits following major Vulcanian/Plinian explosions have probably widened due to the explosion intensity (Wilson et al., 1980) (giving a propensity for lithic components in pyroclastic deposits) and gravitational instabilities (Calvari et al., 2006), and drained lava lakes frequently exhibit funnel-like geometries (Patrick et al., 2019) that are probably the result of convection-driven thermal erosion. In contrast, spine growth (especially the cross sectional shape and extrusion direction) has been used to infer ascent velocities, magma properties and conduit geometry (Lacroix, 1904; Vallance et al., 2008; Zorn et al., 2020a). The effect of inclined conduits on eruption dynamics was first demonstrated experimentally by James et al. (2004) who showed that gas slugs (constant starting volume and pressure differential) rising in inclined conduits will be less overpressured at burst compared to vertical conduits. Gas overpressure at the vent has been demonstrated experimentally to affect gas-only and gas-particle jet dynamics (Alatorre-Ibargüengoitia et al., 2011, 2010; Schmid et al., 2020). Lagmay et al. (1999) and Major et al. (2013) linked asymmetric crater geometry to inclined eruption columns and, as a consequence, to a preferential distribution of proximal volcanic hazards. Taddeucci et al. (2013b) illustrated how the presence of a crater may change the dynamics of eruptive jets.

The link between vent geometry and jet dynamics has been investigated experimentally through rapid decompression experiments where impulsive jets have been released from a vertical shock-tube setup. For instance, Cigala et al. (2017) explored the influence of four different radially symmetrical vent geometries on gas-particle jets and constrained the effect of vent geometry on residual overpressure at the vent, a parameter that contributes to jet expansion and particle dispersion. In similar experiments with the same setup, Schmid et al. (2020) focussed on the characteristics of gas-only jets released from vent geometries with reduced symmetry. In these experiments, six vent geometries were fabricated using two designs with the strongest impact (cylindrical, 15° diverging inner geometry of Cigala et al. (2017) combined with a slanted surface plane (5°, 15°, 30°)). These experiments confirmed that the bilateral vent symmetry is a major controlling parameter for the expansion dynamics of gas-only jets, leading to jet inclination and asymmetric spreading angles despite a vertical conduit.

Understanding vent evolution and migration, as well as crater and/or vent asymmetry and their links to eruption dynamics and mechanisms, may improve hazard assessment. Tourist destination volcanoes (e.g. Stromboli, Italy; Villarica, Chile; Whakaari/White Island, New Zealand; Yasur, Vanuatu) are famous for the accessibility of observational points but infamous for unheralded strongly explosive events (e.g., Dempsey et al., 2020; Giordano and De Astis, 2021; Viccaro et al., 2021). Depending on eruption frequency, recurrent up-close surveys of the active crater area can reveal high(er) temporal resolution information on changes. Eruptive activity is known to vary on several scales, including — but not limited to — eruption frequency and height, erupted volume, grain size distribution, pyroclast temperature and jet directionality (e.g., Andronico et al., 2009; Harris and Ripepe, 2007; Taddeucci et al., 2013a; Zanon et al., 2009). Changes in eruption characteristics may be influenced by observable topographic changes of active vents (shape, size, depth, open/closed, rim height) (e.g., Capponi et al., 2016; Cole et al., 2015; Jessop et al., 2016; Solovitz et al., 2014; Suzuki et al., 2020).

Over the past 30 years, documentation of active craters has developed from increasingly complex sketches and photographs (e.g., Andronico et al., 2013; Calvari et al., 2014; Harris and Ripepe, 2007) to aerial imaging and remote sensing data (James et al., 2020b; Turner et al., 2017; Zorn et al., 2020b). Because of their versatility, UAVs have become a powerful tool for many geoscientific fields (Eltner et al., 2016; Niedzielski, 2018). Their ability to acquire high-resolution imagery, conduct measurements or collect samples in hazardous or inaccessible areas makes them an ideal tool for the volcanological community (see James et al. (2020b) for a comprehensive review of volcanological applications). Repeated observations of active vents by UAV (Figures 2.1 and 2.2) and production of digital elevation models (DEMs) allows for precise, quantitative comparison of temporal changes. At persistently active volcanoes such as Stromboli, UAVs provide an excellent opportunity to perform measurements several times a year and achieve a statistically robust morphological dataset over long periods, at high temporal and spatial scales.

Turner et al. (2017) used UAVs to map active and inactive vents at Stromboli in May 2016. Here, we use UAVs to repeatedly acquire imagery for structure from motion (SfM) reconstruction in order to characterise and quantify changes of Stromboli's crater terrace, including the geometry of craters and vents at unprecedented spatiotemporal scales. We also use our photogrammetric models to quantify position, size and asymmetry of active craters and vents at Stromboli. In combination with observations of volcanic explosions we link the geometric variability of vents and craters to eruptive behaviour and the affected areas.

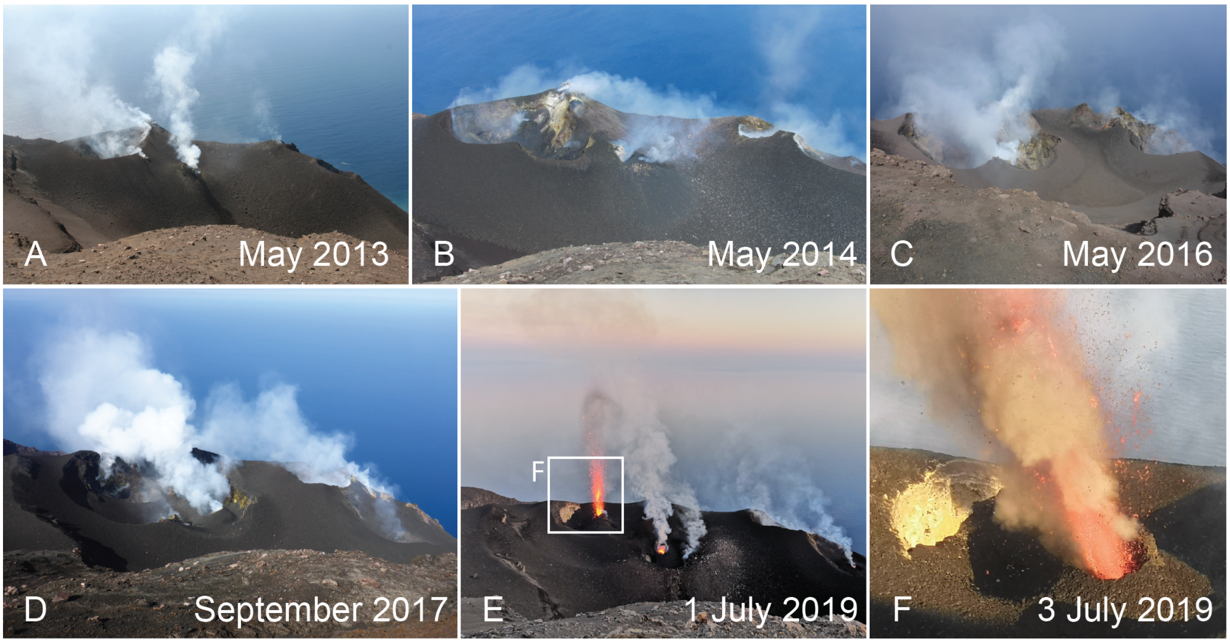

Figure 2.1: Morphological variations of the crater terrace of Stromboli volcano, Italy, as seen from Pizzo between 2013 and 2019. Variations are due to recurring subsidence/collapse events and accumulation of pyroclastic material and lava flows. (A)-(E) show the entire crater terrace while (F) is a zoom to a spatter cone. (E) and (F) show the development of the spatter cone within a mere two days. Eruptive processes led to a geometry change of the spatter cone, visibly affecting the directionality of eruptive jets. Images (A)-(D) by Ulrich Kueppers, (E) and (F) courtesy of Angelo Cristaudo.

2.2.1 Activity and morphology at Stromboli volcano

Stromboli volcano, Italy, is perhaps best known for its continuous eruptive activity for the past 2000–2500 years (Rosi et al., 2000). In the recent decades, Stromboli's activity has been characterised by mild, persistent explosive activity every few to tens of minutes ejecting ash, lapilli, and incandescent bombs up to heights of a few hundreds of meters above the vent (e.g., Andronico et al., 2013; Bertagnini et al., 1999; Patrick et al., 2007; Taddeucci et al., 2013a). This "normal" Strombolian activity is periodically interrupted by two types of more energetic explosions, known as "major explosions" and paroxysms as well as the eruption of lavas (Barberi, 1993; Ripepe et al., 2008). The largest events in the past century ejected metre-sized bombs and blocks as far as inhabited areas located ca. 2 km away (e.g., Calvari et al., 2011; Rittmann, 1931; Rosi et al., 2000). Such activity, albeit rare (most recently on 3 July 2019, 28 August 2019 and 19 July 2020), poses various hazards including pyroclastic density currents, ballistic impact, respiratory problems and vegetation fire (Brown et al., 2017). The paroxysm on 3 July 2019 emitted an eruption column ~5–8.4 km high and a pyroclastic flow that travelled down the Sciara del Fuoco (Giordano and De Astis, 2021; Giudicepietro et al., 2020). This eruption marked the start of a 2-month-long effusive phase.

The 28 August 2019 paroxysm (~6.4 km high) was similar in style to the 3 July 2019 and was also accompanied by a pyroclastic flow and a lava flow (Giordano and De Astis, 2021; Giudicepietro et al., 2020).

As a result of different eruptive styles, magnitude and frequency, the number and positions of vents as well as their geometry is affected (Calvari et al., 2014). The active vents at Stromboli are located within the crater terrace, a break in slope at the top of the Sciara del Fuoco at about 800 m above sea level (asl), lying below the common lookout point Pizzo or Sopra la Fossa at around 918 m asl. The morphology of Stromboli's crater terrace has long been of great interest, as evidenced by scientific descriptions, illustrations and photographs throughout the centuries. Washington (1917) reviewed 21 publications between 1768 and 1915 with a focus on the persistence of Stromboli's active vents. For the past several decades, the crater terrace has hosted three main vent areas: north-east (N), south-west (S) and the central (C), with S and C areas being often grouped together (Salvatore et al., 2018). We use "vent" as a term describing the opening in the ground from where gas and pyroclast jets are ejected, e.g. N1 for the vent number 1 in the north-east vent area, S2 for the vent number 2 in the south vent area . If there is a "crater", i.e. a negative, subcircular volcanic landform around a vent, they are named after the associated vent (see Figure 2.3A and 2.4A for an overview).

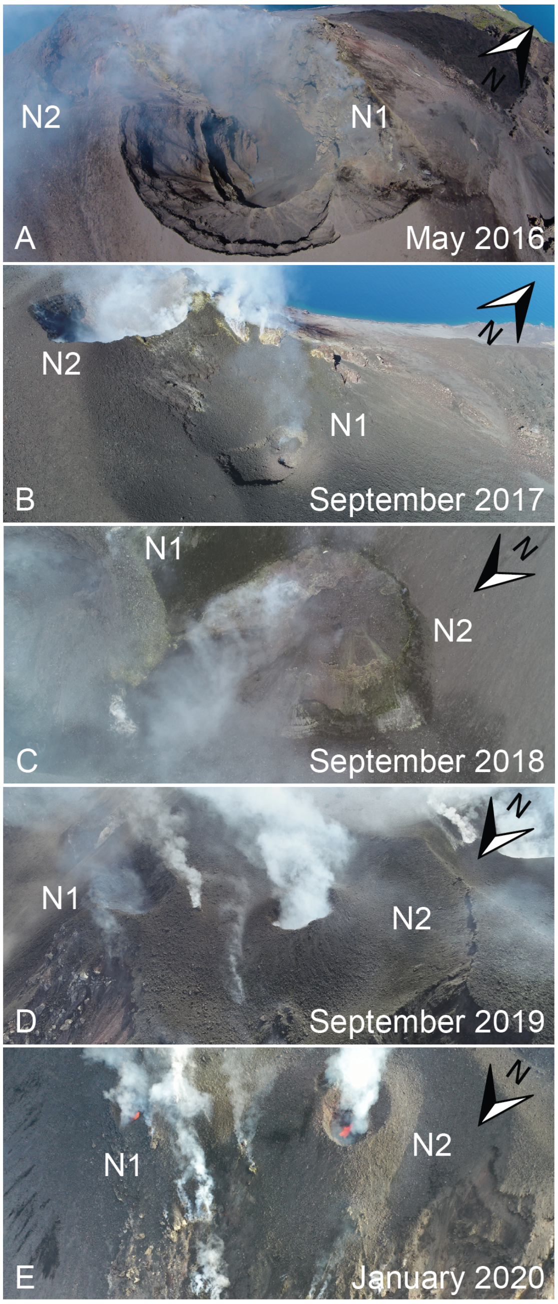

Figure 2.2: Strong morphological variations of N1 and N2 (vents 1 and 2 of the N vent area) of Stromboli volcano, Italy, due to recurring subsidence/collapse events and accumulation of pyroclastic material as seen by UAVs between 2016 and 2020. Arrows indicate North.

Recent publications (e.g., Gaudin et al., 2017; Harris and Ripepe, 2007), as well as recurrent observations (at least once per year) of the crater terrace by several co-authors since 2005 have revealed significant variations in eruption style and frequency, and vent number (between 3 and 15, see Figure 2.1). The shallow plumbing system below the crater terrace has been investigated with tilt meters (Bonaccorso, 1998), seismic networks (Chouet et al., 2003) and continuous GPS (Mattia et al., 2004). These studies suggest the presence of a NE–SW trending structural weak zone that coincides with the direction of dykes exposed in the edifice. Zanon et al. (2009) analysed explosions from Instituto Nazionale di Geofisica e Vulcanologia's (INGV) monitoring webcams and observed inclined jets which they linked to conduit geometry or conduit inclination. Calvari et al. (2014) proposed that morphology changes between 2002 and 2007, together with a massive collapse of the summit crater, have modified the shallow feeder conduit, leading to changes in the eruptive style (i.e. increasing the number of major explosive events and lava overflows).

2.3 Methodology

2.3.1 Field campaigns

We contribute five aerial data sets of Stromboli's crater terrace over nine months (May 2019 and January 2020). Due to the fact that two paroxysms (on 3 July and 28 August 2019) occurred during this period (Giudicepietro et al., 2020), these data provide an opportunity to investigate both the "normal" activity of Stromboli and also changes where deeper portions of the shallow plumbing systems were affected. During each campaign, several vents were active, with variable styles of "normal" activity occurring (Figures 2.1, 2.2 and 2.8).

Field campaigns were conducted over 11–16 May 2019, 5–13 June 2019, 4–5 August 2019, 21–26 September 2019 and 25–27 January 2020. During this time, Stromboli volcano was erupting frequently, with several explosions occurring during the UAV mapping flights, resulting in gas or ash plumes as well as pyroclastic ejecta up to 150 m above the vents. Therefore, all flights had to be conducted manually without predefined flight paths in order to be able to react quickly to prevent loss of, or damage to the UAVs. We mitigated systematic errors in our topographic models by following workflow and best-practice suggestions (e.g., Eltner et al., 2016; James et al., 2020a, 2019).

The flights were conducted at heights between 50 and 150 m above the main area of interest, with a double grid flight path and nadir to off-nadir camera angles. These low flight altitudes were chosen to accomplish a ground sampling distance (GSD) of a few centimetres. The August 2019 flights have a ground resolution of 5.8 cm/pix, the other flights (May, June, and September 2019 and January 2020) have an average resolution of 4.2 cm/pix (Table A1). During individual campaigns, up to 20 flights were performed over several days to ensure full coverage of the entire area of interest, under good light conditions and minimal obscuration by the degassing plume. Here, we present DEMs generated from images of individual flights with sunny to overcast sky and variable wind speed (Table A2). The camera was set to shutter priority with high shutter speeds (1/240–1/500 s). Due to the main focus of this study being the crater terrace and active vents, placing ground control points (GCPs) was not possible. Hence, the global navigation satellite system (GNSS) camera position information was used for georeferencing. In June we had the opportunity to fly on four out of five days (between 8 June and 12 June 2019) and focused on the short-term development of the N area. Four out of the five survey flights were performed by LMU staff (focused directly on the crater terrace and the geometry of vents and craters) and one flight by INGV Rome staff (August 2019). Additionally, we recorded UAV and ground-based video footage and imagery of the eruptive phenomenon to establish a direct link between vent geometry and the resulting eruption dynamics.

2.3.2 Hardware and software

We used two UAVs from DJI: *Phantom 4Pro+* and *Mavic 2Pro*. The *Phantom's* camera has a 1 inch CMOS sensor and 8.8 mm focal length (equal to 24 mm as 35 mm equivalent) with a maximum resolution of 5472 × 3648 pixels and a mechanical shutter. The Mavic's camera uses the same size sensor but with a 10.2 mm (28 mm as 35 mm equivalent) focal length and an electronic shutter.

Different software packages were used for 3D reconstruction of the acquired aerial imagery and the analysis of the obtained models. The structure from motion (SfM) algorithm of *Agisoft Metashape* (Version 1.5.1 – 1.6.1) was used to match image features to make a coarse 3D reconstruction of the surface. By comparing matching features across several images, the 3D position of the cameras can be calculated. Building on this, the multi-view stereo (MVS) algorithm of *Agisoft Metashape* uses the coarse cloud and the obtained camera parameters to perform the reconstruction of a dense cloud. The open source software *CloudCompare* (Version 2.10.2) and *QGIS* (Version 3.10) were used to perform cloud-to-cloud and cloud-to-mesh comparisons as well as DEM and orthomosaic comparisons, respectively.

2.3.3 Processing

Suitable images covering the area of interest were selected and imported into *Metashape* to check image quality (*Agisoft Metashape* Image Quality) and remove blurred images. As cut-off criteria, we used thresholds of 0.8 (May, June, August and September 2019) and 0.6 (January 2020). DJI UAVs are known to have accuracy problems in the flight height information stored in the image metadata that are beyond those of usual GPS inaccuracies.

Therefore, a correction was applied to adjust for the in-flight vertical sensor offset[1]. Areas with strong degassing and areas covered by the gas plume were masked to prevent artefacts during 3D reconstruction. The images were aligned to produce the sparse cloud, roughly representing the topography of the survey area. To improve image alignment, the camera model was optimised by including focal length (f), affinity ($b1$), the centre of distortion (cx, cy) and both radial (k) and tangential distortions (p) of the lens within the bundle adjustment. The GNSS camera positions were included as control observations during the bundle adjustment with uncertainty estimates of 10 m in the three Cartesian directions.

Before further processing, the sparse cloud was cleaned by applying several filter criteria to remove points with weak geometry, large pixel matching errors and large pixel residual errors. The threshold for the reconstruction uncertainty was set to 15, points with a higher uncertainty were removed. The level for the projection accuracy was set to 3. The desired threshold for the reprojection error was 0.3 pixels. To reach this level, the threshold was set in a way that a maximum of 10 % of the total points was removed in every iteration until 0.3 was reached. Between iterations, the optimization (parameters: f, $k1$, $k2$, $k3$, cx, cy, $p1$, $p2$, $b1$) of the camera alignment was repeated, further decreasing the reprojection error to below 0.323 pix. The optimised sparse cloud was the basis for the creation of the dense cloud (high quality, mild depth filtering). The dense clouds were filtered by point confidence and points with a confidence level below 1 were removed. Where necessary, the dense point cloud was improved by manually deleting artefacts. From the dense cloud, all other products were calculated, e.g. meshed 3D models, tiled 3D models, DEMs and orthomosaics. The created DEMs have an average resolution of 8.4 cm/pix and a maximum resolution of 7.6 cm/pix (Table A2). To identify and locate vents, incandescence and fumaroles, orthomosaics were created by projecting the aerial images onto the 3D surface of the model or the DEM. As a result of this, the spatial resolution was increased to an average of 3.7 cm/pix, allowing a better recognition of ground features than from the DEMs alone.

2.3.4 Analysis

Visibility was best in June 2019. Accordingly, it was used as a reference model where prominent features were identified for the referencing of the other models (see Figure 2.3). Due to a lack of clear imagery, and because of significant topographic changes as a result of the two paroxysms, the September 2019 model was aligned to the already referenced August 2019 model. We manually picked individual points e.g. prominent rocks or pinnacles of rock within outcrops of bedrock or an exposed dyke (Figure 2.3A). We assume that these features were stationary throughout the survey period but their appearance may have changed because of erosion, rockfall and pyroclastic deposition (Figure 2.3B–E). As

[1] `https://github.com/agisoft-llc/metashape-scripts/blob/master/src/read_altitude_from_DJI_meta.py` and `https://github.com/agisoft-llc/metashape-scripts/blob/master/src/add_altitude_to_reference.py`

a result, the individual reference points may vary for each survey. In general, four to seven points were used as reference without additional check points. The number of suitable available reference points was limited because the large extent of the areas affected by the two paroxysms had not been anticipated during survey design.

CloudCompare was used to reference the models to each other and to create the rectified DEMs. The referencing yields root mean square (RMS) errors of 0.39 m (May–June), 0.76 m (June–August), 0.39 m (August–September) and 0.33 m (June–January). For the inter-survey comparison of this study, this sub-metre relative accuracy is sufficient and accurate global positioning was not required. Most of the analysis was carried out with *QGIS*, where it was possible to attain and compare surface elevation, slope angles, crater rim heights and crater and/or vent geometry. For all the craters and vents identified we measured area, aspect ratio, circumference, height of crater rims, difference between highest and lowest point of the crater rim (Δh_{rim}) and the orientation of the highest and lowest point around the crater. Based on the difference between the highest and lowest sector of the crater, we calculated the slant angle of the crater exit plane. *QGIS* was also used to address the evolution of crater and/or vent positions as well as the vent surface cover (open versus debris covered). We used the additional UAV video footage to identify active covered vents, and inactive vents during the survey period that were not visible on the DEMs or orthomosaics.

2.3.5 Limitations

The aim of this study was to obtain the highest possible resolution of near-vent (within 100 m) topographic changes. Because of the proximity to the active vents, no ground control points (GCPs) could be placed within the area of interest. In an ongoing collaboration, our observations will be coupled with a study of topographic changes in a larger area above 700 m asl. Without reliable GCPs and check points, propagation of systematic error and artefacts is difficult to quantify. Although our DEM comparisons are useful for providing a first order impression of uncertainties, we cannot assess systematic positioning or reconstruction errors.

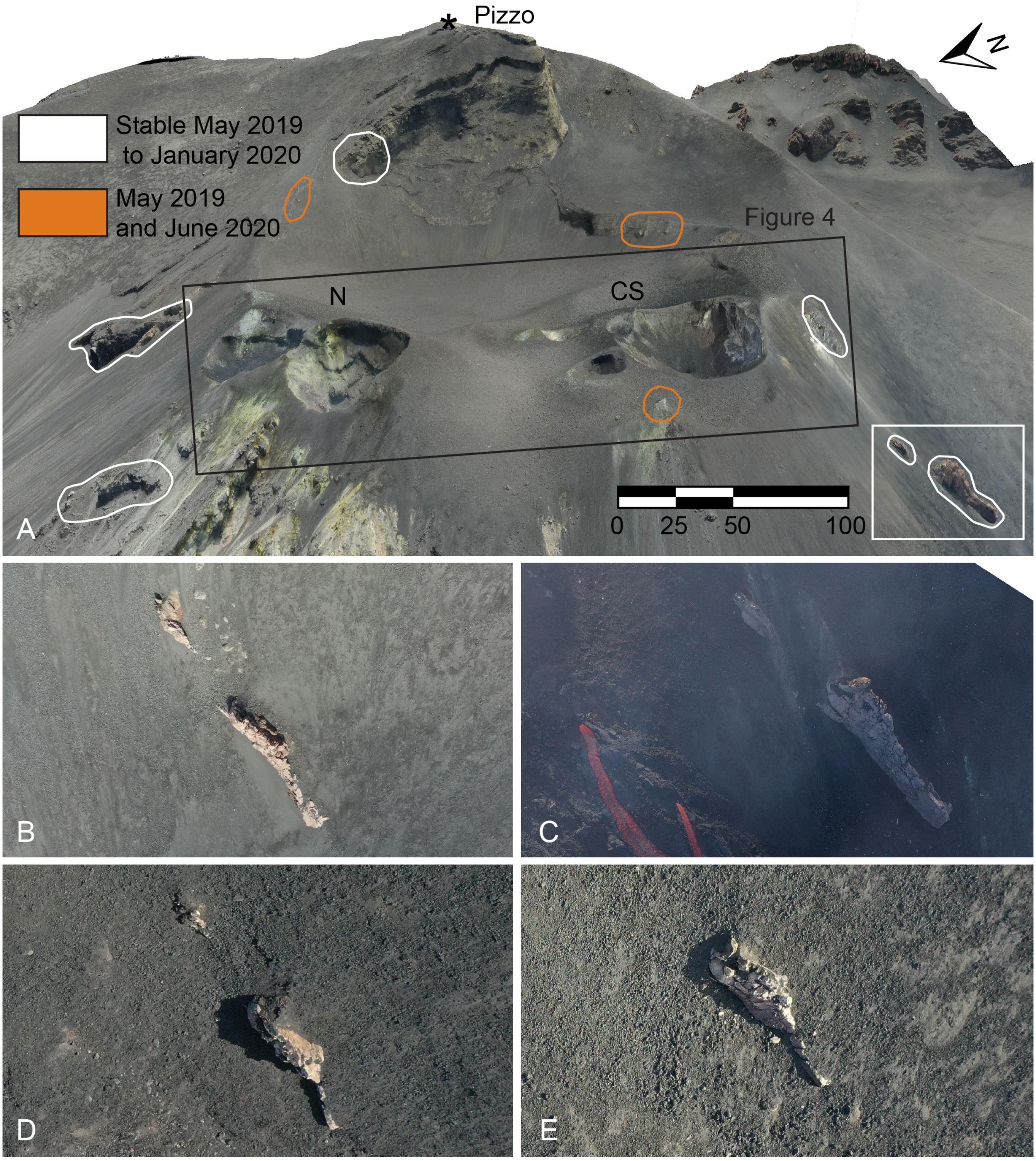

Figure 2.3: Location of features that were used for the referencing of the five models. (A) shows a 3D model of Stromboli's crater terrace in June 2019 indications for features that remained stable. The images in (B) May 2019, (C) August 2019, (D) September 2019 and (E) January 2020 show the dyke marked by the white rectangle. N marks the N vent area and CS the CS vent area. The black rectangle indicates the section shown in Figure 2.4.

2.4 Results

Our results show that the morphology of Stromboli's crater terrace and the geometry of craters and vents are transient on timescales of days to months.

2.4.1 Topographic changes of the entire crater terrace at the time scale of months

The comparison between May and June 2019 and between September 2019 and January 2020 show the changes caused by "normal" and elevated levels of activity (see Table A3 for levels of activity), while changes between June and August 2019 and between August and September 2019 were dominated by the two paroxysms and the effusive episode after the 3 July paroxysm.

During each campaign, we observed the conditions of crater topography (shape), fumaroles (strong or low degassing, "hot" or "cold") and active vents (open or closed) and any changes over day-to-month timescales. This allowed us to constrain quantitatively the impact of both constructive and destructive processes. Between May and June 2019 (~ 32 days) surface elevation changes ranged between −15 and +8 m in the survey area. In particular, negative height variations were restricted to the crater floors, while elevation gain occurred within small portions of the craters as well as in their surroundings. S1 was excavated by explosions, retrograde erosion and possibly subsidence. Gravitational instabilities affected the southern sector of S2 and led to elevation changes of up to −15 m (Figure 2.4). The paroxysm on 3 July 2019 removed at least 30 m (vertical) in the N and SC vent areas. The elevation changes between June and August (~ 53 days) were most apparent in the western portion of the SC area (between −10 and +16 m). On 23 September 2019, 26 days after the second paroxysm, up to 20 m of elevation was lost within S2 and the C vent area while elevation loss was −12 m in the N area. In January 2020, ~ 124 days after the previous campaign (September 2019), only positive elevation changes were detected with the strongest increases west of S2 and around N1 and N2. A maximum of +32 m was gained in the SC area, and +20 m in the N area. Elevation loss related to the explosive excavation by the 3 July and 28 August 2019 paroxysmal events was partially masked by lava effusion and pyroclast deposition.

2.4.2 Geometric changes of vents at the time scale of days

The prevailing processes shaping the N crater area on a timescale of 4 days in June were the deposition of pyroclasts, retrograde erosion along scarps, growth of two circular features within N1 and possibly subsidence (Figure 2.5). Pyroclast accumulation predominantly occurred within N1, while material loss from explosive excavation and/or subsidence dominated the crater floor of N2. Retrograde erosion was limited to a south-western section

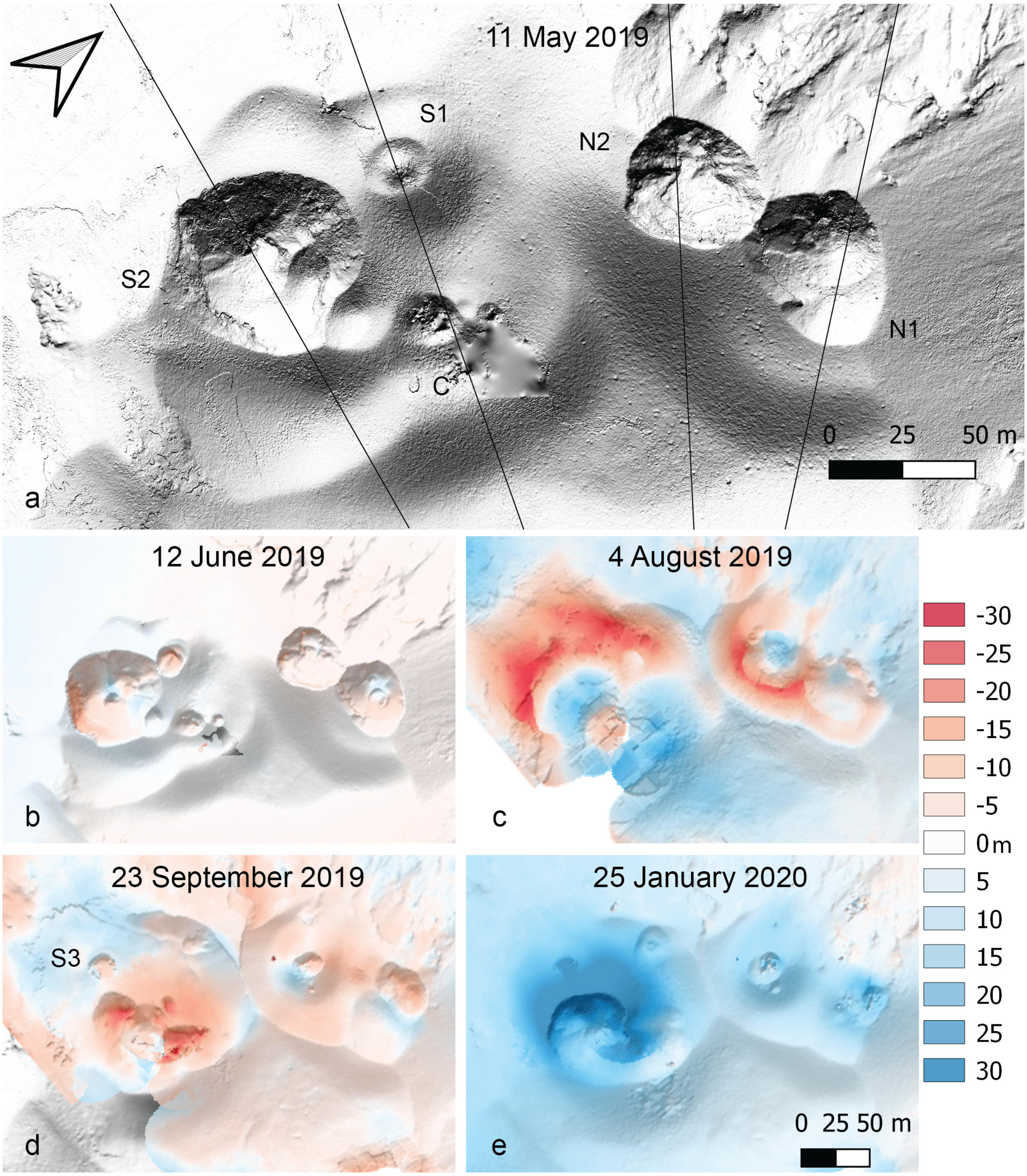

Figure 2.4: Topographic changes of the summit craters between May 2019 and January 2020 illustrated by DEMs. (A) shows a DEM of 11 May 2019. The coloured lines represent the transects shown in Figure 2.7 through S2, S1, N2 and N1 (left to right). The DEMs from June to January (B-E) show the topographic changes in relation to the previous one. All DEMs show the same section in the same orientation, arrow indicates North. Each colour of the colour key spans ± 2.5 m around the labelled value. Red colour represents negative elevation changes and blue colour positive elevation changes.

within N1 as well as the western and south-eastern portions of N2. The larger circular feature appeared to be a bank around the main vent within N1 outlined by erosion and/or the beginning of cone growth.

On 1 July 2019 at 05.40 am local time, a hornito inside S2 crater showed energetic Strombolian explosions with abundant pyroclast and subordinate ash ejection. These explosions were emitting sub-vertical jets with a symmetrical dispersal of pyroclastic material. Two days later, on the morning of 3 July 2019 at 06.26 am local time, the hornito had lost several meters of its height and had developed a small notch in the rim (Figure 2.1E, F). Intermittent activity was at a similar level on both days (A. Cristaudo, pers.comm.) yet the emitted jets and pyroclasts were directed towards the notch (Figure 2.1E, F).

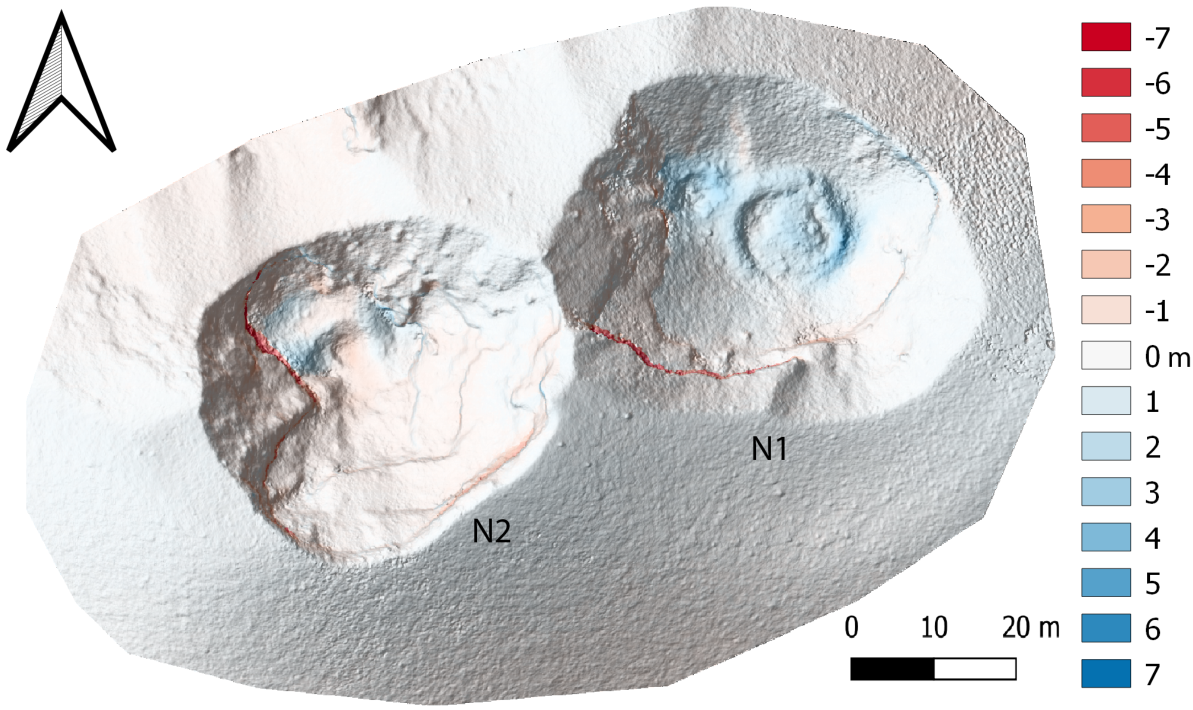

Figure 2.5: Topographic changes in N1 and N2 between June 8 and 12. Within this 4 day interval retrograde erosion altered the western wall of N2 and the south-western wall of N1 (dark red lines). Elevation gain is strongest within N1 visible as two circular features on the crater floor. Arrow indicates North. Each colour of the colour key spans ± 0.5 m around the labelled value.

2.4.3 Vent and Crater positions and crater terrace morphology

The SC and the N areas were persistent sites of volcanic activity throughout the study period, although the activity at some vents ceased, then sometimes resumed at the same or at close-by positions. The spatiotemporal evolution of the vents and craters are depicted in Figure 2.6.

N vent area

From May to June 2019 the diameter of N1 was reduced and, as a consequence, its shape changed, while N2 remained unchanged except for the elevation changes of the crater floor. In the beginning of August 2019, the morphology of the crater terrace was completely altered. Instead of two pronounced craters (N1 and N2), a total of 12 new vents emerged, and six of them exhibited incandescence. These were arrayed along a curved line 13 m and 23 m north of the previous centres of N2 and N1 craters (Figure 2.6A).

By September, the activity in the N area was focused on N1 and N2 at their new locations 8 (N2) and 27 m (N1) from their pre-paroxysm location. Additionally, a new fumarole was active between N1 and N2 at a location where two vents were situated in August 2019. In January 2020, a larger vent (~ 3×4 m) formed a cone with a new crater and two smaller vents a) at the rim of the crater and b) below the cone. A small (~ 0.5 m diameter) vent was active between N1 and N2 at a location where a fumarole was active in September 2019. The location of N2 did not change significantly from September 2019 to January 2020.

SC vent area

The crater diameter of S2 increased from May to June 2019 while the C vent remained unaltered. In early August 2019 the location of S1 shifted 13 m to the north and a new elongated vent (S3) became active on the western side of the crater terrace, around 46 m west of the position of S2 in June (Figure 2.6). By September 2019, S1 had shifted another 11 m to the west and S2 formed an elongated crater system together with two C craters. C1 crater was at the same location as it was in May and June, while a new fourth crater was visible 28 m north of the centre of the S2+C crater system. S3 changed from an ~ 30-m-long fissure to a circular crater with an ~ 18 m diameter. In January 2020, three vents were visible in the SC vent area (S1, S2, and C1). S1 was at the same location as in September, S2 had a similar crater size as in May but was at a new location. C1 was isolated from the S2 crater, close to C1's location in May, while C2 was not visible in January 2020 anymore.

The circumference of individual vents and craters was between and 46 and 227 m, with aspect ratios between 0.23 and 0.96. The height of the crater rim around the crater varied for each vent, in some cases considerably. N1 crater in June showed the biggest difference in Δh_{rim}. The NW side was 21 m lower than its highest point in the NE. With around 4 m in September, S3 exhibited the lowest difference in crater rim height. In combination with the crater diameter, for each crater we calculated the slant angle of the theoretical surface plane of the crater rim. These range from 10° (N2 January 2020) to 39° (S1 September 2019) and had an average slant angle of ~16° calculated from n=22 measurements.

We tracked the changes of N1, N2, S1, and S2 along four transects through the crater terrace (see transects in Figure 2.4A). The changes of N1 are illustrated in Figure 2.7A, where the edifice around the crater was growing over time, accompanied by crater enlargement between May and June 2019 (circumferences: 163 and 168 m). After the paroxysm on 3 July 2019, the location of N1 shifted towards the north and the circumference of the newly built crater was considerably smaller (131 m in September 2019 and 60 m in January 2020). Even though vent location and crater shape was modified by the events in July and August 2019, the southern crater rim of N1 was always higher than the northern crater rim. The difference between the highest and lowest point of the crater rim (Δh_{rim}) was 21 m in June 2019, changing to Δh_{rim} of 6 m in January 2020 (Table A1).

N2 (Figure 2.7B) showed a similar evolution (circumference: 150 m in May and June 2019, 67 m in September 2019 and 79 m in January 2020) but without a larger shift of the vent location. N2 Δh_{rim} was greatest in May and June 2019 (with 15 and 20 m, respectively), building up a small cone until the paroxysm on 28 August 2019. After this, N2 Δh_{rim} was reduced to 9 m in September 2019 and 4 m in January 2020.

The S1 transects of May and June 2019 show changes from cone to crater that was caused by a strong explosion on 15 May 2019. The transects through S1 also cut through the C crater (Figure 2.7C) and shows that the location of the C crater was stationary. Figure 2.7D shows transects through S2 (in May, June, September 2019 and January 2020). Strong elevation changes can be seen, including the removal of the crater rim (visible in May and June 2019 transects) and subsequent growth by pyroclastic accumulation (August 2019 – January 2020) at a new location.We compared our models (2019 and 2020) and photographs (2013–2019) with 1) sketches from 1994–2004 (Harris and Ripepe, 2007), 2) photographs from 2007–2012 (Calvari et al., 2014) and 3) a model from 2016 (Turner et al., 2017). These observations represent only snapshots in time and therefore interpreting a trend for small scale features development was not possible. However, interpolation between repeat surveys in a larger context might be useful. For example, from 1994 to 1997, the number of active vents in the N portion of the crater terrace decreased from 7 vents (5 hornitos, 2 with craters) to 2 craters with 1 vent each (N1 and N2). Also, from May 2000 to May 2001 the activity within C shifted as a hornito built up to the north of its pre- 2000 location, where activity ceased in 2002. During the same timespan, up to 4 vents were active within a locally stable crater in S. In 2004, probably as a result of the paroxysmal episode in 2003, the locations of N and S shifted eastward. In 2007 the entire crater terrace was a deep depression affecting all vent areas. Between 2008 and early 2011, the crater in S was increasing in size and a hornito in C transformed into a crater. This was occurring alongside the refilling of the crater terrace by pyroclastic deposits. With continued deposition, N migrated towards the scarp of the Sciara del Fuoco.

In September 2011, only ~2 vents in N and one vent in C were visible. This changed by September 2012 when there was a large crater in S formed by explosive excavation and an increased number of active vents in C. From 2013 to 2017, the changes were dominated by the enlargement and deepening of the crater in S and both craters in N probably due to a combination of explosive excavation and retrograde erosion of the crater rims. In May 2016 no vent was active in C, but activity resumed in 2017 as part of a larger S crater complex.

Table 2.1: Geometrical parameters of N1, N2, S1, S2, and S3 craters from May 2019 to January 2020 detailing area (A), circumference (C), long axis (a), short axis (c), the vertical difference between highest and lowest point of the crater rim (Δh_{rim}), the azimuth of the lowest point of the crater rim (AZM_{min}) and the dip angle of the theoretical surface plane between highest and lowest point of the crater rim ($\Theta_{surface}$).

Date	Name	A [m^2]	C [m]	a [m]	c [m]	Δh_{rim} [m]	AZM_{min} [°]	$\Theta_{surface}$ [°]
May 2019	N1	1898	163.0	51.4	43.1	16.5	24	20
June 2019	N1	1865	167.7	53.2	49.7	21.1	34	24
Sept. 2019	N1	1123	130.7	47.0	29.7	9.7	32	15
Jan. 2020	N1	271	60.0	21.4	16.7	6.4	23	20
May 2019	N2	1632	149.8	48.2	40.2	15.1	330	20
June 2019	N2	1637	149.7	47.9	40.0	19.7	324	27
Sept. 2019	N2	362	67.0	22.4	16.6	8.3	114	25
Jan. 2020	N2	461	78.9	26.1	21.6	4.2	113	10
June 2019	S1	285	72.6	19.9	17.9	4.7	119	14
Sept. 2019	S1	218	60.6	22.5	10.8	10.4	201	39
Jan. 2020	S1	463	86.7	32.5	20.6	7.2	269	16
May 2019	S2	3190	208.7	70.4	62.0	13.8	73	12
June 2019	S2	3742	227.4	76.6	69.0	18.3	66	15
Sept. 2019	S2+C	3671	259.0	96.7	43.2	26.8	242	23
Jan. 2020	S2	2324	184.7	56.4	52.7	11.2	54	12
Aug. 2019	S3	189	82.2	34.0	7.7	6.1	165	17
Sept. 2019	S3	330	62.6	20.0	19.1	3.9	359	12

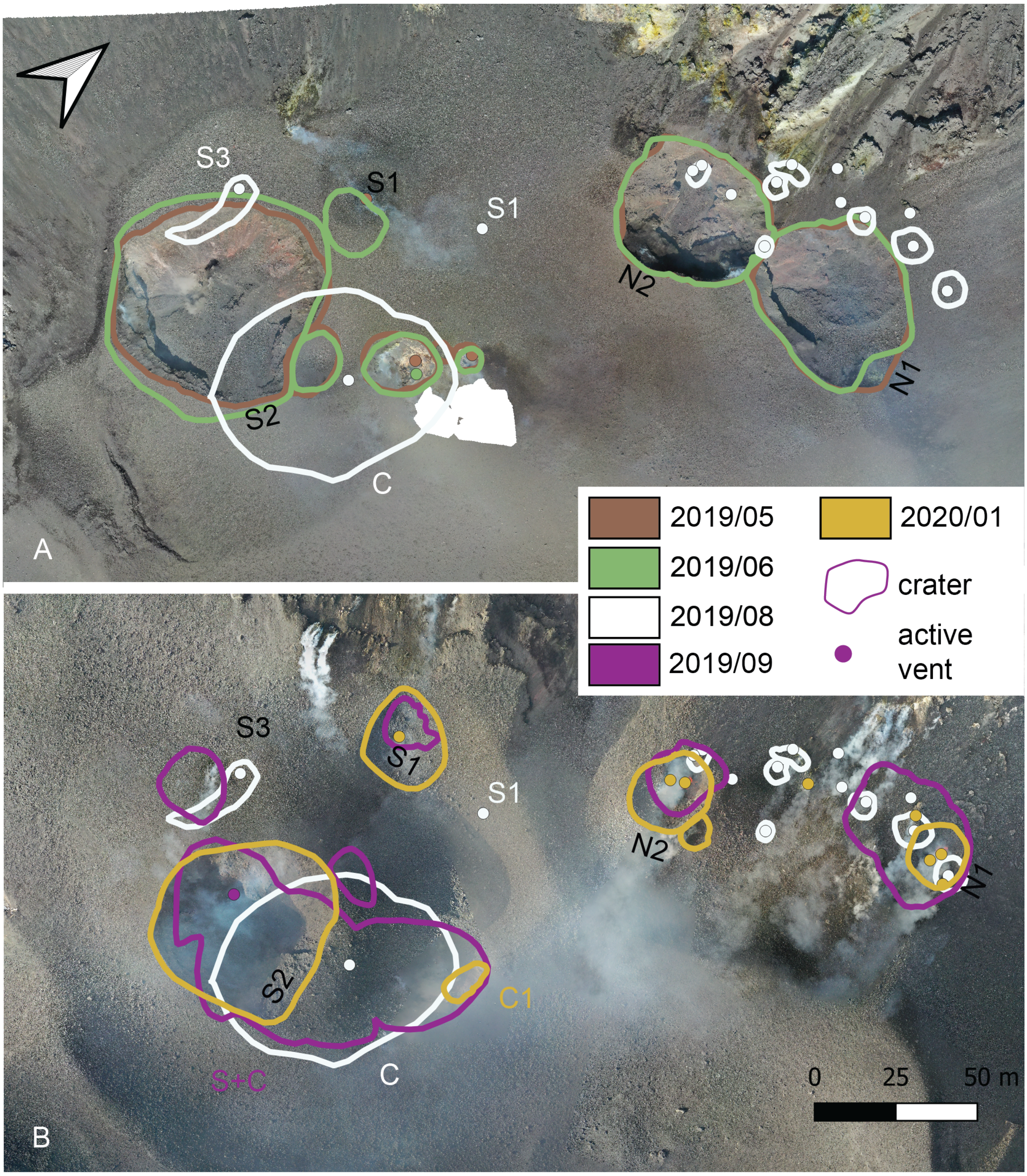

Figure 2.6: Orthomosaic of the area of interest between May 2019 and January 2020. (A) shows May 2019 with coloured outlines for crater shapes and open vents in May, June and August. (B) shows January 2020 with coloured outlines for crater shapes and open vents in August, September 2019 and January 2020. (A) and (B) show the same field of view. Arrow indicates North.

2.5 Discussion

2.5.1 Morphological changes of the crater terrace

We have used our data to evaluate the persistence of craters and vents at Stromboli's crater terrace. We found that the prevailing classifications of vents into two-to-three main centres of activity was applicable throughout the timespan of our observations. The position of craters and vents seem to be structurally controlled and we suggest that the S2 and C vents are aligned along a NE-SW trending feature that appears to be parallel to an old dyke west of the crater terrace (see Figure 2.3A). The paroxysm of 3 July 2019 excavated around 30 m of material, with explosions seemingly being produced by S2 and N2. This value is a conservative minimum, because lava effusion and explosive activity built up the crater terrace during 32 days between the paroxysm and data collection on 4 August 2019. The two paroxysms in 2019 have destroyed the uppermost (few tens of meters) plumbing system and replaced it by a zone of variably sized and cohesive fall-back material as already described by Calvari et al. (2014) for the period between 2007 and 2012. This heterogeneous zone provided additional pathways for magma to reach the surface and enabled the occurrence of the multitude of active vents in the N vent area visible in August 2019. However, it appears that the deeper plumbing system beneath the uppermost zone has not changed substantially, because the activity was soon re-focused into fewer active vents inside N1 and N2 craters. We suggest that the northward migration of N1 is surface morphology-controlled rather than being due to sub-surface structure. Since a large amount of material was removed in the area that now hosts N1 and the established conduit was partially destroyed, the new uppermost conduit of N1 migrated approximately 35 m north of its original location during the refilling of the crater terrace. We suggest that changes to the southern wall of N1 and to the western wall of N2 represent retrograde erosion of parts of the steep, and possibly overhanging crater walls.

During the last 26 years the crater has been subjected to opposing constructive and destructive processes. It seems that changing vent locations and openings of new vents promoted hornito growth. These hornitos were destroyed by explosions and/or collapse and the resulting craters were subsequently enlarged by explosive activity and erosion until a larger event eventually overprints the morphology.

2.5.2 Link between vent geometry and eruption dynamics

We observed changes to individual vents on timescales of days. The changes of vent geometry were accompanied by changes in style and direction of explosions. For example, until partial destruction of S1 in May 2019, the explosions were dominated by long-lasting (up to 50 s), sub-vertical gas-rich jets with incandescent pyroclasts. After this event, explosions were heavily laden with brownish ash, probably related to debris coverage of the vent due to backfall from explosions from other vents and erosion of the walls as described before by

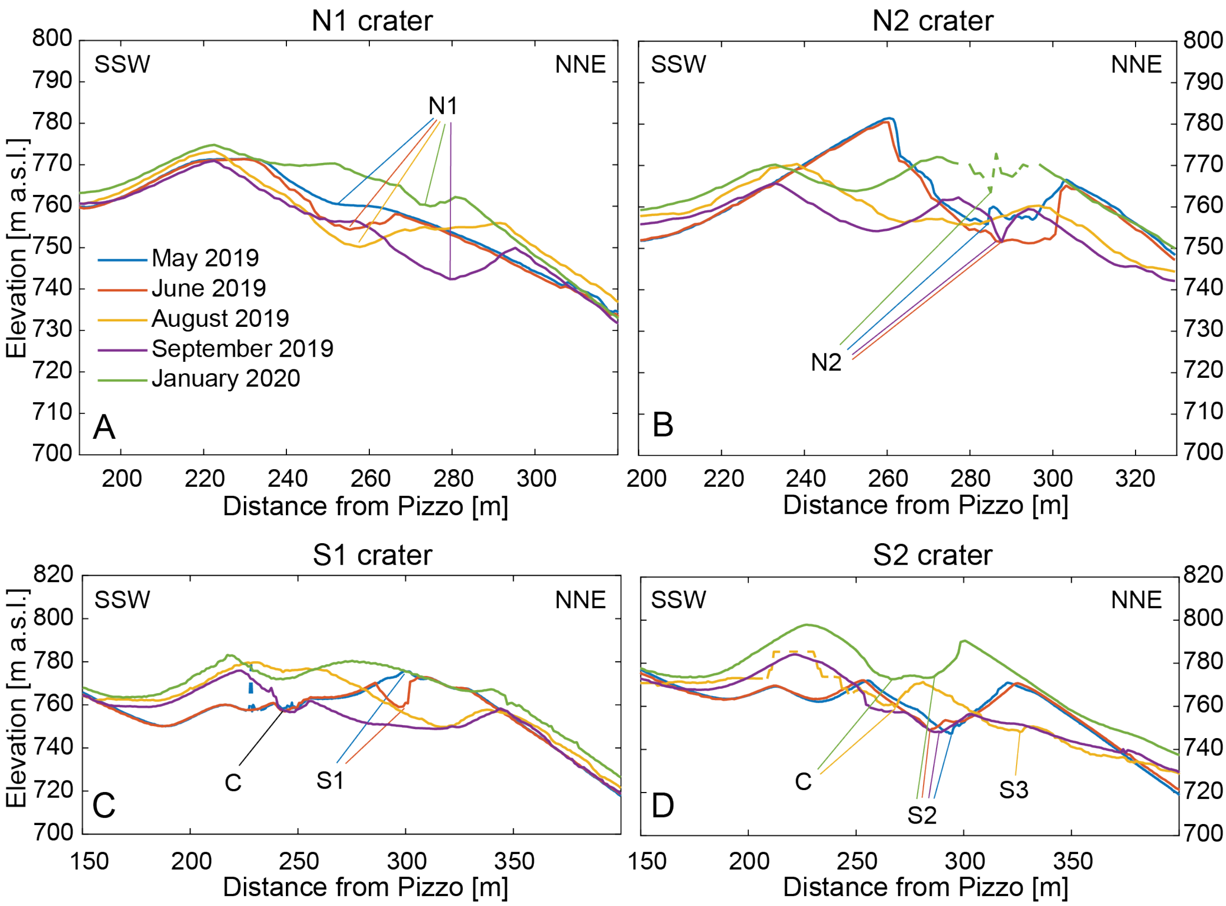

Figure 2.7: Transects through the craters of N1, N2, S1, and S2 as indicated in Figure 2.4 outlining the morphological evolution of the crater terrace. All transects start at the INGV thermal camera at Pizzo. Dashed lines indicate areas where artefacts influenced the profile.

Capponi et al. (2016) and Simons et al. (2020). The explosions and ballistic trajectories were directed towards the newly formed low side of S1 which may be relevant for risk assessment/hazard management (Figure 2.8). The partial destruction of the cone of S1 in May 2019 exposed the uppermost 12 m of a formerly cylindrical sub-vertical conduit. This confirms the impact of asymmetrical exit geometry on jet characteristics released from a vertical conduit.

The modification of S2 in early July 2019, shown in Figure 2.1E, F, is another example where short-term changes of the vent geometry led to directed explosions. This change occurred over few days and supports the assumption that the new direction of the explosions was a result of a modified exit geometry of the vent (Figure 2.1E, F). Previous authors have linked inclined explosions at Stromboli to conduit inclination (Zanon et al., 2009). We suggest that, for the two cases presented here (S1, May 2019; S2, July 2019), conduit inclination played no role in the change of direction of the explosions and that the inclined

explosions were solely based on the asymmetric crater and/or vent geometry. Further evidence of this is that the timescales over which the explosion behaviour changed (days) were too short to be a consequence of tilting (due to inflation or gravitational creep) of the crater terrace and the underlying plumbing system. The experiments of Schmid et al. (2020) confirmed that bilateral vent symmetry i.e. one side higher then the other (Δh_{rim}), produced inclined jets and asymmetric spreading angles despite a vertical conduit. These gas-only experiemts provided a link to the underlaying pure fluid dynamical processes related to complex vent geometries. The pyroclast rich events with variable-sized ejecta at Stromboli add complexities related to the coupling between particles and the gas phase, but the underlying principles remain valid.
Vents covered by debris may also impact the directionality of jets released from explosive eruptions. These processes have been documented by experimental studies of explosions of known energy, explosion depth and covering lithology by Graettinger et al. (2015b) and (Taddeucci et al., 2013b). At Stromboli, both open and covered vents have been observed.

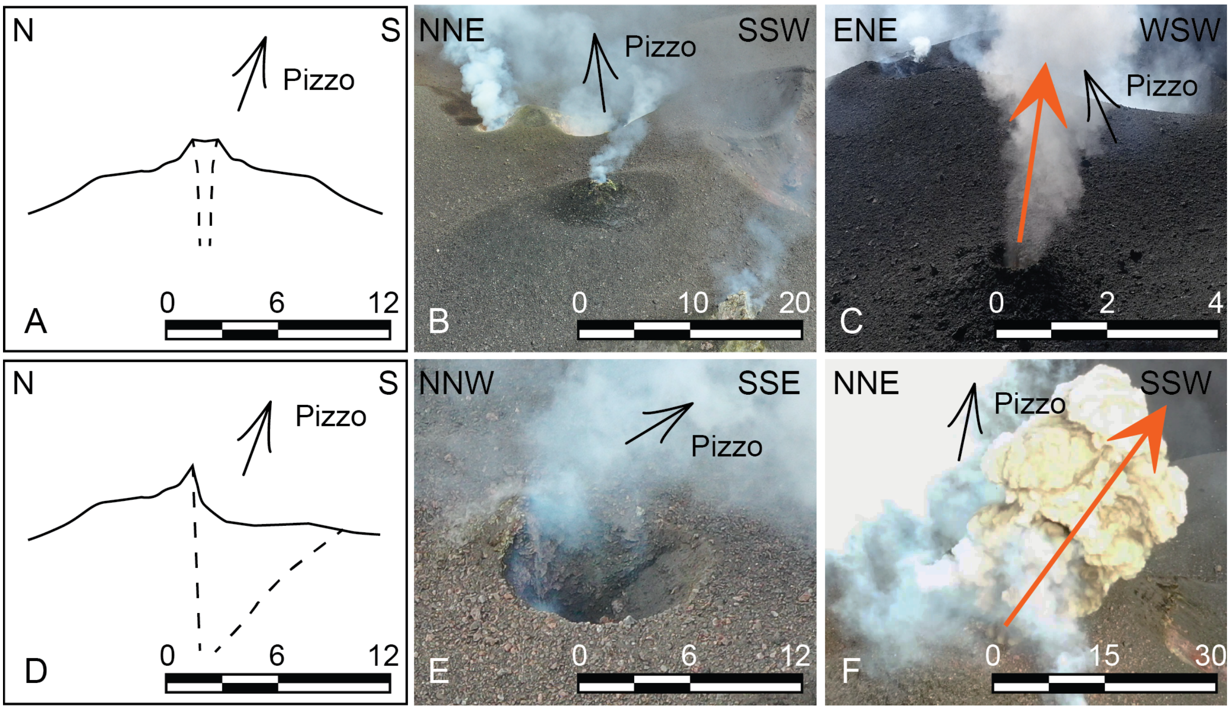

Figure 2.8: Vent geometry changes of S1 in May 2019 and the resulting modification of the eruption dynamics. A) shows a sketch of S1's geometry on 11 May 2019 (B) the corrsesponding image, (C) an associated gas-rich jet. (D) shows a sketch and [E] an image of the same vent's geometry on 15 May 2019 after the partial destruction. (G) shows an explosion on 15 May 2019 that is directed towards the lower (open) side of the crater rime of S1. Also visible is the changed composition of the jet with a significantly higher content of ash.

2.5.3 Towards a morphological monitoring of persistently active volcanoes

Spatiotemporal topographic data provides unique information that should be incorporated into multiparametric volcano monitoring, both to increase our understanding of eruptive processes and to better assess and mitigate specific hazards. Tourist-destination volcanoes are of prime importance for the local economy (Erfurt-Cooper, 2014). Several such volcanoes have decade long observations and there is some understanding of the frequency and magnitude of explosive eruptions that put the local population and tourists at risk (Bertolaso et al., 2009; Erfurt-Cooper, 2014). If the frequency of such events-to-be-avoided is low, permanent access bans may be difficult to enforce. The probability of ballistic impacts or inundation by pyroclastic density currents are two ways to define exclusion zones on active volcanoes (e.g., Alatorre-Ibargüengoitia et al., 2012; Romero et al., 2017; Lavigne et al., 2017; Romero et al., 2017; Toyos et al., 2007), frequently defining large portions of the volcano's flanks as off limits. On volcanoes where 1) continuous activity is believed to lead to limited risk of above-average magnitude explosions, 2) this number is small enough to be considered tolerable in the year-long average by the local civil protection and 3) with high agricultural and/or tourism pressure, topographic analysis of active vents at high spatial and temporal resolution may contribute to define risk areas or exclusion zones of substantially smaller extent and at potentially more frequent revision intervals. It is up to the local authorities if the resources for monitoring, observation and interpretation outweigh the economic interests of parts of the population to allow for such a symbiosis of human activity in potentially varying parts of a volcano. It goes without saying that access to agricultural land or tourist viewpoints is subordinate to public safety.

2.6 Closing remarks

Features of volcanic vents and craters exert a prime control on explosive volcanic activity. The data presented here show the development of the craters and vents at Stromboli volcano in unprecedented detail. The high temporal resolution allowed for a distinction between the effects of 'normal' activity and the elevated activity during the two paroxysms. In addition to qualitative description, it was possible to quantify geometry and morphology changes due to the high resolution of DEMs calculated from images taken during UAV surveys. Such surveys can be accomplished at short repeat intervals and at tolerable risk exposure for the pilot and their observer, which is important since the geometries can change on short timescales. High temporal and spatial resolution may allow quantification of as-yet unconstrained eruption parameters e.g. erupted mass, to date only indirectly — and crudely — known via measuring the degassing behaviour. At present, the limiting factor is the comparatively high error from the alignment of the models that could be improved by adding high quality GCPs or UAVs with real-time kinematic or post-processed kinematik (RTK/PPK) capabilities.

Long-term observations showed that crater and vent geometry can be stable or transient over periods of weeks to months ("normal" activity) but strongly altered during the two paroxysms in July and August 2019. Nevertheless, deeper portions of the shallow plumbing systems were seemingly unaffected as successive activity soon focused back to the three centres of activity as before the paroxysms. Moreover, "normal" eruptive activity with predominantly near-vent deposition of erupted material commonly rebuilt volcanic landforms resembling the pre-paroxysm configurations within weeks to few months.

Additionally, we observed the paramount impact of crater and vent geometry on pyroclast ejection characteristics, a fact that has strong implications for areas potentially affected by bomb impact and fall of pyroclasts. UAV photogrammetry can acquire unbiased data sets that have a much higher information content and comparison potential than photographs or sketches. DEMs enable high-quality measurements of predominant geometric features. Laboratory experiments showed that crater and vent geometry influence the directionality of volcanic jets. This parallels observations of changed eruptive behaviour and directionality following fairly sudden (hours to few days) geometric changes. Repeated UAV surveys can be used to evaluate risk areas, with low risk for the operators and with standard computational capabilities. A quantitative comparison of vent and crater geometry as well as crater terrace morphology was not possible due to the different media throughout the years. As Stromboli is frequently visited by scientists and UAVs are available in many working groups, large collective timeseries at high temporal and spatial resolution are achievable. Therefore, we made our DEMs, orthomosaics and processing reports publicly available (GFZ Data Repository: `https://doi.org/10.5880/fidgeo.2021.015`)

Chapter 3

Release characteristics of overpressurised gas from complex vents: implications for volcanic hazards

3.1 Abstract

Many explosive volcanic eruptions produce underexpanded starting gas-particle jets. The dynamics of the accompanying pyroclast ejection can be affected by several parameters, including magma texture, gas overpressure, erupted volume and geometry. With respect to the latter, volcanic craters and vents are often highly asymmetrical. Here, we experimentally evaluate the effect of vent asymmetry on gas expansion behaviour and gas jet dynamics directly above the vent. The vent geometries chosen for this study are based on field observations. The novel element of the vent geometry investigated herein is an inclined exit plane (5°, 15°, 30° slant angle) in combination with cylindrical and diverging inner geometries. In a vertical setup, these modifications yield both laterally variable spreading angles as well as a diversion of the jets, where inner geometry (cylindrical/diverging) controls the direction of the inclination. Both the spreading angle and the inclination of the jet are highly sensitive to reservoir (conduit) pressure and slant angle. Increasing starting reservoir pressure and slant angle yield 1) a maximum spreading angle (up to 62°) and 2) a maximum jet inclination for cylindrical vents (up to 13°). Our experiments thus constrain geometric contributions to the mechanisms controlling eruption jet dynamics with implications for the generation of asymmetrical distributions of proximal hazards around volcanic vents.

3.2 Introduction

Explosive volcanic eruptions are among the most energetic displays of Earth's internal forces. They pose continual threats to life and infrastructure. Such eruptions are fuelled by gas overpressure, which derives from volatile oversaturation of magma and its resultant degassing, sometimes combined with external volatiles such as vaporised meteoric water (Mayer et al., 2015). The overpressure driving melt vesiculation can be released explosively if it exceeds the tensile strength of magma, leading to failure and fragmentation (Alidibirov and Dingwell, 1996b; Dingwell and Webb, 1990). As a consequence, gas-particle jets of variable gas-particle ratio and grain-size distribution are emitted from vents at high velocity. Depending on jet temperature and the subsequent entrainment of ambient air, the eruption column can collapse and form pyroclastic density currents, or buoyantly rise into the atmosphere (Woods, 2010). Direct observations at volcanoes are limited to those accessible above the vent. What can be observed in the near-vent region is the result of a complex interplay of various source, path and exit conditions that affect the evolution of the related eruptive plumes. Directly above the vent, volcanic jets (composed of gas and pyroclasts) typically show the characteristics of underexpanded starting jets (e.g., Carcano et al., 2013; Kieffer and Sturtevant, 1984; Woods and Bower, 1995). The underlying physical principles of gas and multiphase flow have been investigated in both fluid dynamics (e.g., Arun Kumar and Rajesh, 2017; Deo et al., 2007; Peña Fernández and Sesterhenn, 2017; Sommerfeld, 1994; Tsuji et al., 1984) and applied engineering (e.g., Gutmark et al., 1989; Hokenson, 1986; Rice and Raman, 1993; Yin et al., 2016). However, their applicability for volcanic systems is limited because of the flow regimes considered and/or the assumption of sustained jets.

Several field studies (e.g., Andronico et al., 2009; Gaudin et al., 2014; Taddeucci et al., 2012) have revealed that ejection processes are both dynamic and intricate, exhibiting for example significant ejection velocity variations during single eruptive pulses and complex propagation of gas-particle jets and eruption plumes. Both initially inclined eruption columns as well as directed explosions yielding eruption deposits on a small sector of a volcano have been observed (e.g., Mount St. Helens 1980, Moore and Sisson (1981); Bezymianny 1956, Belousov et al. (2007)). The 1984 eruption of Mayon volcano, Philippines, produced a basal thrust column that had a tilt to the southeast, leading to fountain collapse and a preferential emplacement of pyroclastic flows down the south-eastern flank of the volcano (Lagmay et al., 1999). An asymmetric crater has been cited as the reason for the directed jets rather than wind or an inclined conduit driving the laterally focused propagation (Lagmay et al., 1999). Whereas atmospheric factors such as wind may exert a strong control on the buoyant phase of these plumes and add a lateral dimension to their transport, large and strongly convecting eruptive plumes may remain apparently unaffected even in the event of storms (Pinatubo 1991, Holasek et al. (1996)). Similarly to Mayon, an irregular crater morphology was proposed by Cole et al. (2015) for Soufrière Hills volcano, Lesser Antilles, as the controlling force for directed ballistics and fall out dispersal related to explosive activity on 17 September 1996, 5 December 2008 and 11

February 2010. In May 2008 the eruption of Chaiten volcano, Chile, produced pyroclastic flows on the northern flank of the volcano that appear to have been generated by "directionally focused" explosions (Major et al., 2013). Thus it appears that directionality of eruptive products is often controlled by the geometry of craters and/or vents and is not necessarily associated to the failure of a volcanic edifice (Cole et al., 2015).

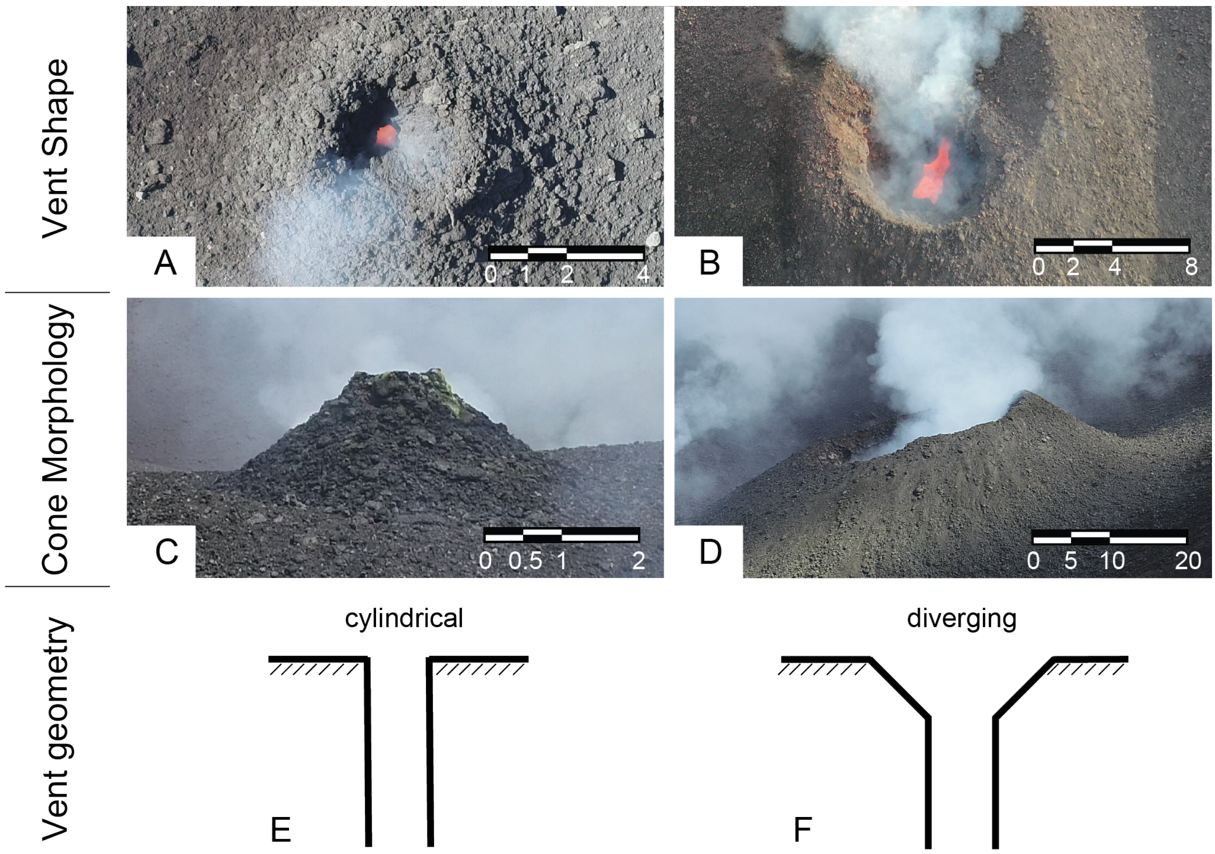

Figure 3.1: Field images acquired at Stromboli Volcano, Italy, by uncrewed aerial vehicle. The first row shows examples of the variability of vent shapes; (A) shows a circular vent, while (B) shows a highly irregular vent. The second row shows the cone morphology with symmetric (C) and asymmetric (D) vent exit heights. The third row shows sketches of the shallow subsurface with a cylindrical (E) and a diverging (F) geometry. The vent geometries used in the experiments presented in this study represent a combination of circular (a) vent shape with asymmetric (D) vent exit heights with either a cylindrical (E) or diverging (F) subsurface geometry.

Vent geometry and its influence on eruption dynamics have been the focus of several studies so far. The vent size influences jet diameter and thereby mass eruption rate (e.g., Jessop et al., 2016; Koyaguchi et al., 2010; Ogden, 2011; Saffaraval et al., 2012). Valentine (1997) suggested that narrow vents and high exit velocities favour the generation of buoyant plumes. Jessop and Jellinek (2014) investigated the effect of vent geometry on entrainment characteristics of volcanic jets. They found that air entrainment is more efficient for diverging vents because of a larger surface of the jet's boundary layer due to particle inertia and trajectory. The effect of geometry on plume dynamics has been assessed in studies focusing on ejection velocity (e.g., Kieffer, 1989; Wilson and Head, 1981; Wilson et al., 1980) and jet radius (e.g., Jessop et al., 2016; Woods and Bower, 1995; Woods and Caulfield, 1992). A flaring vent can aid the transition from subsonic to supersonic flow (e.g., Kieffer, 1989; Wilson and Head, 1981; Woods and Bower, 1995), assuming that the ejection velocity of gas and gas-particle mixtures is mainly governed by gas overpressure, gas mass fraction and temperature (Woods and Bower, 1995). These studies showed that vent geometry can increase the surface area or the velocity of the volcanic jet and therefore enhance air entrainment favouring a buoyant plume over a collapsing column (Valentine, 1997). However, they did not investigate how irregular, asymmetric vents or dynamically evolving vent geometries affect eruption dynamics.

Volcanic edifices have been observed with highly variable topography, notched craters and slopes, hosting one or more open or (partially) clogged vents of variable shape (Figure 3.1). The geometries are subject to rapid changes during a single eruption or throughout the course of several events. To date, irregular vent geometry, varying fragmentation depth and/or directionality of the underlying explosion source have been inferred as causes of asymmetric dispersal of material in scaled experiments (e.g., Graettinger et al., 2015a, 2014; Valentine et al., 2012b). So far, only a small number of studies have investigated the effects of vent enlargement on the dynamics of jets (Solovitz et al., 2014) and only for sustained jets. Jessop et al. (2016) tested the probability of column collapse based on the shape of the vent for symmetric annular and linear vents. Lagmay et al. (1999) combined observations and numerical models to link asymmetry in the crater area to preferential flow directions of pyroclastic flows. By employing Computational Fluid Dynamics with a geometric analogue to a shock-tube setup they simulated jet behaviour for a range of stagnation pressures. They found that the location of (partial) column collapse — and associated direction of pyroclastic density currents is controlled by crater geometry and eruption exit pressure, but they did not consider the dynamic evolution of the exit pressure. Volcanic explosions are sudden, instantaneous events from highly variable vents (Figure 3.1) during which most if not all governing parameters such as magma textures and overpressure (i.e. gas-particle ratio), fragmentation efficiency (i.e. particle size), eruption depth and intensity (i.e. conduit and vent geometry, Figure 3.1) vary and evolve with time. A holistic description of explosive eruptions has been attempted through several approaches, yet, to date, all approaches suffer from a lack of precision at some scale. Experimentally, shock-tube experiments have been used extensively to mimic such starting jets at controlled, reproducible conditions (e.g., Alidibirov and Dingwell, 1996a; Anilkumar et al., 1993; Cigala et al., 2017; Dellino et al., 2014; Kieffer and Sturtevant, 1984; Kueppers et al., 2006a,b) and serve as a basis for numerical models (e.g., Lagmay et al., 1999; Ogden et al., 2008b; Sommerfeld, 1994).

Scaled shock-tube experiments have also been used to decipher the impact of source, path and exit conditions on volcanic phenomena. The poorly constrained to completely unconstrained boundary conditions of volcanic explosions (e.g., pressure, temperature, magma textures, particle concentration and grain size distribution) can be controlled in experiments and varied systematically. Cigala et al. (2017) revealed a general non-linear decay of particle exit velocity, governed by (1) tube length, (2) particle load, (3) vent geometry, (4) temperature, and (5) particle size. They showed that vent geometry controls gas flow which in turn affects particle dynamics. To reveal the influence of complex geometry on gas expansion dynamics without any possible feedback from particles, pure gas jets have been the focus of this study. Accordingly, we modified two (cylinder and diverging 15°) of the radially symmetric geometries of Cigala et al. (2017) that showed the strongest influence on gas-particle ejection. The novelty is a slanted exit plane (5°, 15°, 30°) to decrease the level of symmetry resulting in six new vent geometries.

3.3 Methodology

3.3.1 Experimental setup

For our scaled shock-tube experiments, the "fragmentation bomb" (Alidibirov and Dingwell, 1996a; Kueppers et al., 2006a,b; Spieler et al., 2004) has been used, with modifications building on those introduced in Cigala et al. (2017). The high-pressure high-temperature section (autoclave, Figure 3.2) is separated from the low-pressure section (at ambient conditions) by a set of three diaphragms that allow for incremental pressurisation of the autoclave (with Argon) to the experimental pressure. When the desired experimental pressure in the autoclave is reached, rapid decompression of Argon is triggered and the resulting pressure drop (> 1 GPa/s, Spieler et al. (2004)) automatically triggers the recording system. The gas expands forming an underexpanded starting gas jet at the vent.

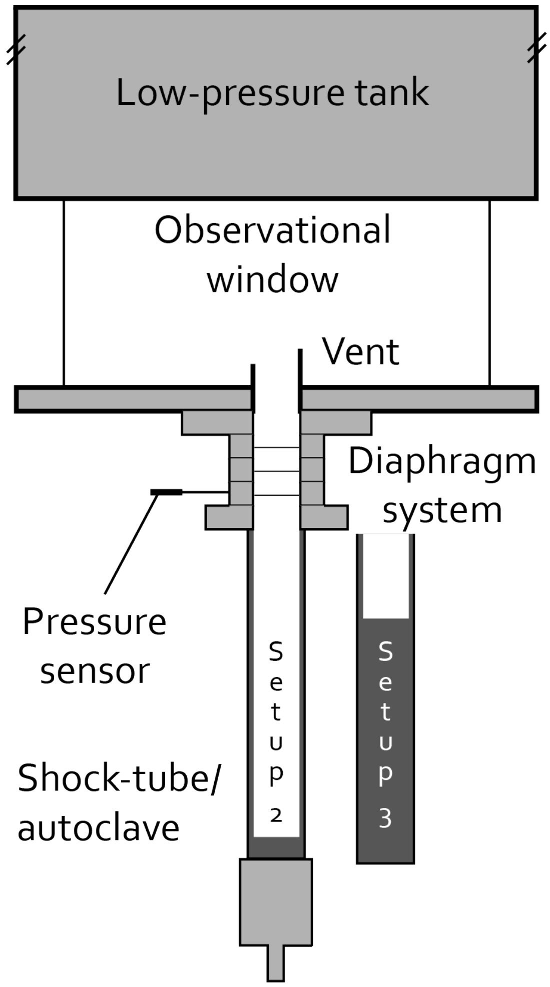

Figure 3.2: Shock-tube setup at LMU Munich consisting of the high-pressure section, the diaphragm system controlling pressurisation and the low-pressure section. The latter consist of the observational window and the tank that can be used for particle collection. Two setups with different autoclave volumes were used (setup 2: 127.4 cm^3, setup 3: 31.9 cm^3).

3.3.2 This study

Based on the findings of Cigala et al. (2017), we chose to adapt two geometrical configurations that showed the strongest effect on gas-particle jets: cylindrical and diverging (15°) inner geometry. For both configurations, vents with three different slant angles of the top plane (5, 15 and 30°) were fabricated (1.4305 NiCr steel, 28 mm conduit diameter, resulting in six vent geometries (see Figure 3.3) with bilateral symmetry. All vents were designed to reproduce conduit length as in Cigala et al. (2017), i.e. with a vent exit height of 50 mm on the lower side. The used slant angles were inspired by the geometry of eruptive vents at Stromboli volcano, Italy (see Figure 3.1). We observed circular, symmetric vents as well as irregular and asymmetric vents. One of the most frequent asymmetrical features was a varying rim height around craters and vents (see Figure 3.1D). We mimic this aspect with the slanted exit plane in our vent designs. A detailed characterisation of crater and vent geometries as well as their temporal evolution over a nine-month timespan based on UAV surveys can be found in Schmid et al. (2021).

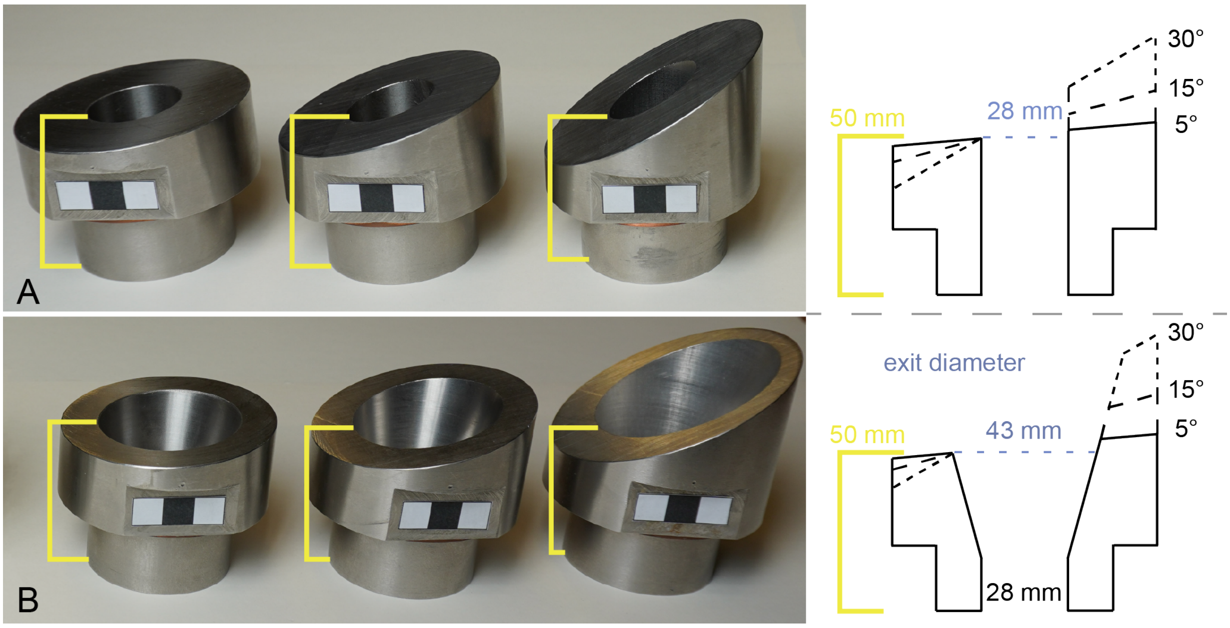

Figure 3.3: Six vent designs with bilateral symmetry. The inner geometry is either cylindrical (cyl) or a 15° diverging funnel (fun) and was selected based on the strongest impact in experiments of Cigala et al. (2017)Cigala et al. (2017). The added vent geometry complexity is a slanted exit plane. 3A left to right: cyl05, cyl15, cyl30 and a sketch of a section through the vent. 3B left to right: fun05, fun15, fun30 and a sketch of a section through the vent. The height of the lower vent exit is identical for all geometries with 50 mm above the base of the vent (yellow mark). The upper side's height is 52.5, 57.5 and 66 mm (cylindrical vents) and 54, 62 and 80 mm (diverging vents) above the base. Black squares used for scale 1×1 cm.

Experiments were performed at constant temperature (25° C), four pressure steps (5, 8, 15, 25 MPa) as well as two reservoir (autoclave) volumes (setup 2: 127.4 cm^3, setup 3: 31.9 cm^3; see Figure 3.2). For the four starting reservoir pressures the theoretical maximum pressure at the vent exit was calculated by applying one-dimensional isentropic theory (1.10, 1.67, 2.80 and 4.25 MPa for the cylindrical vents as well as 0.15, 0.21, 0.30 and 0.32 MPa for the diverging vents, respectively). Each experiment is triggered intentionally, generating a vertically expanding gas jet that eventually leaves the vent. Initially, the gas expands longitudinally within the shock-tube until the expansion front reaches the vent exit. From this point, the gas can expand radially forming a starting jet with turbulent eddies generated by shear between the jet and the stagnant atmosphere that will entrain ambient air. Due to decompression, the expanding Argon condenses and allows visual observation of the gas dynamics.

A Phantom V711 high-speed camera was used to record the experiments at 10,000 frames per second at a resolution of 1280×600 pixels, covering a field of view of approximately 22×10 cm. The videos were recorded from a point orthogonal to the symmetry plane of the vent and centred on the vent axis.

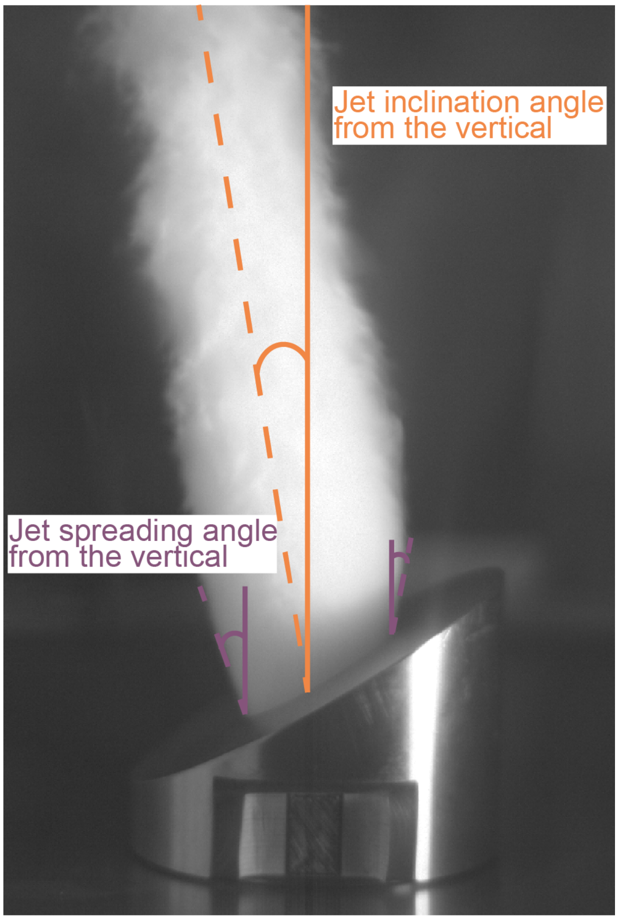

Figure 3.4: Measurement of gas spreading angle (purple) and jet inclination (orange). Gas spreading angle was always measured between vertical and a tangent at the jet boundary on the low and high vent exit. Jet inclination angle was measured as the deviation of the jet from the vertical centreline above the vent.

Scaled single frames were exported and manually analysed with ImageJ. The gas spreading angle (Figure 3.4, purple) was always measured between the vertical and a tangent at the jet boundary at the lower and higher vent side. Jet inclination was determined as the deviation from the vertical centreline of the gas flow (Figure 3.4, orange). Driving medium, starting pressure and temperature are controlled precisely and the geometry is constant. Several studies (e.g., Alatorre-Ibargüengoitia et al., 2011; Cigala et al., 2017; Kueppers et al., 2006b) showed the reproducibility of repetitive experiments with heterogeneity of natural samples having the biggest impact. Here, no samples were part of the experiments. The opening of the diaphragms is sometimes imperfect. The state of the ruptured diaphragms after each experiment was controlled visually and only experiments with diaphragm opening that did not satisfy our criteria were repeated. In our experiments, the largest source of inaccuracy is the subjective error when manually and optically determining the centre streamline and the boundary layer of the jet to measure its spreading and inclination. Hence, measurements of jet spreading and inclination were repeated at least twice with selected experiment being analysed by two individuals for an unbiased assessment.

3.3.3 Scaling

Two experiments are similar, if they have the same non-dimensional parameters. Two different explosions at vastly different scales, e.g. in nature and in the laboratory, are equivalent, if all nondimensional parameters match. In practice, full similarity in all parameters at the same time is not possible. To evaluate the differences between nature and experiments, it is crucial that the dynamics of the explosion are at least comparable. Since our vents are a modification of the vent geometries used by Cigala et al. (2017), we employed the same non-dimensional analysis of the flow conditions. We focused on the Reynolds number (Re) and the Mach number (M) for our vent geometries to describe the fluid flow dynamics. Re represents the ratio of inertial to viscous forces in a flow and is defined as:

$$\mathrm{Re} = \frac{\rho U L}{\mu}$$

where ρ is the fluid density, U is the fully expanded flow velocity, L is a characteristic length e.g. the vent radius (in our case) (Clarke, 2013) or the jet diameter (Kieffer and Sturtevant, 1984) and µis the viscosity at the temperature of the fully expanded condition. The reference quantities in our experiments were calculated by using the one-dimensional isentropic theory (Oswatitsch, 1952) by estimating gas density, viscosity and flow velocity for our experimental temperature and pressures (see Table 1 for gas properties of Argon). The Re for our experiments was between 2.22×10^7 (cylindrical, 5 MPa) at the vent exit and 9.09×10^8 (diverging, 25 MPa) at fully expanded conditions. Re for volcanic eruptions is reported to be between 10^5 and 10^8 (Clarke, 2013) or as high as 10^{11} (Kieffer and Sturtevant, 1984). Furthermore, this way of scaling has proven to be viable for rapid decompression experiments (e.g., Cigala et al., 2017; Dellino et al., 2014; Dioguardi et al., 2013).
The flow Mach number was estimated by the following relationship (Saad, 1985):

$$\frac{\mathrm{A}_2}{\mathrm{A}^*} = \left(\left(\frac{2}{\gamma+1}\right)^{\frac{\gamma+1}{2(\gamma-1)}}\right)\frac{1}{M}\left[1+\left(\frac{\gamma-1}{2}M^2\right)\right]^{\frac{\gamma+1}{2(\gamma-1)}}$$

where A_2 is the area of the exit (28 mm for the cylindrical vents and 43 mm for the diverging vents; see Figure 3.3 for the 2D representation of the exit area) and A* the critical area (26 mm). A* is defined as the narrowest cross-sectional area the gas flow has to pass during expansion and is located at the top of the sample chamber. The exit (A_2) to critical (A*) area ratios were 1.16 and 2.73 for the cylindrical and diverging inner geometry, respectively. The heat capacity ratio γ was estimated for each experimental pressure resulting in Mach numbers between 1.54 and 3.82 for the cylindrical inner geometry at 5 MPa and the diverging inner geometry at 25 MPa (Table 2). All values for Re and M presented here represent maximum values that are, due to the dynamic nature of these type of experiments, only valid at the beginning of the experiment.

Table 3.1: The fluid properties of argon at 25° C at the experimental pressures used in this study. Density, viscosity, speed of sound, Cp (specific heat capacity at constant pressure), Cv (specific heat capacity at constant volume) and R (gas constant) have been retrieved from Linstrom and Mallard (2000). The heat capacity ratio (γ) was calculated as $\gamma = \frac{Cp}{Cv}$.

Pressure [MPa]	Density [kg/m^3]	Viscosity [Pa*s]	sound speed [m/s]	Cp	Cv	γ	R
0.1	16.223	2.27E−05	322.33	0.52	0.31	1.67	209.15
5	82.911	2.38E−05	327.19	0.58	0.32	1.81	262.81
8	134.37	2.47E−05	332.65	0.62	0.33	1.91	297.92
10	169.05	2.55E−05	337.22	0.65	0.33	1.98	321.4
15	255.55	2.77E−05	351.96	0.71	0.34	2.12	376.57
25	416.71	3.32E−05	393.89	0.80	0.35	2.30	450.94

Table 3.2: Nondimensional numbers calculated cylindrical and diverging inner geometries at the experimental pressures used in this study. Mach number (M) was calculated at the lower vent exit height. Reynolds number (Re) was calculated at the throat of the vent, the lower vent exit height and at fully expanded conditions. The characteristic length used to calculate these values is the vent exit diameter (28 mm for cylindric vents and 43 mm for diverging vents).

Pressure	M	Re		
	Exit	Throat	Exit	Fully expanded
Cylindrical				
5	1.5	2.22E+07	2.85E+07	3.31E+07
8	1.6	3.58E+07	4.77E+07	6.78E+07
15	1.6	6.73E+07	9.69E+07	2.21E+08
25	1.6	1.06E+08	1.64E+08	5.92E+08
Diverging				
5	3.1	2.22E+07	4.98E+07	5.09E+07
8	3.2	3.58E+07	9.48E+07	1.04E+08
15	3.5	6.73E+07	2.55E+08	3.40E+08
25	3.8	1.06E+08	5.51E+08	9.09E+08

3.4 Results

We focus here on the analysis of two features of the gas dynamics: *jet spreading* and *jet inclination*. Figure 3.5 illustrates the temporal evolution of jet dynamics as a function of autoclave overpressure and vent geometry. The colour-coded jet outlines represent three pressure starting conditions, columns and rows represent six geometries and four time intervals, respectively. We observed a strong influence of pressure ratio, slant angle and inner geometry on the dynamics of gas jets (Figures 3.5 and 3.6). The images are still frames extracted from high-speed videos showing a condensing gas jet. In the first row, the images show the expanding gas 0.8 ms after the visual onset of gas ejection. The flow is choked at the system throat and underexpanded. At this time, asymmetry of gas expansion is visible via a larger extent of the jet towards the lower vent side (left side in Figure 3.5). After 4.3 ms, gas jets from experiments starting at 25 and 15 MPa reservoir pressure are still underexpanded, while the initial overpressure in experiments with 5 and 8 MPa has already been accommodated. Now, jet asymmetry becomes even more apparent. The jets emitted from vents with the cylindrical inner geometry are inclined towards the side of the lower vent exit; jets emitted from the diverging vents are inclined to the opposite direction with an increasing inclination for diminishing underexpanded flow conditions.

By comparison of data from 7.3 and 8.3 ms one can observe the effects of pressure decay of the reservoir. For jets produced by experiments with 8 MPa initial pressure the boundary layer between jet and atmosphere becomes increasingly diffuse and the jet exhibits undulating motion at around 7.3 ms. In case of the diverging geometry the flow detaches from the vent when gas spreading angle drops below the 15° slope angle of the diverging part of the geometry. Late (8.3 ms), only the jets created from 25 MPa initial pressure are still underexpanded.

3.4.1 Jet spreading

The maximum gas jet spreading angle was sensitive to reservoir overpressure and slant angle of the exit plane (see Figure 3.6A). Spreading angles evolved with time, showing a fast build-up to the maximum value and then a slower decay. Figure 3.6A reports the maximum spreading angle on the lower vent side that was achieved for individual experimental conditions. The pressure ratio was found to be of paramount influence on the maximum gas jet spreading angle, with higher pressure ratios causing larger spreading angles. Vents with cylindrical inner geometry had spreading angles that were, depending on reservoir pressure, between 5° and 20° larger than for diverging vents. Furthermore, for identical inner geometry and reservoir pressure, a positive correlation between spreading angle and slant angle as well as reservoir pressure was observed. When comparing results of setup 2 and 3, a positive correlation of initial gas reservoir volume and maximum spreading angle of the gas jet could be observed. The difference between maximum spreading angle on the lower and upper vent side is controlled by inner geometry and slant angle (Figure 3.7). For

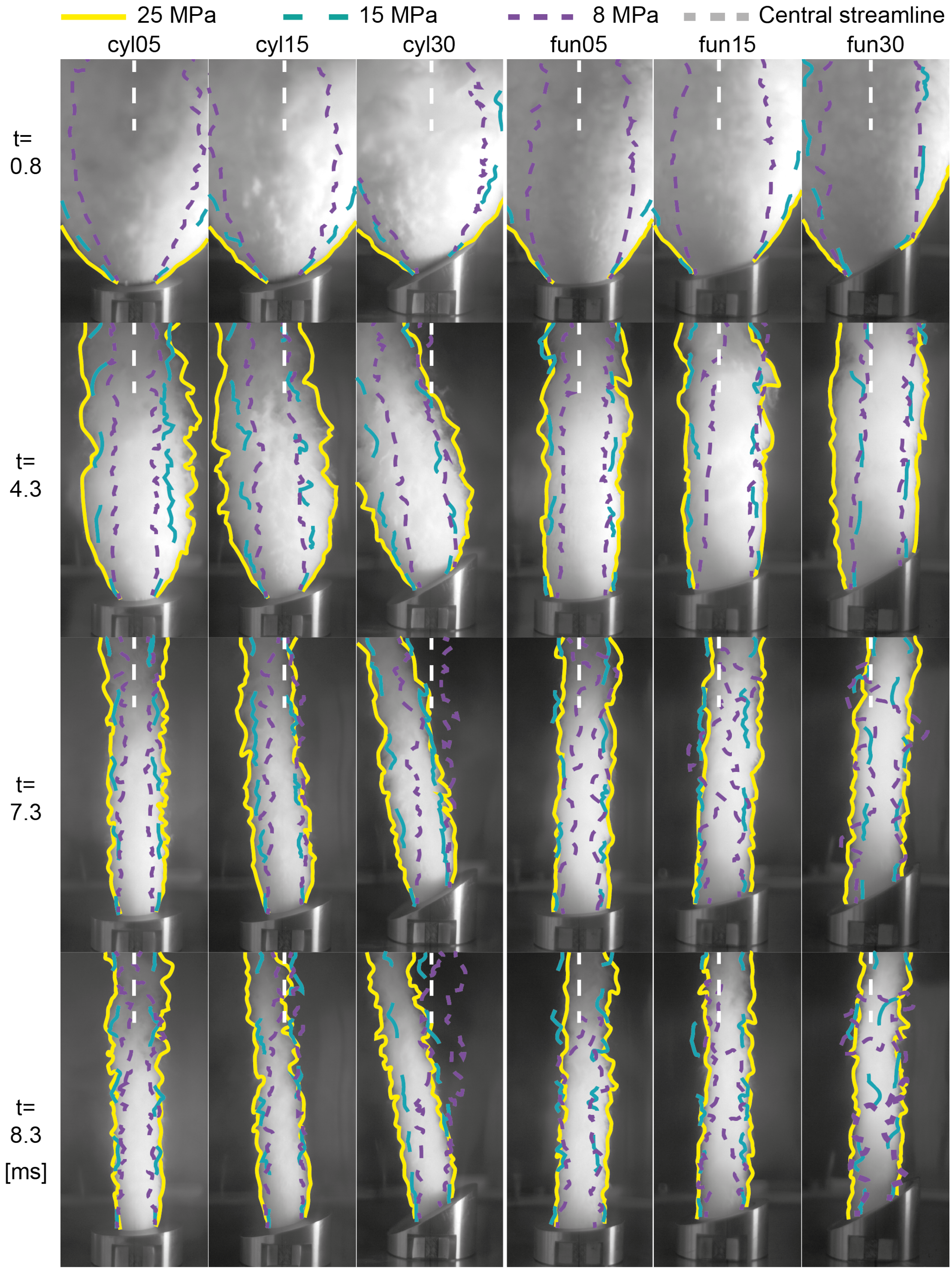

Figure 3.5: Gas-only experiments reveal a strong dependency of jet inclination to slant angle of the exit plane and reservoir pressure. Thereby, large slant angles and high-pressures cause a higher degree of tilt from the centreline. The six columns represent six different vent geometries (cyl05, cyl15, cyl30 have a cylindrical inner geometry and 5, 15 and 30° slant angle; fun05, fun15, fun30 are vents with 15° diverging inner geometry and 5, 15 and 30° slant angle respectively). The four rows represent different times after the first gas ejection (0.8, 4.3, 7.3, 8.3 ms). The coloured outlines mark different reservoir pressures (yellow 25 MPa, blue 15 MPa, purple 8 MPa). The underlying image shows an experiment at room temperature and 25 MPa initial overpressure.

cylindrical vents, the slant angle has little effect on the spreading angle and the difference between lower and upper side is generally small (around 2°). For diverging vents with 30° slant angle the difference is between 8° and 14° with the smallest difference in experiments with 25 MPa. For diverging vents with 15 and 5° slant angle the difference is generally smaller (between 0° and 8°, and 2–3°).

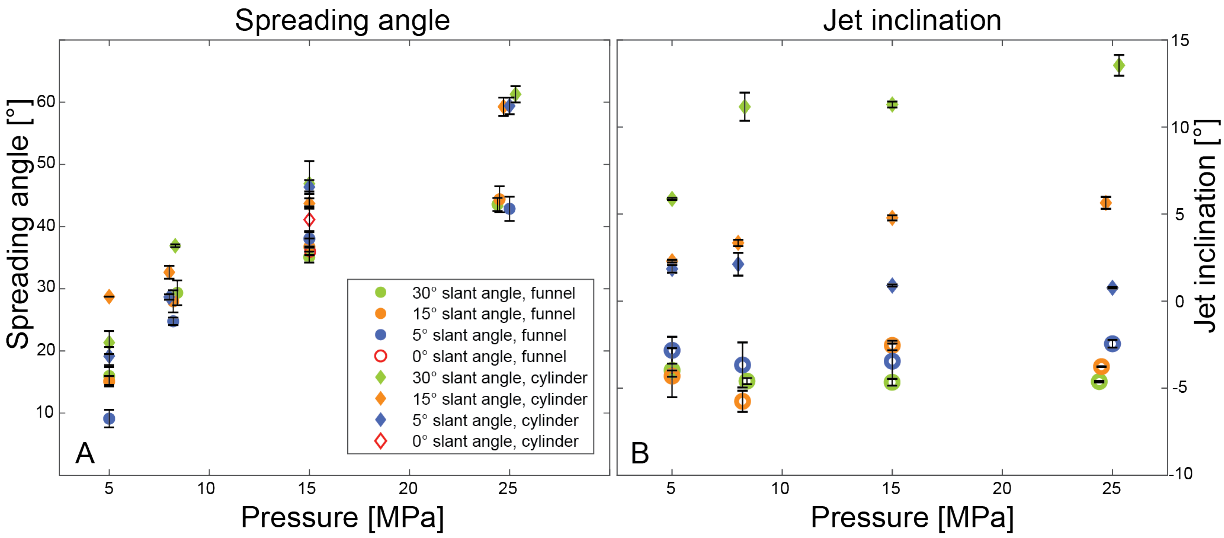

Figure 3.6: Gas jet spreading angle (A) and jet inclination (B) plotted against reservoir pressure. Initial pressure of 5, 8, 15 and 25 MPa. Circular symbols represent experiments with the 15° diverging vents and diamond symbols for cylindrical vents. The colours represent slant angle. Data for experiments with 0° slant angle taken from Cigala et al. (2017). (A) The spreading angle is highly affected by the initial reservoir pressure. Furthermore, higher slant angles of the exit plane produce bigger spreading angles. (B) The slant angle exerts the biggest control on jet inclination in experiments with the cylindrical geometry, while the initial reservoir pressure has no strong influence, except for the pressure increase between 5 and 8 MPa. For experiments with the diverging inner geometry the jet inclination is around 5° against the dip direction of the exit. There seems to be no clear relationship between pressure ratio and/or slant and the degree of jet inclination.

3.4.2 Jet inclination

The emitted jet reacted to the slanted exit plane by deviating from the vertical centre streamline. We observed opposing effects of inner geometry on jet inclination direction: for cylindrical vents, jets were generally inclined in the dip direction of the vent surface (positive angles), whereas funnel vents showed the opposite trend (against the dip direction, negative angle, Figure 3.6). For the case of vents with the cylindrical inner geometry, the strongest effect on jet inclination was exerted by the slant angle of the exit plane, followed by the pressure ratio. Overall, the maximum jet inclination was between 1° (for 5° slant and 5 MPa) and 13° (for 30° slant and 25 MPa). Jets emitted from vents with diverging geometry were generally less affected by slant angle or pressure ratio and their inclinations were between 2° and 7° for all cases. The smaller reservoir volume in setup 3 had no significant impact on jet inclination.

3.5 Discussion

Volcanic explosions are the visible expression of a complex interplay of several source and path processes, several of which are likely to be highly variable with time. The crater may have an irregular shape. The vent may be open or clogged. Magma inside the conduit can exhibit strong textural gradients. The conduit may be vertical or inclined. Many of those parameters will be discussed in the following. Many studies have investigated the overall characteristics of eruption plumes. Here we described the near-vent characteristics of gas jets in the gas-thrust region where the observed features are due to magmatic processes and air entrainment makes little or no contribution.

3.5.1 Experiments

For each experiment, time zero is set at the visible onset of gas ejection from the main reservoir to account for subtle differences in diaphragm behaviour. The visibility of the gas is due to condensation upon expansion-driven cooling. After diaphragm rupture, the gas is expanding vertically and the flow requires some time to develop and generate quasi-static conditions for a short moment (Peña Fernández et al., 2020). As long as the jet is underexpanded at the vent (i.e. the gas pressure is above ambient pressure), the jet will expand horizontally. This study determined the maximum gas spreading angle as well as the jet inclination.

Two controlling factors with influence on gas expansion dynamics were found: shallow subsurface geometry (inner geometry) and topography (slant angle, Figure 3.3). The systematically larger spreading angle in experiments with cylindrical inner geometry is linked to higher pressure at the vent exit. Above the vent exit, gas can decompress radially. In experiments with diverging vents, radial gas expansion started inside the vent at the beginning of the diverging section (30 mm below the vent exit), resulting in systematically lower vent pressure. Similarly, the difference between the maximum spreading angle between lower and upper vent exit is also related to the vent exit pressure as the geometry affects the vertical difference between the two sides (Figure 3.3). In case of the cylindrical geometry, the maximum height difference between lower and upper vent exit is 16 mm (30° slant angle) but nearly twice as high (30 mm) for the diverging geometry. In summary, the dynamics in the gas-thrust region for volcanic eruptions, as well as our experiments, are strongly controlled by the ratio of exit area to critical area. Comparison with maximum gas spreading angles determined by Cigala (2017) for gas-particle jets shows similarity with gas spreading angles measured on the lower vent side (see Figure 3.6A), but only for experiments where the onset of particle ejection (depending on particle to exit distance) starts after the maximum gas spreading angle has developed. Afterwards, the presence of particles at the vent exit alters flow conditions significantly. Adding particles to future experiments with slanted geometry will provide the opportunity for a thorough comparison on the effect of complex vent geometry on gas-particle ejection.

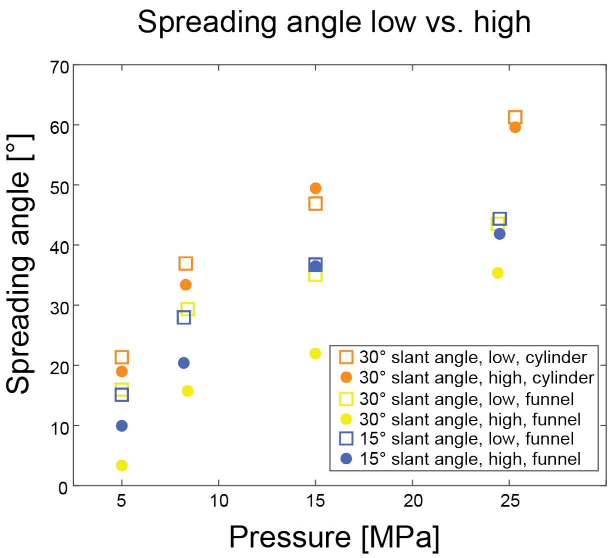

Figure 3.7: Maximum gas spreading angles on low and high vent exit side plotted against the reservoir pressure. Initial reservoir pressure of 5, 8, 15 and 25 MPa. Square symbols represent spreading angles on the lower vent exit side, circular symbols for spreading angles on the upper vent exit side. Orange symbols represent experiments with cylindrical geometry and 30° slant, yellow symbols diverging geometry with 30° slant angle and blue symbols for diverging geometry with 15° slant angle.

The jets from our vertical experiments were visibly inclined, showing a first order influence of crater geometry on the gas-thrust region. In Figure 3.6B the jet inclination of experiments with cylindrical inner geometry and 5° slant angle appears to decrease with increasing pressure. However, the variation of inclination angles for the cyl05 is small and can be attributed to instabilities in the boundary layer that have a larger impact when the inclination angle is small. We observed the same two types of jet inclination behaviour as have been previously described numerically for sustained jets by Lagmay et al. (1999). The high spatial and temporal resolution in our experiments with starting jets also reveal processes that have not been addressed before. Due to the dynamic nature of our experiments we could observe the continuous transition caused by the depletion of the finite gas reservoir, involving variable degrees of jet underexpansion and supersonic flow conditions (Figure 3.5). Overall, we observed jet inclination towards the lower vent side for cylindrical geometry and towards the upper vent side for diverging geometry, but already during underexpanded flow conditions. The two geometries show different inclination behaviour with time and starting overpressure. For cylindrical geometry, inclination was observed highest after 4.3 ms and was positively correlated with starting pressure and slant angle. For diverging geometry, the inclination increased with decreasing pressure but showed a clear asymmetry early on (e.g. Figure 3.5, yellow outline, t = 4.3 ms). Flow instabilities towards the end of the visible gas flow overprint the jet inclination. In essence, vent geometry has been shown to cause asymmetry of the impulsive gas jets as it impacts gas expansion and air entrainment. Gas flow velocity and density changes due to entrainment affect plume buoyancy and ballistic pathways and should be included in hazard assessment of primary volcanic risks.

3.5.2 Volcanological implications

Volcanic eruptions are complex processes that have remained incompletely deciphered. Many boundary conditions cannot be measured directly and have to be measured remotely or estimated through model or experiments. Our scaled experiments revealed that the surface manifestation of a volcanic explosion can show directionality, even with a vertical and symmetrical subsurface geometry. In this simplified case the direction of the jet is solely dependent on vent geometry and vent exit pressure. In nature, the dependencies are certainly more complex but assuming a vertical conduit and knowing the geometry of the vent we might be able to make assumptions about the exit pressure based on observations of the emitted jets.

Asymmetrical gas-particle jets and eruption plumes have been described for large, pyroclastic density current issuing eruptions (Cole et al., 2015; Lagmay et al., 1999; Major et al., 2013). Inclined jets have also been observed for less energetic eruptions for example, at Stromboli volcano, Italy, where inclination of the shallow plumbing system beneath the active craters in February 2004 was proposed by Zanon et al. (2009). Nine out of twenty observed jets exhibited a dip of around 7–13° towards the northwest regardless of wind direction. They stated that the inclined jets could be generated by a combination of deep-seated slug bursts within an inclined conduit. However, it was also reported that the morphology of the Northeast Crater was characterized by a deep and wide opening in the north-western crater wall at the time of the survey (Zanon et al., 2009). This kind of crater asymmetry is equivalent to those reported by Lagmay et al. (1999) and might deserve some consideration in accounting for the jet inclination for supersonic jets at Stromboli volcano. In fact, the idea of an inclined shallow feeder system at Stromboli volcano was previously proposed (Chouet et al., 2003) but the behaviour we observed in experiments with diverging geometry could account for vertical jets even with an inclined conduit. James et al. (2004) have described the influence of cylindrical conduit inclination on gas bubble ascent processes, leading to varying overpressure conditions at bubble burst and acentric rupture of the liquid film. When applied to higher viscosity magma, inclined conduits may ease a mechanical separation of gas bubbles and melt and enhance ascent velocity. There have been cases where an explosion destroyed parts of a symmetrical cone resulting in an immediate change from vertical jets to inclined jets (Schmid et al., 2021). In such cases, it is unlikely that the conduit geometry changed over such a short timescale and hence, vent asymmetry must be the factor governing the directionality.

The coupling of juvenile tephra to the (initially) surrounding gas jet is dependent on size and density (Taddeucci et al., 2017). Upon ejection into the atmosphere, the trajectory may be independent but the starting acceleration with a certain directionality is surely affected by vent geometry, making it a first-order parameter to consider for hazard assessment. An asymmetric vent with a variable exit height, allows flatter trajectories and therefore a higher range of ballistics on sides with a lower vent exit height. The areas that can be affected by impacts of ballistics is thus skewed towards the lower side of the vent given a shallow explosion source. The difference in jet spreading angle on different sides of asymmetric volcanic vents could lead to a variance of entrainment efficiency. Hence, the likelihood of a column collapse towards the side with the smaller jet surface area (smaller spreading angle) might be elevated. The effect of inclined jets on pyroclast dispersal, as already observed (Cole et al., 2015; Lagmay et al., 1999; Major et al., 2013), adds another controlling force on the distribution of proximal hazards of explosive volcanic eruptions. Jet inclination seems to be exclusively governed by the pressure at the vent exit and the vent geometry. The latter (and its temporal variations) can be achieved today with a high resolution. Quantifying the vent exit pressure is less straightforward. It requires assumptions on pressure radiation in complex topography (Lacanna and Ripepe, 2020) or near-exit measurements (Kueppers et al., 2019). Future measurements of gas dynamics in the near-vent gas-thrust region of volcanic explosions shall contribute to refined vent exit conditions. Some crucial parameters of volcanic vents affecting jet and plume behaviour can be constrained rapidly, reliably and with a high time resolution. Coupled with general knowledge from larger-scale observations of buoyant plumes and ballistic distribution, this will hopefully lead to enhanced hazard assessment as topographic variations may *a priori* allow to constrain size and location of areas of elevated risk.

3.6 Concluding remarks

In summary, the morphology of volcanic vents and the overpressure affect the gas dynamics in the near-vent part of the gas thrust region. Experiments with impulsive gas jets released from a vertical, cylindrical reservoir revealed the following positive correlations: The *pressure ratio* correlates positively with 1) the maximum spreading angle of the gas jet, 2) the maximum jet inclination for cylindrical vents, and 3) the duration of underexpanded character of the jet. The *slant angle* correlates positively with 1) the maximum spreading angle of the gas jet and 2) the maximum jet inclination for cylindrical vents. Moreover, the *inner vent geometry* influenced the direction of the jet inclination in two distinct ways, 1) towards the direction of the exit plane dip for cylindrical vents and 2) against the direction of the exit plane dip for diverging vents. Additionally, cylindrical vents produced larger spreading angles then diverging vents. The *reservoir volume* showed positive correlation with maximum gas spreading angle but no significant impact on maximum jet inclination.

We demonstrate here that inner and outer vent and/or crater geometry can lead to inclined jets and asymmetrical jet spreading angles. Even though this is not commonly reported for volcanic eruptions, there are examples where crater asymmetry led to asymmetrical behaviour in the gas-thrust region and consequently in the areas affected by the eruption (Cole et al., 2015; Lagmay et al., 1999; Major et al., 2013).

Today asymmetry of the vent and/or crater area can easily be detected and characterized by drone observations. Structure from motion photogrammetry allows the acquisition of data with unprecedented detail to analyse geometry, elevation, position and volumetric changes and their temporal evolution. Since this data collection is fast, easy, cheap and safe, even in times of volcanic unrest or ideally as part of a standard monitoring routine, asymmetry should not be neglected as factor influencing the proximal hazards of explosive volcanic eruptions.

Chapter 4

Complex vent geometry and asymmetric particle ejection: experimental insights

4.1 Abstract

Explosive volcanic eruptions eject a gas-particle mixture into the atmosphere. The characteristics of this mixture in the near-vent region are a direct consequence of the underlying boundary conditions. Yet it is not possible to observe directly the sub-surface parameters that drive such eruptions. Here, we use scaled shock-tube experiments mimicking volcanic explosions in order to elucidate the effects of a number of boundary conditions. As volcanic vents can be expected to possess an irregular geometry we utilise three vent designs, two "complex" vents and a vent with a "real" volcanic geometry. Particle size and density as well as experimental pressure are varied. The near-vent dynamics, characterised as a function of particle spreading angle and particle ejection velocity reveal a strong influence of the vent geometry, which governs both the direction and the magnitude of particle spreading and the velocity of particles. Spreading angle and velocity are negatively correlated with particle size and density and positively correlated with experimental pressure. These findings have implications for the distribution of volcanic ejecta and resulting areas at risk.

4.2 Introduction

Explosive volcanic eruptions eject gas and pyroclasts at high velocity and temperature into the atmosphere. The related threat to life and infrastructure is a consequence of the eruption's style and magnitude. In proximal areas (tens of metres to few kilometres), volcanic ballistics can inflict injury and destruction of property (e.g., Alatorre-Ibargüengoitia et al., 2016; Blong, 2013; Williams et al., 2017). Pyroclastic density currents (PDCs) pose an additional risk threatening thousands of lives, agricultural land and farm stock, as well as infrastructure (e.g., Blong, 2013; Charbonnier et al., 2013; Druitt, 1998). Therefore, identifying precursory signals to forecast volcanic eruptions or mitigate their impact is one of the main goals of volcanology.

In recent years significant advances have been made in monitoring and forecasting of volcanic eruptions (e.g., Dempsey et al., 2020; Johnson et al., 2018; Layana et al., 2020). Yet unforeseen or larger-than-expected eruptions still claim many human lives. Whilst it would be the safest option to draw large exclusion zones around (potentially) active volcanoes, this is often not socially feasible. In the absence of such measures, achieving a better understanding of source conditions and the related tipping point that will inevitably lead to an explosive event will be central to estimating the maximum travel distance of volcanic bombs and the development of probabilistic hazard maps. Here, we perform rapid decompression experiments and empirically correlate the ejection characteristics of gas-particle jets in the near-vent region with complex vent geometry in an effort to help satisfy these scientific goals.

In the near-vent region, volcanic explosions are typically manifested by multiphase underexpanded starting jets (Carcano et al., 2014; Kieffer and Sturtevant, 1984; Woods and Bower, 1995). In nature and in laboratory experiments, vent geometry exerts a prime control on the ejection of gas and gas-particle flows by affecting ejection velocity (e.g., Cigala et al., 2017; Kieffer, 1989; Valentine et al., 2012a; Wilson et al., 1980; Wilson and Head, 1981), jet radius (e.g., Jessop et al., 2016; Koyaguchi et al., 2010; Woods and Bower, 1995), jet inclination (Schmid et al., 2020) and gas and gas-particle spreading (Cigala et al., 2021). Further, vent geometry influences the trajectories of volcanic ballistics (Dürig et al., 2015) and the likelihood of column collapse (Jessop et al., 2016). Whether an eruption column collapses or rises as a buoyant plume is governed by the efficiency of entrainment of ambient air (Woods, 2010). Factors promoting a buoyant plume over collapse are narrow vents, high exit velocities, high gas content and possibly high pressure ratios at the vent (Valentine, 1997). The effect of vent shape on flow dynamics has been investigated for vents with radial or axial symmetry (e.g., Deo et al., 2007; Glaze et al., 2011; Jessop et al., 2016; Mi et al., 2000). To date, the natural complexity of volcanic vents is often greatly simplified in experiments and models, where the vent is commonly treated as a symmetrical circular feature. In reality, volcanic vents are likely complex, highly asymmetric shapes that can potentially change on short timescales and for volcanic eruptions, preferential emplacement directions of PDCs have indeed been explained by the asymmetry of vents and/or craters (Cole et al., 2015; Lagmay et al., 1999; Major et al., 2013).

The near-vent characteristics of volcanic jets are important for our quantitative understanding of volcanic eruptions since they are the first observable manifestation of the related sub-surface processes. Jet attributes directly above the vent derive from the underlying boundary conditions and vent geometry, while subsequently, atmospheric conditions (wind field, temperature, humidity) can substantially alter the jet dynamics. Additionally, the characteristics of the initial gas-particle jet significantly affect the further development of the eruption plume (buoyant vs (partial) collapse, plume height and pyroclast dispersal).

Multiphase jets result from magma fragmentation following deformation and gas expansion and occurs over a wide range of eruption styles, e.g., Strombolian, Vulcanian and Plinian eruptions (Gouhier and Donnadieu, 2011; Koyaguchi and Woods, 1996; Scharff et al., 2015; Taddeucci et al., 2012). Thus, in general, the complex interactions between the ejected phases and their characteristics (e.g., gas-particle ratio) exert strong controls on the dynamics of the jets. Two-way and four-way coupling interdependencies between the fluid phase (gas and melt) and solid particles have been reported (e.g., Bercovici and Michaut, 2010; Burgisser et al., 2005; Carcano et al., 2014; Cerminara et al., 2016). The degree of coupling between the solid and the gas phases significantly affects particle acceleration and resulting trajectories.

Magma fragmentation and volcanic jet generation have been successfully mimicked in shock-tube experiments (e.g., Alidibirov and Dingwell, 1996a; Arciniega-Ceballos et al., 2015; Cigala et al., 2017; Kueppers et al., 2006a; Montanaro et al., 2016) and such scaled laboratory experiments are a key to exposing boundary conditions of volcanic eruptions that are beyond direct observation. Cigala et al. (2017) empirically correlated the temporal evolution of particle exit velocity from radially symmetric vents with internal vent geometry, particle load, grain size distribution, conduit length and temperature. High-speed video footage of these experiments was used to analyse the temporal evolution of the angular deviation of particles from the vertical (Cigala et al., 2021). Based on the two vent geometries of Cigala et al. (2017) (cylindrical and 15° diverging inner geometry), we increased the complexity of vent geometry by introducing variably slanted surface planes (5°, 15°, 30°) to investigate the gas ejection from six axisymmetric vent geometries (cyl05, cyl15, cyl30, fun05, fun15, fun30; Figure B.1) at four starting pressure ratios revealing asymmetric spreading angles and inclined gas jets (Schmid et al., 2020).

Whereas in nature, gas-particle ejection and jet inclination might be influenced by inclined conduits (Zanon et al., 2009), debris coverage (Capponi et al., 2016), variable explosion depth (Dürig et al., 2015; Salvatore et al., 2018), pre-existing craters (Graettinger et al., 2015b; Taddeucci et al., 2013b) or an inhomogeneous high-viscosity layer (Kelfoun et al., 2020), in this study, we can exclude all of these factors and investigate the sole effect of subsurface boundary conditions (pressure, fragmentation efficiency and density) and vent geometry.
We performed repeatable shock-tube experiments (Figure 4.1) with three vent geometries (cyl30, fun30, S1, see Figure 4.2 and Figure B.1), two types of particles (scoriaceous and

pumice), each with three particle size classes (0.125–0.25, 0.5–1, 1–2 mm) and two experimental pressures (8 and 15 MPa) to further elucidate the effect of vent geometry and gas-particle coupling on the ejection of a gas-particle mixture.

4.3 Materials and Methods

4.3.1 Experimental setup

The shock-tube setup used in this study is an evolved version of the "fragmentation bomb" developed by Alidibirov and Dingwell (1996a) that has been adapted and utilised in many studies to date (Arciniega-Ceballos et al., 2015; Cigala et al., 2017; Kueppers et al., 2006b,a; Montanaro et al., 2016; Spieler et al., 2004). Here, we used the latest version, including the modifications introduced by Cigala et al. (2017) and Cigala et al. (2021) (Figure 4.1).

The setup consists of a high- and low-pressure section, separated by diaphragms. Two copper diaphragms (each with a stability of ~4.6 MPa) or three iron diaphragms (each with a stability of ~6.1 MPa) were used for the incremental pressurisation to the final autoclave pressure of 8 and 15 MPa, respectively. The autoclave (Nimonic 105 alloy) has an internal diameter of 28 mm and a volume of 127.4 cm^3. Upon intended failure of the uppermost diaphragm, the diaphragm(s) below go outside their stability field, open, and pressure equilibration initiates. The associated rapid decompression of the autoclave allows the gas to expand. The associated gas flow accelerates the particles; the gas-particle mixture is ejected through a vent into the low-pressure section, a 3 m high stainless-steel tank at ambient conditions, sitting above a 35 cm high transparent Perspex cylinder.

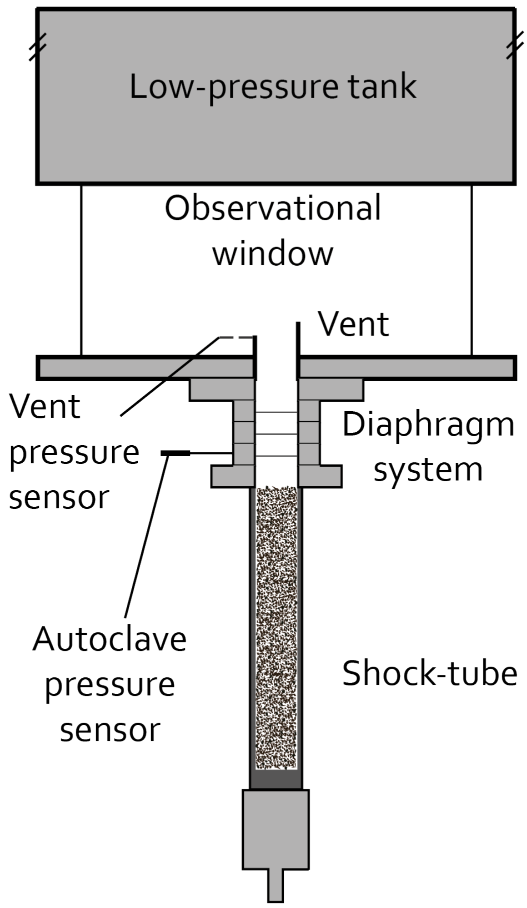

Figure 4.1: Shock-tube setup at LMU Munich with a high-pressure/temperature autoclave including samples, the diaphragm system and the low- pressure section above the vent.

Three different vent geometries were used in this study, increasing "topographic complexity" based on the findings of Cigala et al. (2017) and Schmid et al. (2020). At the base, all are the geometrical extension of the underlying autoclave (inner diameter of 28 mm). Two vent geometries were fabricated from 1.4305 NiCr steel and are non-erodible. They have already been used by Schmid et al. (2020), where they showed the biggest impact on gas-jet dynamics. They have a bilateral symmetry as they have a slanted top plane (30° inclination) above a cylindrical (cyl30) or 15° diverging funnel (fun30) inner geometry, respectively. The lower vent exit height was always 50 mm (Figure 4.2). The top exit of those vents was 16 and 30 mm higher, respectively. The third non-erodible vent (S1) resembles the geometry of the active S1 vent on Stromboli in May 2019.

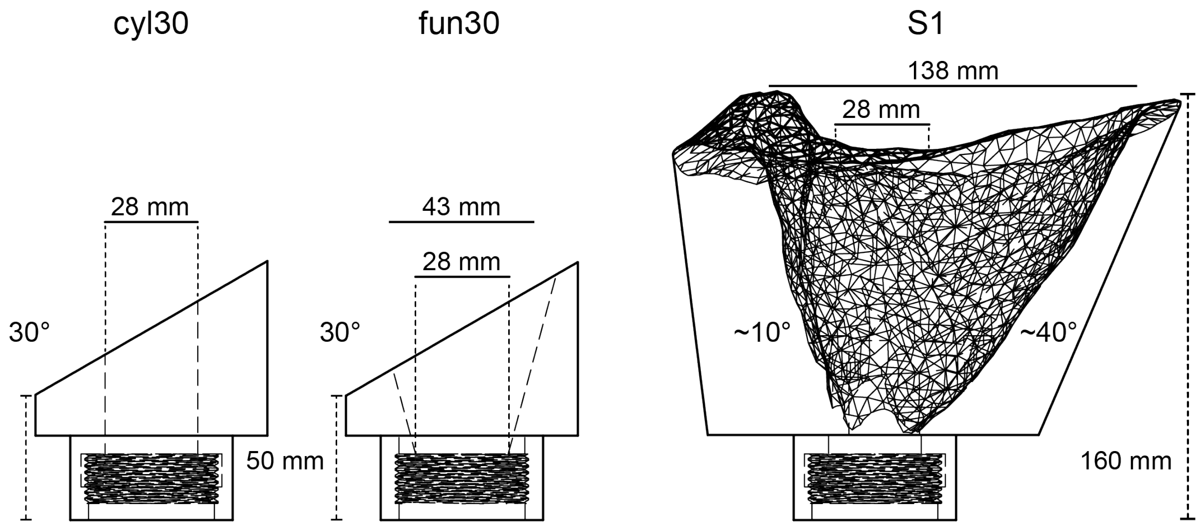

Figure 4.2: Sketch of the three vent geometries used for the present study. They can be distinguished by their characteristic geometry element with a slanted exit plane (cyl30 and fun 30) and a variable divergence angle (S1). The internal diameter at the bottom of the vent is 28 mm for all geometries while the horizontally projected exit diameter is 28, 43 and 138 mm.

During a field campaign, aerial imagery was collected by unoccupied aerial vehicle (UAV) of this vent and subsequently, a 3D model was created by Structure from Motion (SfM) photogrammetry using *Agisoft Metashape*. For a detailed description of the field campaign and the processing, refer to Schmid et al. (2021). The created 3D mesh was transformed into a printable body with *Autodesk Fusion 360*. Afterwards, the outer shape of the vent was designed and exported as Standard Triangle Language (STL) file, a standard file format used in 3D printing. The software *Slic3r* was used to convert the STL file into printing instructions (G-code) for the 3D printer by cutting the model into horizontal slices (layers) and the required toolpaths to form the 3D printed model. A *Renkforce RF1000* 3D printer that was controlled by the Repetier-Host software was used. The model was printed with polylactic acid (PLA) filament with a 0.5 mm nozzle, a layer thickness of 0.4 mm and 60% infill density in a honeycomb structure. The printed vent was fixed to a steel vent mount to withstand the applied experimental conditions resulting in a total height of ~160 mm. The inner diameter up to the throat of the vent is 28 mm as in the other vents (Figure 4.2). The average diameter at the vent exit is 138 mm compared to 28 mm (cyl30) and 43 mm (fun30). The defining geometry element of the S1 vent was the asymmetric divergence with ~10° on one side and ~40° on the opposing side.

Two pressure steps (8 and 15 MPa) and six different samples were tested for each vent geometry. We used two types of natural samples from the East Eifel volcanic region (Germany): scoriaceous fragments of a porous lava flow (SL) and pumice particles from the Laacher See eruption (LSB). Three particle sizes were used for both types: 1) fine, 0.125–0.25 mm; 2) medium, 0.5–1 mm; and 3) coarse, 1–2 mm. The average density was 2.5 g/cm^3 and 1.4 g/cm^3 for the scoria (SL) and the pumice (LSB), respectively (Douillet et al., 2014). The particle load for all experiments was between 38 g (LSB 1–2 mm) and 175 g (SL 0.125–0.25 mm) (Table 4.1). All experiments were conducted at ambient temperature (~25° C) with argon as pressurising gas.

Table 4.1: Average sample load for all particle types and particle size fractions. The particle vent ratio is calculated by dividing the medium particle size of each particle size fraction by the basal vent diameter (28 mm).

Particle [mm]	Sample load [g]	particle/ conduit ratio
SL		
0.125–0.25	175	0.007
0.5–1	152	0.027
1–2	143	0.054
LSB		
0.125–0.25	54	0.007
0.5–1	44	0.027
1–2	38	0.054

Once the experiments were initiated, the instantaneous pressure drop in the autoclave (> 1 GPa/s, Spieler et al. (2004)) was recorded by a static pressure sensor (KISTLER 4075A500) at the top of the autoclave to trigger the recording system. We recorded the experiments with a high-speed camera (Phantom V711) and a pressure sensor (KISTLER 601A) at the vent exit. All experiments were filmed at 10,000 frames per second (fps) and a resolution of 1280×600 pixels (cyl30 and fun 30), 864×760 pixels (S1, 15 MPa) or 960×704 pixels (S1, 8 MPa). The camera was aligned orthogonally to the symmetry plane of the vent and centred on the vent axis.

We exported scaled single frames to manually and optically analyse them with the *ImageJ's* plugin *MTrackJ*. We measured the particle spreading angle of the gas-particle jets and the particle ejection velocity. The spreading angles reported here are always the maximum spreading angle that was reached during a single experiment. The particle spreading angle is the angular outward deviation from the vertical continuation of the inner autoclave walls. It was measured as a tangent along the edge of the gas-particle jet starting at the vent exit to the upper limit of the field of view. All angles reported below represent averaged values from three repeated measurements. For a qualitative comparison of the temporal evolution of the gas-particle jets and the asymmetry of the particle spreading angle the jet boundary (as defined by the presence of particles) was traced for each experimental condition and subsequently stacked (Figure 4.3). The particle velocity is measured between 1 and 2 ms after the first particle ejection (t_0). Each particle was tracked over five still frames, and the average velocity is given for > 25 particles.

The reproducibility of experiments in this experimental setup has been demonstrated in several studies (e.g., Alatorre-Ibargüengoitia et al., 2011; Cigala et al., 2017; Kueppers et al., 2006a). The heterogeneity of natural samples has a big influence on the fragmentation behaviour of the sample. In the present study, loose particles were used that were accelerated with negligible preceding fragmentation. We repeated selected experiments to test reproducibility and experiments influenced by irregularities in the experimental procedure (e.g., imperfect opening of the diaphragms). The reproducibility of gas and gas-particle jet spreading angles was demonstrated by Cigala et al. (2021) and Schmid et al. (2020). The subjective error by optically and manually measuring the spreading angles was quantified by letting three individuals analyse the same experiment and comparing the results (Cigala et al., 2021). Since the measuring methodology in the present study is the same, and the same experimental setup was used we assume negligible operator subjectivity as well. We tested the reproducibility of particle ejection velocity by repeating individual experimental conditions three times and analysed each experimental run three times each (min. 25 representative particles in each experiment). We found that the variance in particle ejection velocity within each experiment is higher than the variance between the repetition experiments (Figure B.2). The standard deviations of three measurements (25 particles each) of the same experiment were up to 17 m/s. In contrast, comparing the average velocity of the three experiments with identical starting conditions had a 5 m/s standard deviation.

4.3.2 Scaling

For the experiments presented here, the same non-dimensional scaling was applied as for the experiments of Cigala et al. (2017) and Schmid et al. (2020). This manner of scaling has been proven suitable for rapid decompression experiments (e.g., Dellino et al., 2014; Dioguardi et al., 2013) because two explosions at vastly different scales, e.g. in nature and the laboratory, are equivalent if all non-dimensional parameters match. Effectively, it is unlikely to have full similarity in all parameters at the same time. Therefore, it is crucial that the dynamics of the explosions are at least comparable when analysing the differences between nature and laboratory.

We calculated Reynolds number (Re), Mach number (M) and the Stokes number (St) to describe the fluid flow dynamics and the coupling between gas and particles. The reference quantities of Re and M were calculated following the one-dimensional isentropic theory (Oswatitsch, 1952) by estimating gas density, viscosity and flow velocity based on

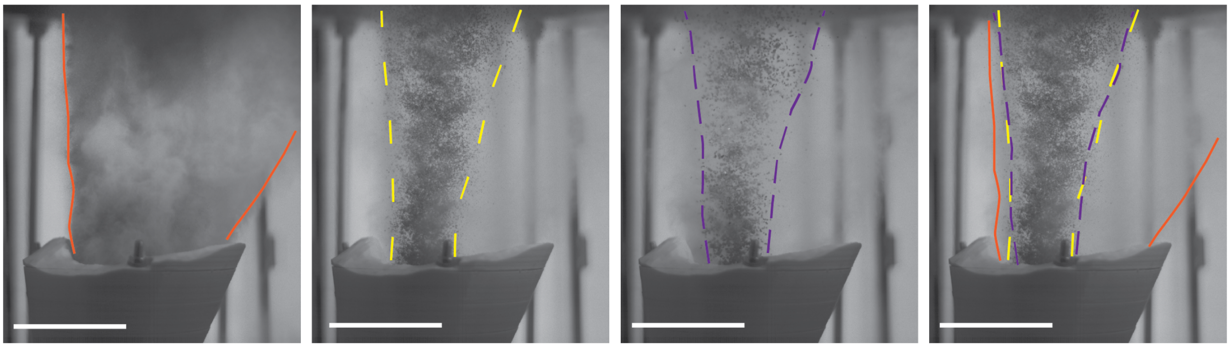

Figure 4.3: For a qualitative comparison of the various experimental conditions the outlines of the jets were manually traced in scaled single frames at a fixed time after the first gas became visible (t_0). The underlying image for the stacked version is always the single frame of the 0.5–1 mm experiment. All images for the complete experimental suite displayed in Figure 4.5 were produced in this manner. Here shown for experiments performed with vent geometry S1, SL particles, room temperature and 15 MPa starting pressure. The scale bar shows 10 cm. The same colour coding of the contours was used in Figure 4.5 and B.3

the starting experimental conditions. We stress that the experiments performed here are highly dynamic, and the values listed in the following are maximum values (Table 4.2). Schmid et al. (2020) calculated Re for these experiments at characteristic flow conditions, e.g., at the throat of the vent, at the vent exit and fully expanded flow conditions above the vent. For the cyl30 vent Re was between 3.58×10^7 (8 MPa, throat) and 2.21×10^8 (15 MPa, fully expanded), and for the fun30 vent was between 3.58×10^7 (8 MPa, throat) and 3.40×10^8 (15 MPa, fully expanded). Re for the S1 vent was calculated at 1.90×10^7 (8 MPa, throat) and 1.09×10^8 (15 MPa, fully expanded). In volcanic eruptions, Re can be between 10^5 and 10^8 (Clarke, 2013) or as high as 10^{11} (Kieffer and Sturtevant, 1984), 1984]. M is the dimensionless quantity for the ratio between fluid velocity and the speed of sound of the surrounding media. It was calculated by following Saad (1985) to be 1.6 for the cyl30 vent and 3.2 or 3.5 for the fun30 vent at 8 MPa and 15 MPa, respectively (Schmid et al., 2020). The S1 vent with an exit diameter of 138 mm has a M of 10.47 (8 MPa) and 14.31 (15 MPa). Volcanic jets frequently exhibit $M > 1$ if the reservoir pressure is more than about twice the atmospheric pressure (Kieffer and Sturtevant, 1984).

The Stokes number is the particle's momentum response in relation to the surrounding flow field, i.e., it describes how well a particle couples to the flow. We calculated St for fully expanded conditions for experiments with 0.5–1 mm and 1–2 mm (of SL and LSB) particles following Carcano et al. (2014). The maximum velocity of gas and particles is required as an input to calculate St. While it was possible to measure the particle velocity for experiments with 0.5–1 mm and 1–2 mm particles, it was not possible to determine the velocity of individual particles in experiments with 0.125–0.25 mm particles. In addition, it was not possible to determine reliable gas-velocity in this experimental setup (Cigala et al., 2017), and we had to revert to theoretical values following one-dimensional isentropic theory (Saad, 1985; Woods and Bower, 1995).For the range of particle size (0.5–1 mm and 1–2 mm), particle densities, ejection velocities, and vent diameters used in the present study, St was between 45 (scoria, 1–2 mm) and 2 (pumice, 0.5–1 mm). Theoretical investigations suggested that particles with a $St > 1$ are not coupled to the carrier gas-phase (Carcano et al., 2013, 2014; Woods and Bower, 1995). The experiments with 0.125–0.25 mm should be better coupled to the gas-phase with a St closer to 1 (Cigala et al., 2017).

By using 3D printing to produce the S1 vent, we introduced surface roughness into the system. Based on the findings of Alsoufi and Elsayed (2017), we estimated the surface roughness for our vent to be between 0.045 and 0.071 mm. For fluid flows with high Re, the wall friction depends solely on the friction factor, a ratio of wall irregularity size to conduit size (Wilson et al., 1980). Here, the friction factor is 0.0016–0.0026 at the top of the conduit and 0.0005–0.0003 at the vent exit. Wilson et al. [1980] stated that the calculated range of friction factors for natural conduits varies for most cases between 0.005 and 0.02. Hence, we assume that the roughness related to the 3D printing process has minor influence compared with natural conduit roughness.
Given the broad range of particle sizes of pyroclasts emitted by volcanic eruptions and the similarity of Re, our experiments we suggest that our experiments reproduce well the dynamics of volcanic eruptions for gas-particle jets in different St regimes.

4.4 Results

4.4.1 Particle spreading angle in gas-particle jets

In experiments with identical conditions, the cyl30 vent showed a higher maximum particle spreading angle than the fun30 vent (Figure 4.4). This difference was especially pronounced on the left (lower) vent side. For all experimental runs, particle size had the biggest impact on jet spreading angle, where the fine particles consistently showed the largest particle spreading angle. In all cases, experiments with cyl30 and fun30 geometries exhibited an asymmetric jet spreading angle with a larger maximum spreading angle on the left (lower) vent side than on the right side.
The jet spreading angle measured for the S1 vent could not be directly compared with the cyl30 and fun30 vent geometries because of the difference in the vent exit height and the resulting offset in time. However, the spreading angle of the jet emitted through the S1 vent was also asymmetrical, with larger spreading angles on the right (more divergent) vent side than on the left side. The spreading angle measured at the steep side of the vent was small and seemed relatively unaffected by particle size, density or experimental pressure.

Table 4.2: Maximum non-dimensional numbers calculated for the cyl30, fun30 and S1 geometry at 8 and 15 MPa experimental pressure. Mach number (M) was calculated at the lower vent exit height (cyl30 and fun30) and for S1's average exit diameter. Reynolds number (Re) was calculated at the throat of the vent, the vent exit height (lower side for cyl30 and fun30) and fully expanded conditions. The characteristic length used to calculate these values is the vent exit diameter (28 mm for the cylindrical vent, 43 mm for diverging vents and 138 mm for S1). St was calculated for both sample types, each with a particle size of 0.5–1 mm and 1–2 mm.

Pressure [MPa]	M Exit	Re Throat	Re Exit	Re Fully expanded	St SL [mm]		St LSB [mm]	
cyl30					0.5-1	1-2	0.5-1	1-2
8	1.6	3.6E+07	4.8E+07	6.8E+07	26	45	20	35
15	1.6	6.7E+07	9.7E+07	2.2E+08	17	31	17	26
fun30								
8	3.2	3.6E+07	9.5E+07	1.0E+08	17	33	13	26
15	3.5	6.7E+07	2.5E+08	3.4E+08	12	22	8	17
S1								
8	10.5	1.9E+08	6.2E+08	3.3E+08	5	10	3	14
15	14.3	3.6E+08	3.6E+09	1.1E+09	3	6	2	9

In general, experimental pressure was positively correlated, and particle size and density were negatively correlated with gas-particle jet spreading angle. The vent geometry exerted the strongest control and governed the direction and degree of particle spreading angle asymmetry, manifested in visually inclined jets. The effect of particle size was strongest for the fine particle size fraction (Figure 4.3A, D). In contrast, the difference between medium and coarse particles was less distinctive and depended on vent geometry. Particle density visibly affected gas-particle jet dynamics causing larger spreading angles for LSB particles than for SL particles. The magnitude of this difference varied with particle size and pressure. All other experimental conditions constant, 15 MPa pressures were generally correlated with a larger particle spreading angle than 8 MPa pressure. The only exception was S1's left (less divergent) side, where the spreading angle was seemingly unaffected by changing boundary conditions. Figure 5 shows the temporal evolution of the gas-particle jets and the asymmetry of particle spreading angles as a function of particle size and vent geometry. All experiments exhibited the largest spreading angle at the beginning of the experiments. With proceeding decompression spreading angle decreased. Fine and light particles showed a larger spreading angle that could be maintained longer than for coarse and dense particles. In the beginning, 2.5 ms after the first gas ejection, the gas-particle jet emitted by the fun30 geometry was inclined towards the left (lower) vent side. At t= 5 ms, and later in the experiment, the jet was inclined towards the opposite side, the right (higher) vent side. In experiments with the S1 geometry, the particle spreading angle was sub-vertical on the left side of the vent for all experimental conditions and at all time steps. On the right (more diverging) side of the vent, larger spreading angles were observed than on the left vent side. The S1 geometry had a higher vent exit height than the other geometries, which caused a delayed ejection of SL particles visible at t = 2.5 ms, while LSB particles filled the entire field of view (Figure 4.5, top row). The delay was even more apparent in the 8 MPa experiments (see Figure B.3).

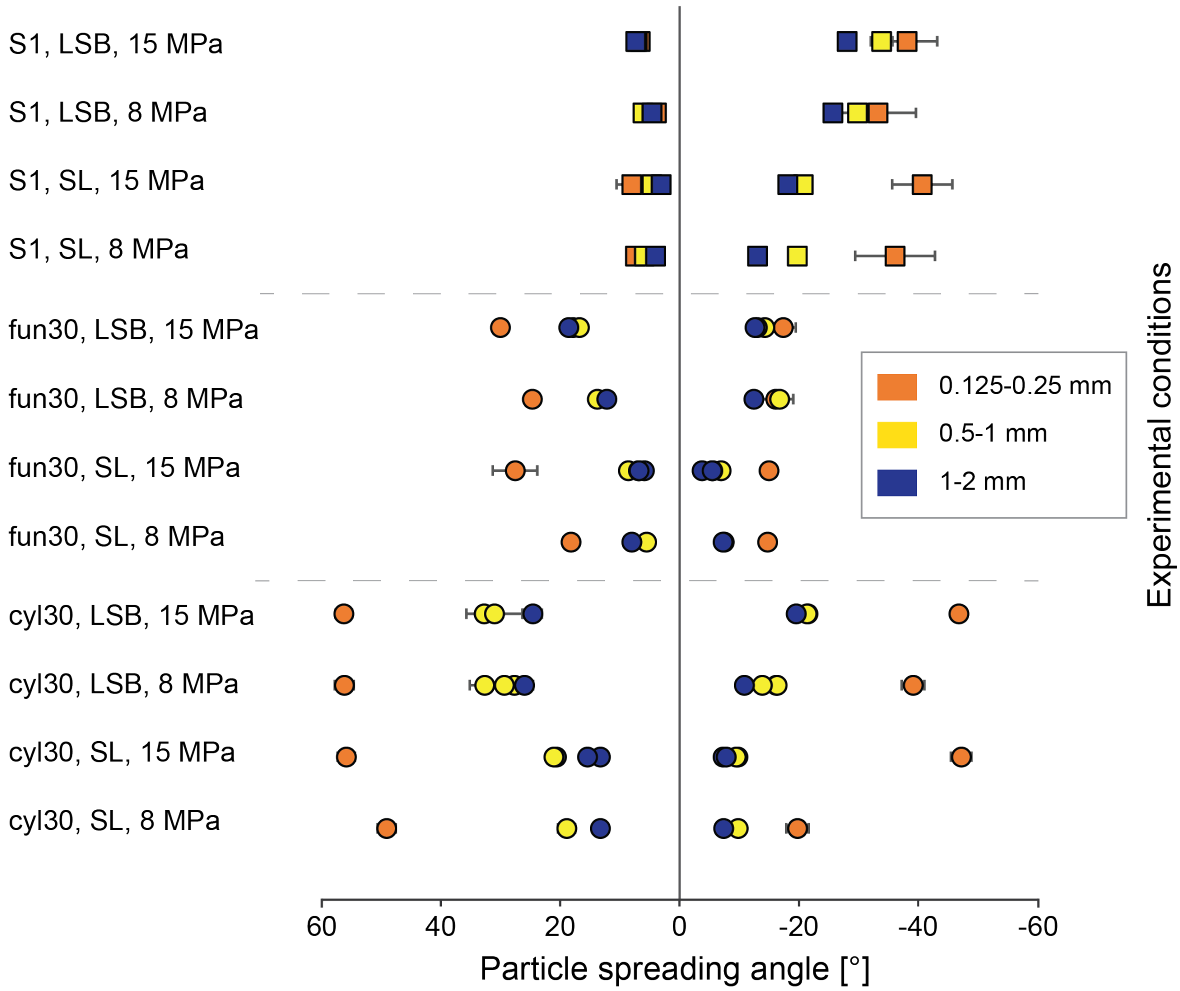

Figure 4.4: Particle spreading angles plotted for all experimental conditions. Positive values are spreading angles on the left side of the vent, negative values on the right side. Circular symbols represent experimental runs with the cyl30 and fun 30 geometry, square symbols for S1. The colours represent the particle sizes of 0.125–0.25 (orange), 0.5–1 (yellow) and 1–2 mm (blue). Error bars represent the standard deviation for the average of three repetitions of measurements. Error bars can be smaller than the associated symbol.

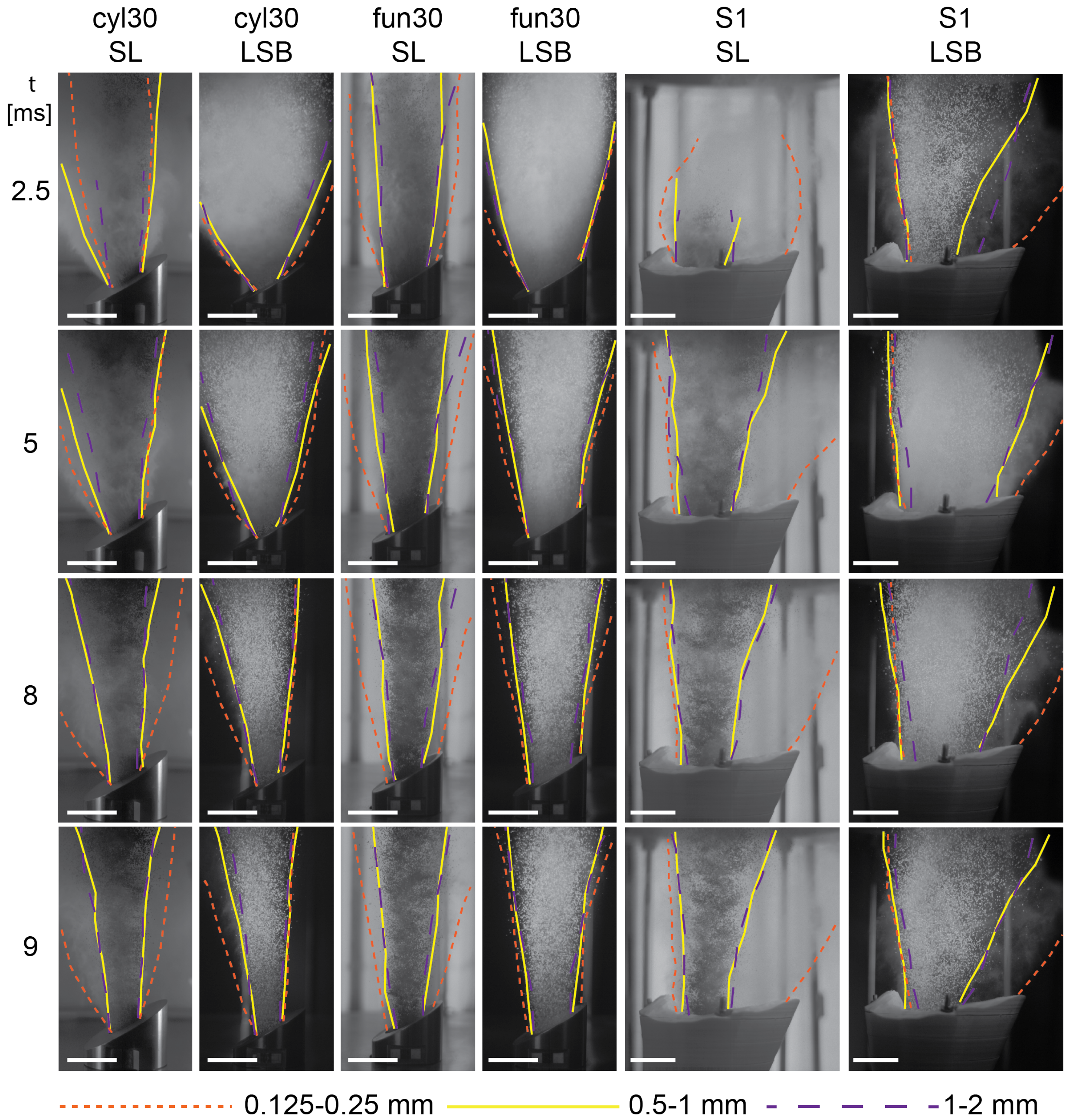

Figure 4.5: Time series of jet spreading angles at 15 MPa experimental pressure. Each vertical column shows the temporal evolution of particle ejection, with four rows at 2.5, 5, 8, and 9 ms after the onset of the gas ejection. The columns represent six different experimental conditions, using particles of two different densities (SL, LSB) and 3 different vent geometries (cyl30, fun30, S1). Colour lines (see Fig. 4.3 for explanation) mark the outlines of particle ejection. For every individual stack of images, the corresponding image from the experiment with 15 MPa and 0.5–1 mm particles were taken as basis. T_0 is defined as the onset of gas ejection and the scale bar shows 5 cm. This Figure was created as in Figure 4.3. Figure B.3 shows the series with 8 MPa experiments.

4.4.2 Particle ejection velocity

Differences in particle ejection velocity are a function of particle density, vent geometry, pressure and subordinately particle size. For the fine particles, it was not possible to obtain particle ejection velocity because of lack of resolution. Lower particle density (LSB) accounted for up to >100 m/s (>200 %) higher velocities than SL samples (Table 4.3). 15 MPa, Figure 4.6) starting pressure caused increased particle ejection velocity (up to ~ 50 m/s, ~ 25 %) compared to 8 MPa. Accordingly, the highest ejection velocities were observed at the beginning of particle ejection in LSB particles and 15 MPa overpressure experiments. Usually, the fun30 vent showed higher particle ejection velocities compared to both other vents (up to ~ 30 m/s).

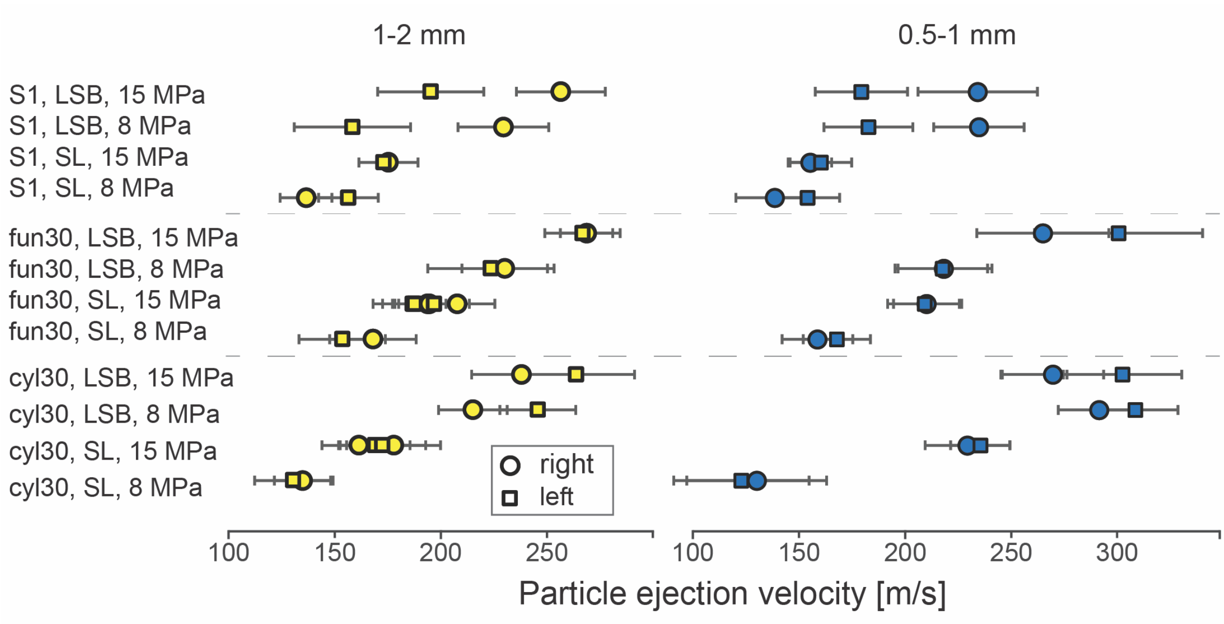

Figure 4.6: Particle ejection velocity plotted for all experiments with 0.5–1 and 1–2 mm particles. Dots mark velocities on the right-hand side (higher side of cyl30 and fun30 vents and more diverging side of S1) of the vent while squares mark velocities on the left side (lower side of cyl30 and fun30 vent and less diverging side of S1). Error bars represent the standard deviation of the averaged particle velocity.

Furthermore, vent geometry caused the asymmetric distribution of particle velocity, i.e. faster particles on one side of the vent. We observed up to ~ 60 m/s velocity difference in experiments with the S1 vent geometry and LSB particles. The higher velocity was measured on the right (more diverging) side of the vent. In experiments with the cyl30 and the fun30 geometry, LSB particles showed a higher velocity on the left (lower) side. In the case of the cyl30 vent at both 8 and 15 MPa pressure, the fun30 vent only at 15 MPa. In experiments with SL particles, no distinctive velocity distribution was observed (Figure 4.6). There was no clear correlation between particle size and ejection velocity with a tendency for higher velocities for finer particles. In general, particle velocity varied substantially, even within the same experiment and at the same ejection time.

Table 4.3: Particle ejection velocity for all experimental conditions. The velocity was always measured between 1 and 2 ms after the ejection of the first particles. On each side of the vent, 25 particles were measured and averaged (v_{left} and v_{right}). Positive values of Δ_v indicate higher velocities on the left vent side. All velocities are in m/s.

Experiment	0.5–1 mm			1–2 mm		
	v_{left}	v_{right}	Δ_v	v_{left}	v_{right}	Δ_v
cyl30						
SL, 8 MPa	131	124	7	135	131	4
SL, 15 MPa	230	236	-6	169	171	-1
LSB, 8 MPa	292	309	-17	215	246	-31
LSB, 15 MPa	270	303	-33	238	264	-26
fun30						
SL, 8 MPa	160	169	-9	168	154	14
SL, 15 MPa	211	210	1	199	190	8
LSB, 8 MPa	219	219	0	230	223	6
LSB, 15 MPa	266	301	-36	268	267	2
S1						
SL, 8 MPa	139	155	-16	136	156	-20
SL, 15 MPa	156	161	-5	175	173	2
LSB, 8 MPa	236	184	52	229	158	71
LSB, 15 MPa	235	180	55	256	195	61

4.5 Discussion

Gas-particle jets respond to the complex geometry by exhibiting asymmetric behaviour regarding jet spreading angle and particle velocity. Experimental vent geometry governed the general direction and behaviour of the gas-particle jets, while particle properties and overpressure controlled how well the particles followed the forcing (jet spreading and inclination) exerted by the vent geometry. Once decompression was initiated, the ensuing expansion led to a vertical gas flow within the autoclave. The related drag accelerated particles, thereby transferring a significant portion of the initially stored energy into kinetic energy. The geometric boundary conditions (conduit length or depth of magma surface and the topography of the volcanic edifice) controlled the velocity and residual overpressure of the gas phase at the transition into the atmosphere. If jets were underexpanded at the vent, the lateral expansion contributed to pressure equilibration with the atmosphere. The associated horizontal gas drag acted on all particles ejected from the experiment (or volcano).

4.5.1 Particle spreading angle in gas-particle jets

Vent geometry had the most striking effect on particle ejection dynamics as it caused the largest differences in the particle spreading angle and controlled the asymmetry of the particle jet. Experiments with the cyl30 geometry showed the strongest horizontal expansion and the highest calculated overpressure at the vent exit (Schmid et al., 2020). Because of the slanted top of the vent, the lateral expansion started first on the left (lower) side of the vent, while the lateral confinement still prevented expansion on the right (higher) side. As a result, the jet exhibited asymmetrical particle spreading angles with larger spreading on the vent's left (lower) side. In experiments with the fun30 vent, the initial gas expansion started inside the vent, thereby partially accommodating overpressure. Consequentially, the spreading angle was smaller than for the cylindrical geometry. Because of the slanted top, the spreading angle was also asymmetric, with a larger angle on the left (lower) side. As the pressure at the vent further decreased, the gas-particle jet changed its direction and exhibited a larger particle spreading angle on the right (higher) vent side after ~ 5 ms. This behaviour was unique for the fun30 geometry and linked to the more efficient decompression and lower vent exit pressure (Table B.1). A inclination of the jet towards the higher vent side was observed for gas jets (Schmid et al., 2020) and in numerical models (Lagmay et al., 1999), linked to the transition from underexpanded to overexpanded flow conditions. The S1 vent showed asymmetric particle spreading angles, although there was no difference in vent exit height. For all experiments with S1, particle trajectories on the left side seem to be a geometric extension of the inner vent wall. This likely indicates that gas overpressure had been accommodated before reaching the vent exit height. On the right side of the vent the strong divergence allowed lateral spreading of the particles as a result of a non-uniform gas expansion.

Both particle size and density influenced the degree of coupling between a particle and the surrounding expanding gas flow. Accordingly, the additional lateral expansion of the gas phase above the vent visibly manifested as particle spreading angle. Overall, particle size was negatively correlated with particle spreading angle, and the fine particles always exhibited the largest values. Owing to their lower bulk density, pumice particles were better coupled to the gas than the denser SL particles and generally showed larger spreading angles. This was especially pronounced for the medium and coarse samples. The fine particles of both samples showed similar behaviour showing that the drag of gas was similarly efficient in deflecting particles laterally.

4.5.2 Particle ejection velocity

The complex vents used in this study generated substantial variability in the velocity of particles tracked at two vent sides. The same variability was not observed in studies with symmetrical vent geometries (Cigala et al., 2017). Moreover, particle density was a major controlling parameter on ejection velocity (higher velocity for LSB than SL particles),

while particle size only had a minor impact on velocity. Still, the highest velocity values were measured for medium particles.
The difference in particle velocity on either side of the vent was a consequence of the complex vent geometries. In experiments with the cyl30 and fun30 geometry we measured a higher particle velocity on the left (lower) than on the opposing side (Table 4.3). This was only visible for the LSB particles since they were coupled sufficiently to still be affected by the unconfined gas flow. As the fun30 vent decompressed more efficiently, the flow was only able to further affect the medium sized LSB particles in experiments with 15 MPa. Experiments with the S1 geometry exhibited a uniform velocity distribution for SL particles for 8 and 15 MPa, whereas LSB particles were ejected faster on the right (more diverging) side of the vent. As a consequence of the asymmetric divergence angle of S1, the right (more diverging) side of the vent had a higher M and accordingly, higher gas velocities were reached on this side. Within the conduit the acceleration was uniform and unilaterally, but once the gas and particles reached the diverging section the gas was able to accelerate stronger on $\sim 40°$ side. The inertia of SL particles prevented that this additional acceleration became evident, whereas the coupling between gas and particles was sufficient to be reflected by the velocity of the LSB particles.

These observations can be interpreted when considering calculated non-dimensional fluid dynamic parameters based on the starting conditions of the experiments. We stress again that those values can only be regarded as conservative upper values as the impulsive nature of the experiments and the comparatively small autoclave volume caused highly dynamic conditions with only short periods during which a jet can be considered quasi-static (Peña Fernández et al., 2020). Only for the fine particles, St was close to 1, meaning that initially vertically and later additionally horizontally expanding gas allowed for more efficient acceleration within the autoclave and deflection (during the starting phase of particle ejection) above the vent. Since St was > 1 for medium and coarse particles of both densities, lateral deflection above the vent could be observed to a lesser degree. The particles followed trajectories dominated by inertia. While the gas flow likely started deceleration at or shortly after leaving the vent, the particle's inertia prevented measurable deceleration in our field of view. The fun30 vent geometry exhibited a higher ejection velocity than the other vent geometries. The higher exit-to-critical-area ratio and the higher M facilitated faster gas velocities than in experiments with the cyl30 vent. According to fluid dynamic theory [Saad, 1985], the S1 vent with an even higher M should have produced a higher velocity. However, this was highly dependent on the exit pressure. A certain minimum pressure is required to positively correlate the exit-to-critical-area ratio and the M at the exit (Cigala et al., 2017). It seemed that the pressure had already dropped below the required minimum pressure as the particles arrived at the vent exit preventing a higher particle velocity.

The experiments with the S1 geometry provide a proof of concept for incorporating novel techniques like UAV photogrammetry and 3D printing into the conception of experiments by bringing "real" volcanic geometries into the laboratory. A combination of high resolution, high-speed observations of the near-vent dynamics of volcanic explosions and scaled laboratory experiments utilising the associated "real" geometry can ultimately lead to establishing the link between observable features and the shallow subsurface boundary conditions.

4.5.3 Linking experiments to volcanic hazards

Although the dynamics of the experiments presented in this study did not allow observations beyond the near-vent region, the impact of complex vent geometries on gas-particle ejection can be applied to explosive volcanic eruptions by including field observations and published studies (e.g., Andrews and Gardner, 2009; Jessop and Jellinek, 2014; Jessop et al., 2016; Lagmay et al., 1999; Lherm and Jellinek, 2019; Solovitz et al., 2014). Vent geometry is one of the prime factors controlling the initial ejection of pyroclasts. The particles used in the present study showed a variable degree of coupling as a function of size and density and different ratios between particle size and conduit diameter (Table 4.1), mimicking a wide range of volcanic ejecta. The gas flow initially accelerated the largest particles but they soon decoupled and continued on inertia-controlled ballistic trajectories. The (asymmetric) vent geometry thereby controlled the maximum ejection angle and velocity. In nature, the general trajectory of volcanic ballistics directly results from vent and/or crater geometry, explosion depth, conduit inclination, and secondary effects (e.g., vent coverage or clogging, presence of a high viscosity layer). The resulting trajectory is then further modified by a plethora of complex factors like drag forces, altitude, Earth rotational and Coriolis effects, the surrounding expanding gas, in-flight particle collisions and particle deformation (e.g., Bower and Woods, 1996; Fagents and Wilson, 1993; Gaudin et al., 2016; Saunderson, 2008; Sherwood, 1967; Taddeucci et al., 2017; Vanderkluysen et al., 2012; Wilson, 1972). However, the prime impulses affecting the maximum travelling distance are ejection angle and velocity.

The asymmetric particle ejection angle and velocity can alter entrainment processes unilaterally. Trajectories that deviate from a vertical ejection can deform the size of entrainment eddies, increasing the penetration distance of the eddy compared to vertical trajectories (Jessop and Jellinek, 2014). This effect might be especially strong for weakly coupled particles since their trajectories disturb the rotational motion of the eddies, increasing mixing rates and entrainment at the boundary layer (Lherm and Jellinek, 2019). The experiments described by Jessop and Jellinek (2014) and Lherm and Jellinek (2019) describe the particle ejection into a water-filled tank describing a different regime that might not allow a direct comparison to the compressible regime. Solovitz et al. (2014) observed an asymmetric ejection of the solid and fluid phases in experiments with erodible vents and gas-particle jets. They suggested that this asymmetric ejection may lead to partial fountain collapse. When a jet fails to entrain sufficient air to decrease its density below ambient levels, the asymmetry of the jet in the near vent region can lead to a preferential directionality of PDCs. In nature, collapse directions were linked to vent/crater asymmetry on several occasions, e.g., Mount St. Helens 1980 (Andrews and Gardner, 2009), Mayon 1988 (Lagmay et al., 1999), Soufrière Hills 2010 (Cole et al., 2015) and Chaiten 2008–2009 (Major et al., 2013).

There are different mechanisms of how the vent and/or crater asymmetry can influence the direction of (partial) collapse of eruption columns. In Figure 4.7A and 4.7B, for example, the emitted gas-pyroclast jets are tilted as result of the vent geometry. The (partial) collapse of inclined eruption columns — either due to vent asymmetry or an inclined conduit — will cause locally concentrated fallout and a preferential direction of PDCs. The link between inclined jets and vent asymmetry was demonstrated numerically (Lagmay et al., 1999) and experimentally by Schmid et al. (2020) and in the present study. This link is especially relevant for supersonic jets (Sim and Ogden, 2012), where jet conditions (underexpanded/overexpanded) determine whether the jet is inclined towards the high or low side of the vent. For supersonic underexpanded jets, the preferred collapse direction is to the lowest side of the vent (Figure 4.7A), while a supersonic overexpanded jet will focus the collapse towards the highest side of the vent (Figure 4.7B) (Lagmay et al., 1999; Schmid et al., 2020).

If the characteristic asymmetry element is a varying divergence angle instead of a high and low vent exit side, the preferred direction for volcanic fallout and PDCs will be towards the more diverging side (Figure 4.7C) as a result of the asymmetric particle distribution. In the experiments presented in this study the observation of asymmetric particle spreading angle suggests this behaviour.

In addition to vent geometry, the collapse direction can be affected by the asymmetry of the surrounding crater or topography. Jet and plume flow direction is partially restricted and consequentially deflected back- and upwards, locally increasing the bulk density (Figure 4.7D). The physical barrier might also limit air entrainment and restrict column radius, which leads to asymmetric column growth. PDCs following (partial) collapse will be directed towards topographic lows. Partial column collapses and directed PDCs due to asymmetric crater geometry was described by Andrews and Gardner (2009) for the 1980s eruption of Mount St. Helens. The dynamics of the experiments presented in this study do not permit an analysis of the criteria for column collapse. Hence, we cannot state whether the utilised complex vent geometries promote collapse over a symmetric geometry. However, based on our observations of particle trajectories and jet inclination and direct eruption observations, numerical models, and experiments, we suggest: The asymmetric gas-particle jet spreading angles can initially encourage entrainment because of the increased surface area of the jet's boundary layer and increased penetration depth of the entrainment eddies until certain threshold conditions are reached (e.g., vent radius, mass eruption rate, ejection velocity). A comprehensive description of factors governing

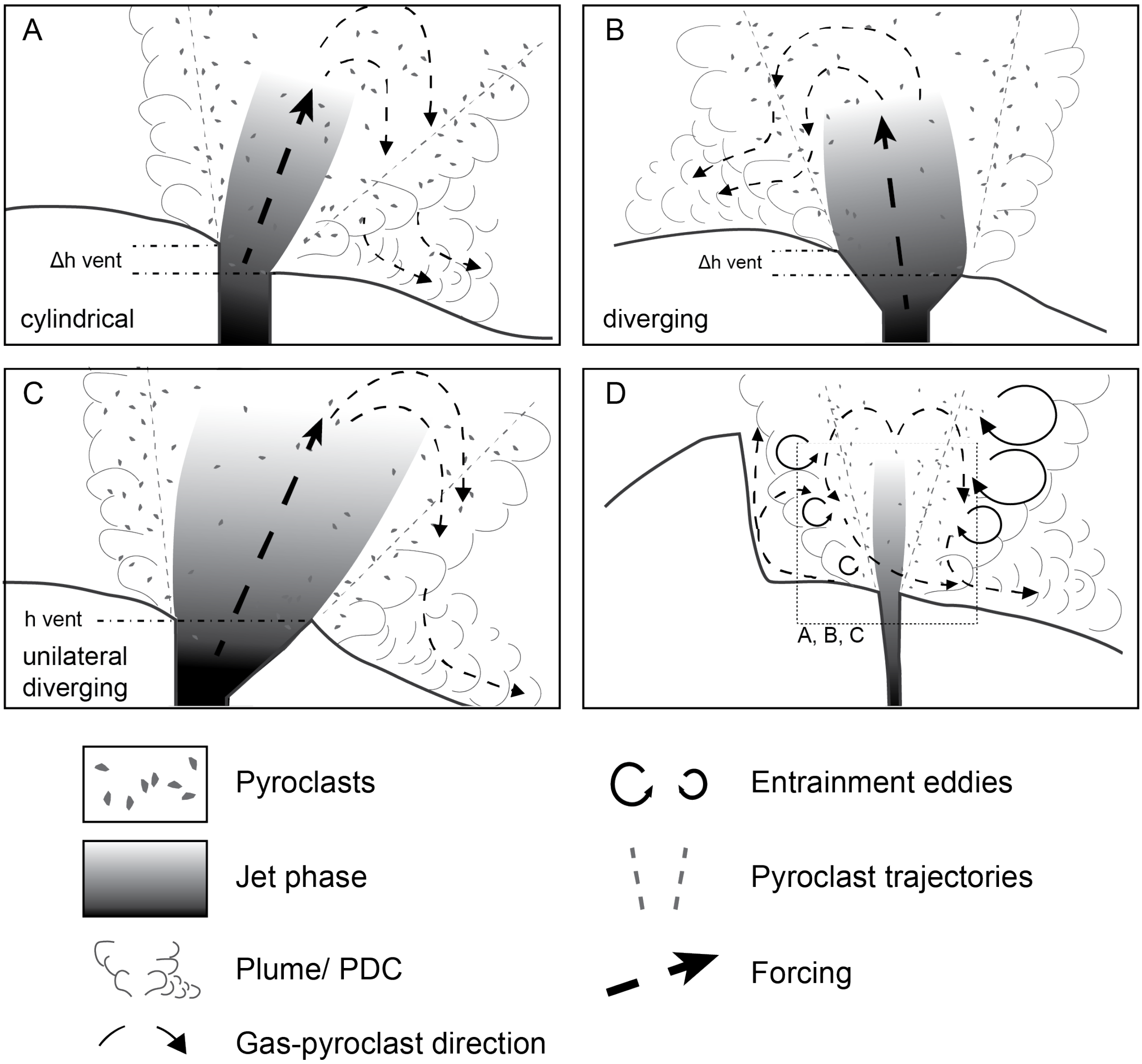

Figure 4.7: Sketch of possible collapse scenarios. In A) and B) the characteristic asymmetry element is the different vent exit height. The difference of the inner vent geometry (cylindrical and diverging) governs the inclination of the jet as a result of the decompression efficiency. In C) the asymmetric divergence describes the vent geometry. D) shows a larger field of view including the surrounding topography.

buoyant rise versus column collapse is beyond the scope of this study but have been described in numerous studies (e.g., Chojnicki et al., 2015; Dellino et al., 2014; Jessop et al., 2016; Koyaguchi et al., 2010; Lherm and Jellinek, 2019; Neri et al., 2003; Saffaraval et al., 2012; Sparks et al., 1978; Suzuki et al., 2020; Woods, 1988, 2010). We propose that an asymmetric vent and/or crater geometry facilitates the asymmetric distribution of volcanic ejecta and, in case a column collapse occurs, a preferential direction for ensuing PDCs.

4.6 Conclusion

The rapid decompression experiments performed in the present study investigated the link between vent geometry, particle size and density, and pressure and their impact on the eruption dynamics. In the laboratory, vent geometry determined the direction of the emitted gas-particle jet. The cyl30 vent promoted the largest particle spreading angles, while the fun30 vent exhibited the highest velocities. The S1 geometry had the strongest asymmetry regarding the jet spreading angle. Both cyl30 and fun30 vents exhibited a larger spreading angle and a higher particle velocity (for LSB particles) on the left (lower) vent side than the right (higher) vent side. S1 showed a larger spreading angle and faster particles (for LSB particle) on the side with the stronger divergence. In order of importance, the maximum particle spreading angle had

- a negative correlation with particle size
- a negative correlation with particle density
- positive correlation with experimental pressure

The particle ejection velocity had

- a negative correlation with particle density
- a positive correlation with experimental pressure
- a negative correlation with particle size

The results of the scaled laboratory experiments performed here showed the significance of vent geometry and the major effect of asymmetry on the ejection of multiphase flows. These findings can be applied to interpret observable volcanic eruptions dynamics. The asymmetry of the vent and/or crater can impact areas affected by proximal and distal volcanic hazards. Furthermore, a comparison of the experimental data with field observations (Schmid et al., 2021) demonstrated the feasibility of using novel techniques to produce realistic vent geometries for laboratory experiments. The combination of UAV photogrammetry and additive 3D printing is a rapid and inexpensive way to utilise realistic volcanic vent geometries in scaled laboratory experiments.
Ultimately, we need increasingly complex experiments to explore the link between observable eruption dynamics and the underlying, concealed boundary conditions that, to date, have remained beyond direct observation and measurements.

Chapter 5

Conclusion

The goal of this thesis was to further investigate the link between vent geometry, boundary conditions and the dynamics of explosive eruptions. While boundary conditions are unobservable and to date unconstrained for natural eruptions, they can be controlled reliably and repeatedly in the experiments presented here. This has been done by designing increasingly complex vent geometries, partially based on direct observations, and meticulously observed eruption dynamics in the near-vent region. In order to achieve this, I combined data and observations from five field surveys and experiments. I used the field data to identify common geometrical features contributing to the asymmetry of volcanic vents and I quantified their evolution. The findings of the high-resolution vent characterisation were incorporated in the design of six vent geometries that mimic a variable vent exit height by a slanted exit plane. As a first step, gas-only experiments were performed to analyse the effect of two inner vent geometries (cylindrical and diverging), each with 5°, 15° and 30° slant angle, four pressure steps (5, 8, 15 and 25 MPa) and two autoclave volumes (127.4 cm^3 and 31.9 cm^3). For the second set of experiments I used two of the existing vent geometries (cylindrical 30° slant and diverging 30° slant), a realistic vent geometry (S1), six granular samples (SL and LSB, each with 0.125–0.25, 0.5–1 and 1–2 mm grain size) and two pressures (8 and 15 MPa).

The field surveys revealed that volcanic vents and craters often exhibit highly irregular and asymmetric geometries that can be transient. UAV photogrammetry enabled a quantification of these processes at unprecedented spatiotemporal resolution. It was possible to evaluate the processes during "normal" Strombolian activity, with predominantly near-vent deposition of erupted material, as well as "major eruptions" where explosive excavation severely altered the vent geometry on a short timescale. The two paroxysms on 3 July and 28 August changed the morphology of larger portions of the crater terrace facilitating shifts of vent locations and the opening of new vents. Both major and paroxysmal eruptions and the changes to the vents induced by them affected eruption dynamics. This highlighted that geometric features of volcanic vents and/or craters can exert a prime control on explosive volcanic activity. Hereby, increasing the asymmetry of a vent led to an asymmetric distribution of the associated eruption products. The high temporal and spatial resolution of UAV surveys may allow a quantification of erupted mass, a as of yet crudely constrained eruption parameter.

The scaled shock-tube experiments helped to quantify the control exerted by the vent geometry for variable boundary conditions:

- Six complex vent geometries (cyl05, cyl15, cyl30, fun05, fun15, fun30)
- One realistic vent geometry (S1)
- Four experimental pressures (5, 8, 15, 25 MPa)
- Six granular samples (SL 0.125–0.5 mm, 0.5–1 mm, 1–2 mm; LSB 0.125–0.25 mm, 0.5–1 mm, 1–2 mm)
- Two autoclave volumes (127.4^2 and 31.9 cm^2)

The gas-only rapid decompression experiments with a vertical, cylindrical reservoir revealed the following positive correlations: The *pressure ratio* correlated positively with 1) the maximum spreading angle of the gas jet, 2) the maximum jet inclination for cylindrical vents, and 3) the duration of the underexpanded character of the jet. The *slant angle* correlated positively with 1) the maximum spreading angle of the gas jet and 2) the maximum jet inclination for cylindrical vents. Moreover, the *inner vent geometry* (cylindrical versus diverging) influenced the direction of the jet inclination in two distinct ways, 1) towards the direction of the exit plane dip for cylindrical vents and 2) against the direction of the exit plane dip for diverging vents. Additionally, cylindrical vents produced a larger spreading angle than diverging vents. The *reservoir volume* showed positive correlation with maximum gas spreading angle but no significant impact on maximum jet inclination.

In experiments including particles the vent geometry affected the direction, the spreading angle and the velocity of the gas-particle jet. The cyl30 vent promoted the largest particle spreading angle, while the fun30 exhibited the highest particle velocity. The S1 geometry had the strongest asymmetry regarding particle spreading angle and particle velocity. Both, cyl30 and fun30 vents exhibited a larger spreading angle and a higher particle velocity (for LSB particles) on the left (lower) vent side than on the left (high) side. S1 showed the largest spreading angle and the fastest particles (for LSB particle) on the right (stronger diverging) side. *Particle size* and *particle density* had a negative correlation with particle spreading angle and particle velocity. The initial *experimental pressure* showed a positive correlation with both, particle spreading angle and particle velocity.

The combination of field and laboratory data revealed that (asymmetric) vent and/or crater geometry can lead to inclined jets, asymmetric particle spreading and a non-uniform particle velocity distribution. As a function of underlying boundary conditions and the vent and crater geometry this can influence areas that are affected by volcanic explosions in the near and far field. As a consequence, vent/crater geometry and their evolution should be incorporated in the standard monitoring routine to improve the assessment of areas at risk. This can easily be obtained by UAV observations since they can be conducted fast, inexpensively and safely, even in times of heightened volcanic activity. Furthermore, the combination of field and laboratory work should be strengthened. With new technologies at our disposal it has become an achievable goal to investigate the shallow subsurface boundary conditions of volcanic explosions. A way of accomplishing this could be a combination of using repeated high-resolution UAV photogrammetry and high-speed imaging at frequently erupting volcanoes. The photogrammetric data can be used to characterize the vent/crater geometry, quantify the erupted mass and the dispersal of pyroclasts of small scale eruptions while high-speed recordings can capture the near-vent dynamics of the related explosion. Additionally, the photogrammetric data can be used to produce a 3D printed model of the vent that can be used in scaled laboratory experiments where near-vent dynamics can be recorded at a high temporal resolution as well. As the boundary conditions are precisely controlled in the laboratory, a comparison of the near-vent dynamics in nature and the laboratory aids to empirically constrain the boundary conditions of the volcanic explosion.

Appendix A

Chapter 2

Table A.1: Survey data for the five UAV campaigns between May 2019 and January 2020.

	Resolution [cm/pix]			
	GSD	DEM	Orthomosaic	Coverage area [km^2]
May 2019	4.21	8.41	4.21	0.35
June 2019	3.81	7.62	3.81	0.287
August 2019	5.76	11.5	5.76	0.317
September 2019	4.28	8.56	4.28	0.34
January 2020	4.33	8.67	4.33	0.519

Table A.2: Flight parameters for the five survey flights perfomed between May 2019 and January 2020. The flight name corresponds to the internal LMU labelling.

Flight	Flight path	Flight conditions	Illumination	Images	No. Images	Oblique
#2_May11	double grid	good	sunny	320	132	yes
#17_June12	double grid	strong winds	sunny	129	129	no
Aug-04	circular	strong degassing	sunny	220	108	yes
#21_Sept23	double grid	moderate degassing	overcast	177	175	no
#31_Jan25	single grid	strong degassing	overcast	119	103	yes

Table A.3: Levels of eruptive activity between May 2019 and January 2020 as reported by the weekly and daily reports “Bollettini multidisciplinary” by INGV Osservatorio Etneo Sezione Cataniaa. Activity level is given as events per hour for the entire volcano and both N and SC vent areas. Where available, the minimum number of active vents is given for the N and SC vent area; n.a. indicates that data were not available.

Date range from	to	Total activity [events/h]	N activity [events/h]	SC activity [events/h]	Min. No. of vents in N	Min. No. of vents in SC
4/29/19	5/5/19	15-23	3-8	11-14	2	3
5/6/19	5/12/19	10-16	4-5	6-11	2	3
5/13/19	5/19/19	n.a.	n.a.	n.a.	n.a.	n.a.
5/20/19	5/26/19	11-16	3-7	11-16	2	3
5/27/19	6/2/19	7-11	2-4	5-8	2	3
6/3/19	6/9/19	n.a.	n.a.	n.a.	n.a.	n.a.
6/10/19	6/16/19	17-21	2-12	2-15	2	3
6/17/19	6/23/19	16-24	3-9	11-17	2	5
6/24/19	6/30/19	17-25	3-11	9-16	2	5
7/1/19	7/7/19	13-25	2-11	9-16	2	3
7/8/19	7/14/19	15-22	4-9	10-16	n.a.	n.a.
7/15/19	7/21/19	12-24	4-10	6-17	n.a.	n.a.
7/22/19	7/28/19	10-26	6-16	4-10	6	2
7/29/19	8/4/19	13-21	6-16	4-10	8	2
8/5/19	8/11/19	19-22	14-17	4-6	9	1
8/12/19	8/18/19	n.a.	n.a.	n.a.	n.a.	n.a.
8/19/19	8/25/19	18-26	7-15	9-16	n.a.	n.a.
8/26/19	9/1/19	36	n.a.	n.a.	3	1
9/2/19	9/8/19	18-36	7-25	5-25	n.a.	n.a.
9/9/19	9/15/19	26-34	15-23	8-14	n.a.	n.a.
9/16/19	9/22/19	20-35	8-15	10-15	n.a.	n.a.
9/23/19	9/29/19	11-20	4-6	10-12	n.a.	n.a.
9/30/19	10/6/19	12-15	4-6	7-10	n.a.	n.a.
10/7/19	10/13/19	10-19	5-8	9-12	n.a.	n.a.
10/14/19	10/20/19	4-40	2-22	2-16	n.a.	n.a.
10/21/19	10/27/19	2-35	0-20	1-12	n.a.	n.a.
10/28/19	11/3/19	5-22	2-9	7-11	n.a.	n.a.
11/4/19	11/10/19	16-29	4-10	10-14	3	3
11/11/19	11/17/19	16-24	6-16	7-13	3	3
11/18/19	11/24/19	6-20	5-11	1-10	3	3
11/25/19	12/1/19	11-17	7-11	4-8	3	3
12/2/19	12/8/19	12-24	6-11	6-13	3	3
12/9/19	12/15/19	14-23	6-12	7-12	3	3
12/16/19	12/22/19	13-32	9-19	2-13	3	3
12/23/19	12/29/19	15-23	3-17	6-12	3	3
12/30/19	1/5/20	16-26	8-15	7-12	3	3
1/6/20	1/12/20	16-30	3-22	7-16	3	3
1/13/20	1/19/20	13-23	2-12	11-13	3	3
1/20/20	1/26/20	15-20	5-8	9-14	3	3

Appendix B

Chapter 4

Table B.1: Vent exit pressure (P_{vent}) is affected by the starting pressure (P_{start}) of the experiment and vent geometry. The pressure at the vent was measured with a KISTLER 601A pressure sensor just below the lower vent exit side. The S1 vent was not equipped with a pressure sensor at the vent. P_{start} was measured at the top of the autoclave. Experiments where no pressure could be determined, either because no vent sensor was installed or a bad signal to noise ratio are marked as n.n..

Experiment	0.125–0.25 mm		0.5–1 mm		1–2 mm	
	P_{vent} [MPa]	P_{start} [MPa]	P_{vent} [MPa]	P_{start} [MPa]	P_{vent} [MPa]	P_{start} [MPa]
cyl30						
SL, 8 MPa	n.a.	8.4	n.a.	n.a.	2.3	8.2
SL, 15 MPa	n.a.	15.5	2.7	15.2	0.7	15.3
LSB, 8 MPa	n.a.	n.a.	2.5	8.3	2.1	8.3
LSB, 15 MPa	n.a.	n.a.	4.0	15.2	3.8	15.4
fun30						
SL, 8 MPa	0.3	8.2	0.4	8.2	0.3	8.3
SL, 15 MPa	0.4	15.2	0.5	15.3	n.a.	15.4
LSB, 8 MPa	0.8	8.1	0.3	8.0	0.4	8.0
LSB, 15 MPa	0.7	15.1	0.6	15.1	0.4	15.3
S1						
SL, 8 MPa	n.a.	8.2	n.a.	8.1	n.a.	8.2
SL, 15 MPa	n.a.	15.2	n.a.	15.2	n.a.	15.3
LSB, 8 MPa	n.a.	8.2	n.a.	8.3	n.a.	8.2
LSB, 15 MPa	n.a.	15.2	n.a.	15.2	n.a.	15.1

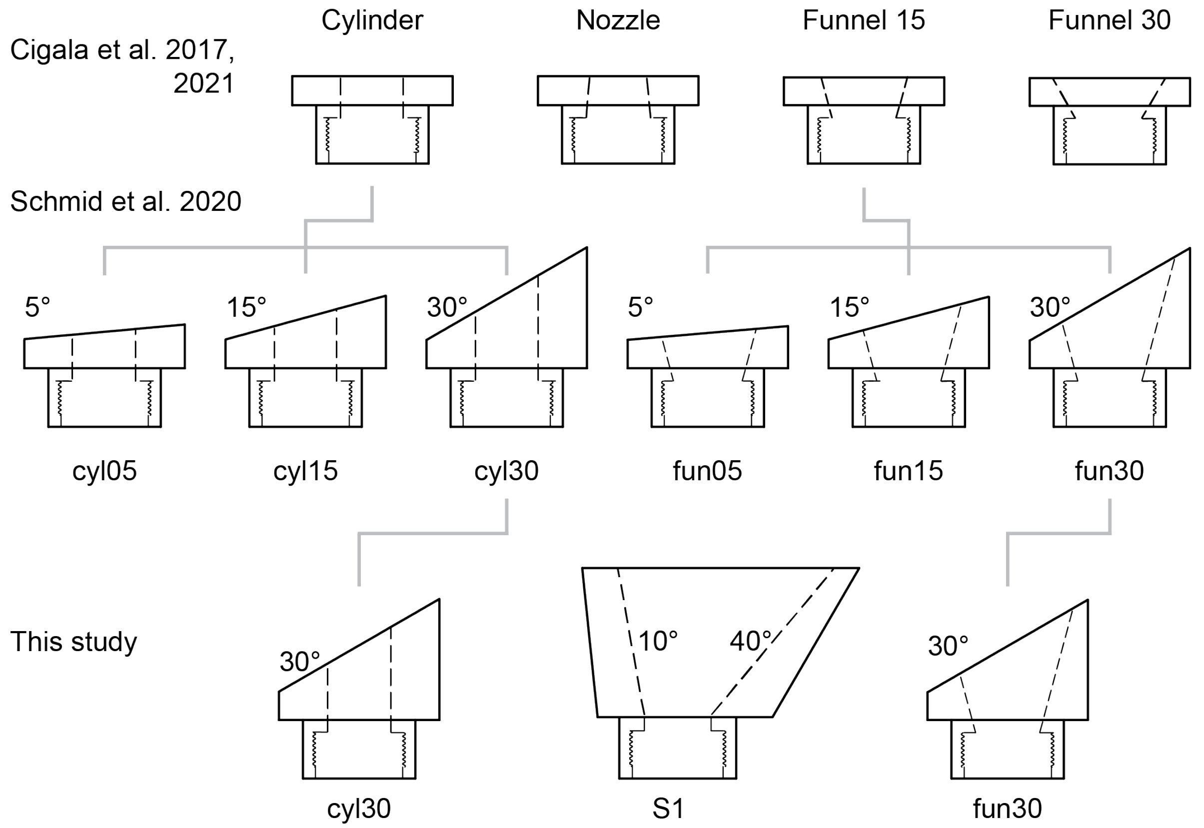

Figure B.1: Evolution of experimental vent geometries used in rapid decompression experiments at LMU Munich. The vents in the first row were used by Cigala et al. (2017, 2021). They have a radial symmetry with varying exit diameters. Out of these four vents, two were selected and modified with a slanted exit plane (5°, 15°, 30°) to reduce the level of symmetry. These vents were used by Schmid et al. (2020) in gas-only experiments. The two vents with the strongest effect on the dynamics of gas jets were selected for the current study. They were complemented by a third vent based on the geometry of Stromboli's S1 vent with an asymmetric divergence. All vents are sketched in a cross-sectional view.

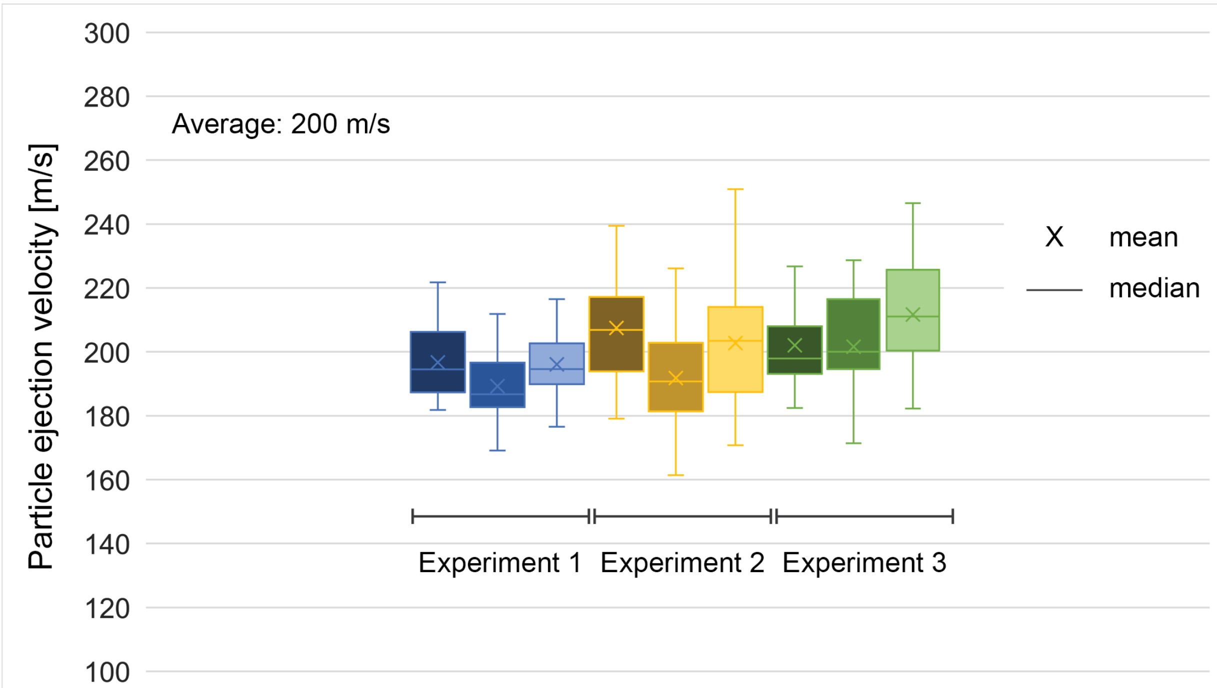

Figure B.2: Test of reproducibility of particle velocity. Three repetitions of the same experimental conditions (fun30, SL 1–2 mm, 15 MPa) were analysed three times each. Every analysis was conducted independently and 25 particles were measured during each analysis. The 25 particles were selected unbiased; hence it is possible that some particles were measured in multiple analysis. The box shows the quartiles calculated with an exclusive median. The cross marks the mean value and the line in the box marks the median.

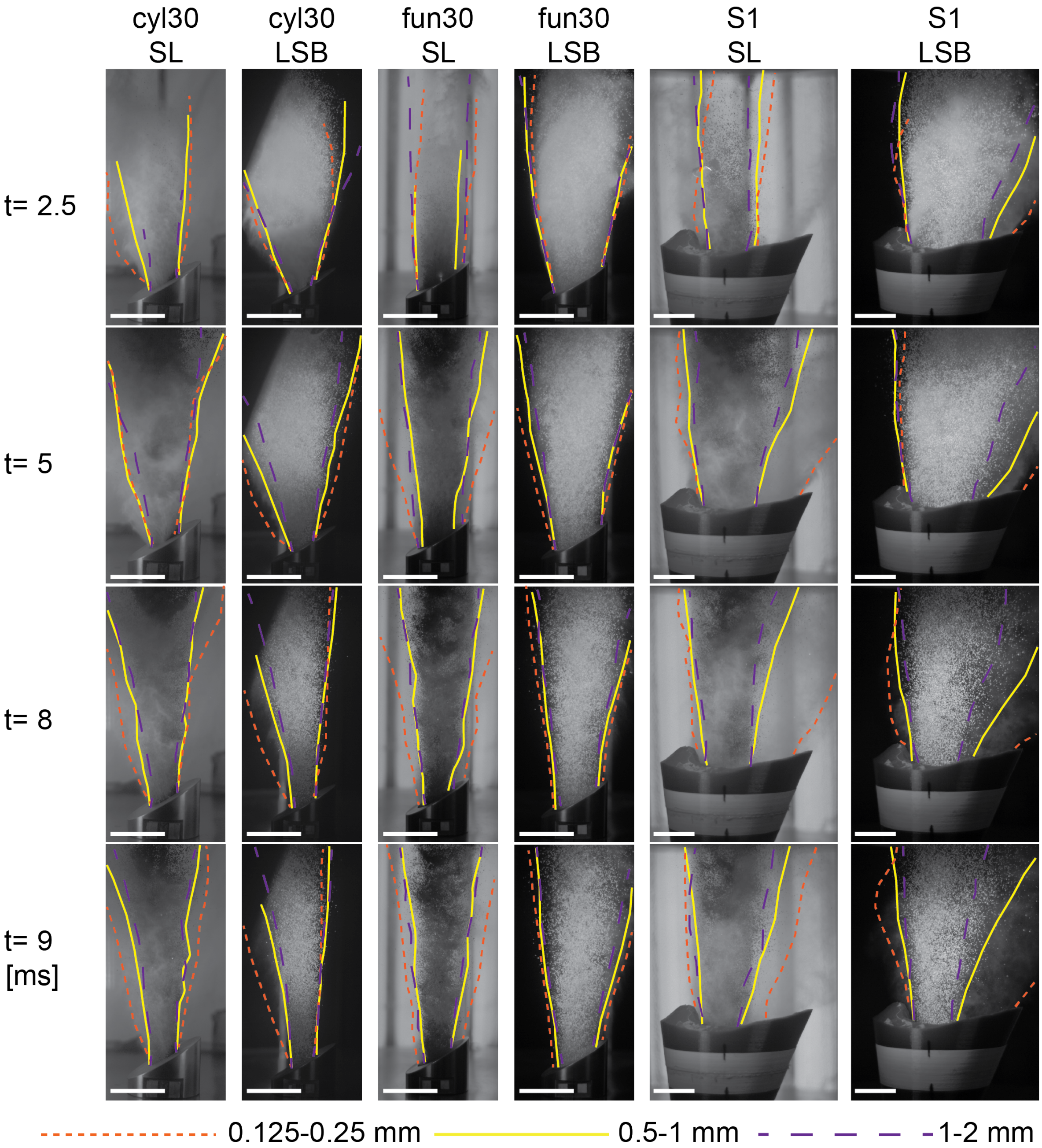

Figure B.3: Time series of jet spreading angles at 8 MPa experimental pressure. Each vertical column shows the temporal evolution of particle ejection, with four rows at 2.5, 5, 8, and 9 ms after the onset of the gas ejection. The columns represent six different experimental conditions, using particles of two different densities (SL, LSB) and 3 different vent geometries (cyl30, fun30, S1). Colour lines mark the outlines of particle ejection. For every individual stack of images, the corresponding image from the experiment with 8 MPa and 0.5–1 mm particles was taken as basis. t_0 is defined as the onset of gas ejection and the scale bar shows 5 cm. This Figure was created as shown in Figure 4.3. Refer to Figure4.5 for the 15 MPa experiments.

Bibliography

Alatorre-Ibargüengoitia, M. A., Delgado-Granados, H., and Dingwell, D. B. (2012). Hazard map for volcanic ballistic impacts at popocatépetl volcano (mexico). *Bulletin of volcanology*, 74(9):2155–2169.

Alatorre-Ibargüengoitia, M. A., Morales-Iglesias, H., Ramos-Hernández, S. G., Jon-Selvas, J., and Jiménez-Aguilar, J. M. (2016). Hazard zoning for volcanic ballistic impacts at el chichón volcano (mexico). *Natural Hazards*, 81(3):1733–1744.

Alatorre-Ibargüengoitia, M. A., Scheu, B., and Dingwell, D. B. (2011). Influence of the fragmentation process on the dynamics of vulcanian eruptions: An experimental approach. *Earth and Planetary Science Letters*, 302(1):51–59.

Alatorre-Ibargüengoitia, M. A., Scheu, B., Dingwell, D. B., Delgado-Granados, H., and Taddeucci, J. (2010). Energy consumption by magmatic fragmentation and pyroclast ejection during vulcanian eruptions. *Earth and Planetary Science Letters*, 291(1-4):60–69.

Alidibirov, M. and Dingwell, D. B. (1996a). An experimental facility for the investigation of magma fragmentation by rapid decompression. *Bulletin of Volcanology*, 58(5):411–416.

Alidibirov, M. and Dingwell, D. B. (1996b). Magma fragmentation by rapid decompression. *Nature*, 380(6570):146.

Alsoufi, M. S. and Elsayed, A. E. (2017). How surface roughness performance of printed parts manufactured by desktop fdm 3d printer with pla+ is influenced by measuring direction. *American Journal of Mechanical Engineering*, 5(5):211–222.

Andrews, B. J. and Gardner, J. E. (2009). Turbulent dynamics of the 18 may 1980 mount st. helens eruption column. *Geology*, 37(10):895–898.

Andronico, D., Cristaldi, A., Del Carlo, P., and Taddeucci, J. (2009). Shifting styles of basaltic explosive activity during the 2002–03 eruption of mt. etna, italy. *Journal of Volcanology and Geothermal Research*, 180(2-4):110–122.

Andronico, D., Taddeucci, J., Cristaldi, A., Miraglia, L., Scarlato, P., and Gaeta, M. (2013). The 15 march 2007 paroxysm of stromboli: video-image analysis, and textural and compositional features of the erupted deposit. *Bulletin of volcanology*, 75(7):733.

Anilkumar, A., Sparks, R., and Sturtevant, B. (1993). Geological implications and applications of high-velocity two-phase flow experiments. *Journal of Volcanology and Geothermal Research*, 56(1-2):145–160.

Arciniega-Ceballos, A., Alatorre-Ibargüengoitia, M., Scheu, B., and Dingwell, D. (2015). Analysis of source characteristics of experimental gas burst and fragmentation explosions generated by rapid decompression of volcanic rocks. *Journal of Geophysical Research: Solid Earth*, 120(7):5104–5116.

Arun Kumar, R. and Rajesh, G. (2017). Shock transformation and hysteresis in underexpanded confined jets. *Journal of Fluid Mechanics*, 823:538–561.

Auker, M. R., Sparks, R. S. J., Siebert, L., Crosweller, H. S., and Ewert, J. (2013). A statistical analysis of the global historical volcanic fatalities record. *Journal of Applied Volcanology*, 2(1):1–24.

Barberi, F. (1993). Volcanic hazard assessment at stromboli based on review of historical data. *Acta Vulcanologica*, 3:173–187.

Belousov, A., Voight, B., and Belousova, M. (2007). Directed blasts and blast-generated pyroclastic density currents: a comparison of the bezymianny 1956, mount st helens 1980, and soufrière hills, montserrat 1997 eruptions and deposits. *Bulletin of Volcanology*, 69(7):701.

Bercovici, D. and Michaut, C. (2010). Two-phase dynamics of volcanic eruptions: compaction, compression and the conditions for choking. *Geophysical Journal International*, 182(2):843–864.

Bertagnini, A., Coltelli, M., Landi, P., Pompilio, M., and Rosi, M. (1999). Violent explosions yield new insights into dynamics of stromboli volcano. *Eos, Transactions American Geophysical Union*, 80(52):633–636.

Bertolaso, G., De Bernardinis, B., Bosi, V., Cardaci, C., Ciolli, S., Colozza, R., Cristiani, C., Mangione, D., Ricciardi, A., and Rosi, M. (2009). Civil protection preparedness and response to the 2007 eruptive crisis of stromboli volcano, italy. *Journal of Volcanology and Geothermal Research*, 182(3-4):269–277.

Blong, R. J. (2013). *Volcanic hazards: a sourcebook on the effects of eruptions*. Elsevier.

Bonaccorso, A. (1998). Evidence of a dyke-sheet intrusion at stromboli volcano inferred through continuous tilt. *Geophysical research letters*, 25(22):4225–4228.

Bower, S. M. and Woods, A. W. (1996). On the dispersal of clasts from volcanic craters during small explosive eruptions. *Journal of Volcanology and Geothermal Research*, 73(1-2):19–32.

Brown, S. K., Jenkins, S. F., Sparks, R. S. J., Odbert, H., and Auker, M. R. (2017). Volcanic fatalities database: analysis of volcanic threat with distance and victim classification. *Journal of Applied Volcanology*, 6(15):1–20.

Burgisser, A., Bergantz, G. W., and Breidenthal, R. E. (2005). Addressing complexity in laboratory experiments: the scaling of dilute multiphase flows in magmatic systems. *Journal of Volcanology and Geothermal Research*, 141(3):245–265.

Cagnoli, B., Barmin, A., Melnik, O., and Sparks, R. S. J. (2002). Depressurization of fine powders in a shock tube and dynamics of fragmented magma in volcanic conduits. *Earth and Planetary Science Letters*, 204(1):101–113.

Calvari, S., Bonaccorso, A., Madonia, P., Neri, M., Liuzzo, M., Salerno, G. G., Behncke, B., Caltabiano, T., Cristaldi, A., and Giuffrida, G. (2014). Major eruptive style changes induced by structural modifications of a shallow conduit system: the 2007–2012 stromboli case. *Bulletin of volcanology*, 76(7):841.

Calvari, S., Spampinato, L., Bonaccorso, A., Oppenheimer, C., Rivalta, E., and Boschi, E. (2011). Lava effusion—a slow fuse for paroxysms at stromboli volcano? *Earth and Planetary Science Letters*, 301(1-2):317–323.

Calvari, S., Spampinato, L., and Lodato, L. (2006). The 5 april 2003 vulcanian paroxysmal explosion at stromboli volcano (italy) from field observations and thermal data. *Journal of Volcanology and Geothermal research*, 149(1-2):160–175.

Capponi, A., Taddeucci, J., Scarlato, P., and Palladino, D. M. (2016). Recycled ejecta modulating strombolian explosions. *Bulletin of Volcanology*, 78(2):13.

Carcano, S., Bonaventura, L., Ongaro, T. E., and Neri, A. (2013). A semi-implicit, second-order-accurate numerical model for multiphase underexpanded volcanic jets. *Geoscientific Model Development*, 6(6):1905.

Carcano, S., Esposti Ongaro, T., Bonaventura, L., and Neri, A. (2014). Influence of grain-size distribution on the dynamics of underexpanded volcanic jets. *Journal of Volcanology and Geothermal Research*, 285:60–80.

Cashman, K. V. and Sparks, R. S. J. (2013). How volcanoes work: A 25 year perspective. *GSA bulletin*, 125(5-6):664–690.

Cerminara, M., Esposti Ongaro, T., and Neri, A. (2016). Large eddy simulation of gas–particle kinematic decoupling and turbulent entrainment in volcanic plumes. *Journal of Volcanology and Geothermal Research*, 326:143–171.

Charbonnier, S. J., Germa, A., Connor, C. B., Gertisser, R., Preece, K., Komorowski, J. C., Lavigne, F., Dixon, T., and Connor, L. (2013). Evaluation of the impact of the 2010 pyroclastic density currents at merapi volcano from high-resolution satellite imagery, field investigations and numerical simulations. *Journal of Volcanology and Geothermal Research*, 261:295–315.

Chojnicki, K., Clarke, A., Phillips, J., and Adrian, R. (2015). Rise dynamics of unsteady laboratory jets with implications for volcanic plumes. *Earth and Planetary Science Letters*, 412:186–196.

Chojnicki, K., Clarke, A. B., and Phillips, J. C. (2006). A shock-tube investigation of the dynamics of gas-particle mixtures: Implications for explosive volcanic eruptions. *Geophysical Research Letters*, 33(15).

Chouet, B., Dawson, P., Ohminato, T., Martini, M., Saccorotti, G., Giudicepietro, F., De Luca, G., Milana, G., and Scarpa, R. (2003). Source mechanisms of explosions at stromboli volcano, italy, determined from moment-tensor inversions of very-long-period data. *Journal of Geophysical Research: Solid Earth*, 108(B1):ESE–7.

Cigala, V., Kueppers, U., Fernández, J. J. P., and Dingwell, D. B. (2021). Linking gas and particle ejection dynamics to boundary conditions in scaled shock-tube experiments. *Bulletin of Volcanology*, 83(8):53.

Cigala, V., Kueppers, U., Peña Fernández, J. J., Taddeucci, J., Sesterhenn, J., and Dingwell, D. B. (2017). The dynamics of volcanic jets: Temporal evolution of particles exit velocity from shock-tube experiments. *Journal of Geophysical Research: Solid Earth*, 122(8):6031–6045.

Clarke, A. B. (2013). *Unsteady explosive activity: Vulcanian eruptions*. Modeling Volcanic Processes: The Physics and Mathematics of Volcanism. Cambridge University Press, England.

Cole, P., Stinton, A., Odbert, H., Bonadonna, C., and Stewart, R. (2015). An inclined vulcanian explosion and associated products. *Journal of the Geological Society*, 172(3):287–293.

Dellino, P., Dioguardi, F., Mele, D., D'Addabbo, M., Zimanowski, B., Buettner, R., Doronzo, D. M., Sonder, I., Sulpizio, R., and Duerig, T. (2014). Volcanic jets, plumes, and collapsing fountains: evidence from large-scale experiments, with particular emphasis on the entrainment rate. *Bulletin of Volcanology*, 76(6):834.

Dempsey, D. E., Cronin, S. J., Mei, S., and Kempa-Liehr, A. W. (2020). Automatic precursor recognition and real-time forecasting of sudden explosive volcanic eruptions at whakaari, new zealand. *Nature communications*, 11(1):1–8.

Deo, R. C., Mi, J., and Nathan, G. J. (2007). The influence of nozzle-exit geometric profile on statistical properties of a turbulent plane jet. *Experimental Thermal and Fluid Science*, 32(2):545–559.

Dingwell, D. B. and Webb, S. L. (1990). Relaxation in silicate melts. *European Journal of Mineralogy*, 2(4):427–449.

Dioguardi, F., Dellino, P., and De Lorenzo, S. (2013). Integration of large-scale experiments and numerical simulations for the calibration of friction laws in volcanic conduit flows. *Journal of Volcanology and Geothermal Research*, 250:75–90.

Douillet, G. A., Rasmussen, K. R., Kueppers, U., Castro, D. L., Merrison, J. P., Iversen, J. J., and Dingwell, D. B. (2014). Saltation threshold for pyroclasts at various bedslopes: Wind tunnel measurements. *Journal of volcanology and geothermal research*, 278:14–24.

Druitt, T. H. (1998). Pyroclastic density currents. *Geological Society, London, Special Publications*, 145(1):145–182.

Dürig, T., Gudmundsson, M. T., and Dellino, P. (2015). Reconstruction of the geometry of volcanic vents by trajectory tracking of fast ejecta - the case of the eyjafjallajökull 2010 eruption (iceland). *Earth, Planets and Space*, 67(1):64.

Eltner, A., Kaiser, A., Castillo, C., Rock, G., Neugirg, F., and Abellán, A. (2016). Image-based surface reconstruction in geomorphometry-merits, limits and developments. *Earth Surface Dynamics*, 4(2):359–389.

Erfurt-Cooper, P. (2014). *Volcanic tourist destinations*. Springer Science & Business Media.

Erfurt-Cooper, P., Sigurdsson, H., and Lopes, R. M. C. (2015). *Volcanoes and tourism*, pages 1295–1311. Elsevier.

Fagents, S. A. and Wilson, L. (1993). Explosive volcanic eruptions—vii. the ranges of pyroclasts ejected in transient volcanic explosions. *Geophysical Journal International*, 113(2):359–370.

Freire, S., Florczyk, A. J., Pesaresi, M., and Sliuzas, R. (2019). An improved global analysis of population distribution in proximity to active volcanoes, 1975–2015. *ISPRS international journal of geo-information*, 8(8):341.

Gaudin, D., Taddeucci, J., Houghton, B. F., Orr, T. R., Andronico, D., Del Bello, E., Kueppers, U., Ricci, T., and Scarlato, P. (2016). 3-d high-speed imaging of volcanic bomb trajectory in basaltic explosive eruptions. *Geochemistry, Geophysics, Geosystems*, 17(10):4268–4275.

Gaudin, D., Taddeucci, J., Scarlato, P., Bello, E., Ricci, T., Orr, T., Houghton, B., Harris, A., Rao, S., and Bucci, A. (2017). Integrating puffing and explosions in a general scheme for strombolian-style activity. *Journal of Geophysical Research: Solid Earth*, 122(3):1860–1875.

Gaudin, D., Taddeucci, J., Scarlato, P., Moroni, M., Freda, C., Gaeta, M., and Palladino, D. M. (2014). Pyroclast tracking velocimetry illuminates bomb ejection and explosion dynamics at stromboli (italy) and yasur (vanuatu) volcanoes. *Journal of Geophysical Research: Solid Earth*, 119(7):5384–5397.

Giordano, G. and De Astis, G. (2021). The summer 2019 basaltic vulcanian eruptions (paroxysms) of stromboli. *Bulletin of Volcanology*, 83(1):1–27.

Giudicepietro, F., López, C., Macedonio, G., Alparone, S., Bianco, F., Calvari, S., De Cesare, W., Delle Donne, D., Di Lieto, B., and Esposito, A. M. (2020). Geophysical precursors of the july-august 2019 paroxysmal eruptive phase and their implications for stromboli volcano (italy) monitoring. *Scientific reports*, 10(1):1–16.

Glaze, L. S., Baloga, S. M., and Wimert, J. (2011). Explosive volcanic eruptions from linear vents on earth, venus, and mars: comparisons with circular vent eruptions. *Journal of Geophysical Research: Planets*, 116(E1).

Global Volcanism Program (2013). Volcanoes of the world, v. 4.10.1. Date accessed: 29.07.2021.

Gouhier, M. and Donnadieu, F. (2011). Systematic retrieval of ejecta velocities and gas fluxes at etna volcano using l-band doppler radar. *Bulletin of Volcanology*, 73(9):1139–1145.

Graettinger, A., Valentine, G., Sonder, I., Ross, P., and White, J. (2015a). Facies distribution of ejecta in analog tephra rings from experiments with single and multiple subsurface explosions. *Bulletin of Volcanology*, 77(8):66.

Graettinger, A., Valentine, G., Sonder, I., Ross, P., White, J., and Taddeucci, J. (2014). Maar-diatreme geometry and deposits: Subsurface blast experiments with variable explosion depth. *Geochemistry, Geophysics, Geosystems*, 15(3):740–764.

Graettinger, A. H., Valentine, G. A., and Sonder, I. (2015b). Circum-crater variability of deposits from discrete, laterally and vertically migrating volcanic explosions: experimental evidence and field implications. *Journal of Volcanology and Geothermal Research*, 308:61–69.

Gutmark, E., Schadow, K., and Wilson, K. (1989). Noncircular jet dynamics in supersonic combustion. *Journal of Propulsion and Power*, 5(5):529–533.

Hanagan, C., La Femina, P. C., and Rodgers, M. (2020). Changes in crater morphology associated with volcanic activity at telica volcano, nicaragua. *Geochemistry, Geophysics, Geosystems*, 21(7).

Harris, A. and Ripepe, M. (2007). Temperature and dynamics of degassing at stromboli. *Journal of Geophysical Research: Solid Earth*, 112(B3).

Hokenson, G. J. (1986). Thrust vector control utilizing asymmetric jet nozzles. *Journal of Spacecraft and Rockets*, 23(6):655–656.

Holasek, R. E., Self, S., and Woods, A. W. (1996). Satellite observations and interpretation of the 1991 mount pinatubo eruption plumes. *Journal of Geophysical Research: Solid Earth*, 101(B12):27635–27655.

James, M. R., Antoniazza, G., Robson, S., and Lane, S. N. (2020a). Mitigating systematic error in topographic models for geomorphic change detection: Accuracy, precision and considerations beyond off-nadir imagery. *Earth Surface Processes and Landforms*.

James, M. R., Carr, B., D'Arcy, F., Diefenbach, A., Dietterich, H., Fornaciai, A., Lev, E., Liu, E., Pieri, D., and Rodgers, M. (2020b). Volcanological applications of unoccupied aircraft systems (uas): Developments, strategies, and future challenges. *Volcanica*, 3(1):67–114.

James, M. R., Chandler, J. H., Eltner, A., Fraser, C., Miller, P. E., Mills, J. P., Noble, T., Robson, S., and Lane, S. N. (2019). Guidelines on the use of structure-from-motion photogrammetry in geomorphic research. *Earth Surface Processes and Landforms*, 44(10):2081–2084.

James, M. R., Lane, S. J., Chouet, B., and Gilbert, J. S. (2004). Pressure changes associated with the ascent and bursting of gas slugs in liquid-filled vertical and inclined conduits. *Journal of Volcanology and Geothermal Research*, 129(1-3):61–82.

Jessop, D. E., Gilchrist, J., Jellinek, A. M., and Roche, O. (2016). Are eruptions from linear fissures and caldera ring dykes more likely to produce pyroclastic flows? *Earth and Planetary Science Letters*, 454:142–153.

Jessop, D. E. and Jellinek, A. M. (2014). Effects of particle mixtures and nozzle geometry on entrainment into volcanic jets. *Geophysical Research Letters*, 41(11):3858–3863.

Johnson, J. B., Watson, L. M., Palma, J. L., Dunham, E. M., and Anderson, J. F. (2018). Forecasting the eruption of an open-vent volcano using resonant infrasound tones. *Geophysical Research Letters*, 45(5):2213–2220.

Keating, G. N., Valentine, G. A., Krier, D. J., and Perry, F. V. (2008). Shallow plumbing systems for small-volume basaltic volcanoes. *Bulletin of Volcanology*, 70(5):563–582.

Kelfoun, K., Harris, A., Bontemps, M., Labazuy, P., Chausse, F., Ripepe, M., and Donnadieu, F. (2020). A method for 3d reconstruction of volcanic bomb trajectories. *Bulletin of Volcanology*, 82(4):1–15.

Kieffer, S. W. (1984). Factors governing the structure of volcanic jets. *Explosive volcanism: inception, evolution, and hazards. National Academy, Washington*, pages 143–157.

Kieffer, S. W. (1989). Geologic nozzles. *Reviews of Geophysics*, 27(1):3–38.

Kieffer, S. W. and Sturtevant, B. (1984). Laboratory studies of volcanic jets. *Journal of Geophysical Research: Solid Earth*, 89(B10):8253–8268.

Komorowski, J.-C., Jenkins, S., Baxter, P. J., Picquout, A., Lavigne, F., Charbonnier, S., Gertisser, R., Preece, K., Cholik, N., and Budi-Santoso, A. (2013). Paroxysmal dome explosion during the merapi 2010 eruption: processes and facies relationships of associated high-energy pyroclastic density currents. *Journal of Volcanology and Geothermal Research*, 261:260–294.

Koyaguchi, T., Suzuki, Y. J., and Kozono, T. (2010). Effects of the crater on eruption column dynamics. *Journal of Geophysical Research: Solid Earth*, 115(B7).

Koyaguchi, T. and Woods, A. W. (1996). On the formation of eruption columns following explosive mixing of magma and surface-water. *Journal of Geophysical Research: Solid Earth*, 101(B3):5561–5574.

Kueppers, U., Huber, J., Schmid, M., Andronico, D., Johnson, J. B., Ripepe, M., Taddeucci, J., and Scarlato, P. (2019). Mind the gap: refined acoustic characterisation of explosions at stromboli volcano using drone-deployed sensors and near-field arrays. *AGUFM*, 2019:V23F–0273.

Kueppers, U., Perugini, D., and Dingwell, D. B. (2006a). "explosive energy" during volcanic eruptions from fractal analysis of pyroclasts. *Earth and Planetary Science Letters*, 248(3):800–807.

Kueppers, U., Scheu, B., Spieler, O., and Dingwell, D. B. (2006b). Fragmentation efficiency of explosive volcanic eruptions: A study of experimentally generated pyroclasts. *Journal of Volcanology and Geothermal Research*, 153(1):125–135.

Lacanna, G. and Ripepe, M. (2020). Modeling the acoustic flux inside the magmatic conduit by 3d-fdtd simulation. *Journal of Geophysical Research: Solid Earth*, 125(6):e2019JB018849.

Lacroix, A. (1904). *La Montagne Pelée et ses éruptions*. Masson.

Lagmay, M. A., Pyle, D. M., Dade, B., and Oppenheimer, C. (1999). Control of crater morphology on flow path direction of soufrière-type pyroclastic flows. *Journal of Geophysical Research: Solid Earth*, 104(B4):7169–7181.

Lavigne, F., Morin, J., Mei, E. T. W., Calder, E. S., Usamah, M., and Nugroho, U. (2017). *Mapping hazard zones, rapid warning communication and understanding communities: Primary ways to mitigate pyroclastic flow hazard*. Springer.

Layana, S., Aguilera, F., Rojo, G., Vergara, Á., Salazar, P., Quispe, J., Urra, P., and Urrutia, D. (2020). Volcanic anomalies monitoring system (volcanoms), a low-cost volcanic monitoring system based on landsat images. *Remote Sensing*, 12(10):1589.

Lherm, V. and Jellinek, A. M. (2019). Experimental constraints on the distinct effects of ash, lapilli, and larger pyroclasts on entrainment and mixing in volcanic plumes. *Bulletin of Volcanology*, 81(12):1–11.

Linstrom, P. and Mallard, W. (2000). *NIST Chemistry Webbook: NIST Standard Reference Database Number 69*, volume 20899. National Institute of Standards and Technology Technology, Gaithersburg MD.

Major, J. J., Pierson, T. C., Hoblittt, R. P., and Moreno, H. (2013). Pyroclastic density currents associated with the 2008-2009 eruption of chaitén volcano (chile): Forest disturbances, deposits, and dynamics. *Andean Geology*, 40(2):324–358.

Mattia, M., Rossi, M., Guglielmino, F., Aloisi, M., and Bock, Y. (2004). The shallow plumbing system of stromboli island as imaged from 1 hz instantaneous gps positions. *Geophysical Research Letters*, 31(24).

Mayer, K., Scheu, B., Gilg, H. A., Heap, M. J., Kennedy, B. M., Lavallée, Y., Letham-Brake, M., and Dingwell, D. B. (2015). Experimental constraints on phreatic eruption processes at whakaari (white island volcano). *Journal of Volcanology and Geothermal Research*, 302:150–162.

Mi, J., Nathan, G. J., and Luxton, R. E. (2000). Centreline mixing characteristics of jets from nine differently shaped nozzles. *Experiments in Fluids*, 28(1):93–94.

Montanaro, C., Scheu, B., Mayer, K., Orsi, G., Moretti, R., Isaia, R., and Dingwell, D. B. (2016). Experimental investigations on the explosivity of steam-driven eruptions: A case study of solfatara volcano (campi flegrei). *Journal of Geophysical Research: Solid Earth*, 121(11):7996–8014.

Moore, J. G. and Sisson, T. W. (1981). Deposits and effects of the may 18 pyroclastic surge. *US Geol. Surv. Prof. Pap*, 1250:421–438.

Neri, A., Esposti, O. T., Macedonio, G., and Gidaspow, D. (2003). Multiparticle simulation of collapsing volcanic columns and pyroclastic flow. *Journal of Geophysical Research: Solid Earth*, 108(B4).

Newman, S. and Lowenstern, J. B. (2002). Volatilecalc: a silicate melt–h2o–co2 solution model written in visual basic for excel. *Computers & Geosciences*, 28(5):597–604.

Niedzielski, T. (2018). Applications of unmanned aerial vehicles in geosciences: Introduction. *Pure and Applied Geophysics*, 175(9):3141–3144.

Ogden, D. E. (2011). Fluid dynamics in explosive volcanic vents and craters. *Earth and Planetary Science Letters*, 312(3):401–410.

Ogden, D. E., Glatzmaier, G. A., and Wohletz, K. H. (2008a). Effects of vent overpressure on buoyant eruption columns: implications for plume stability. *Earth and Planetary Science Letters*, 268(3-4):283–292.

Ogden, D. E., Wohletz, K. H., Glatzmaier, G. A., and Brodsky, E. E. (2008b). Numerical simulations of volcanic jets: Importance of vent overpressure. *Journal of Geophysical Research: Solid Earth*, 113(B2).

Oswatitsch, K. (1952). *Gasdynamik*. Springer-Verlag, Wien.

Papale, P., Moretti, R., and Barbato, D. (2006). The compositional dependence of the saturation surface of h2o+ co2 fluids in silicate melts. *Chemical Geology*, 229(1-3):78–95.

Parcheta, C. E., Pavlov, C. A., Wiltsie, N., Carpenter, K. C., Nash, J., Parness, A., and Mitchell, K. L. (2016). A robotic approach to mapping post-eruptive volcanic fissure conduits. *Journal of Volcanology and Geothermal Research*, 320:19–28.

Patrick, M. R., Harris, A. J. L., Ripepe, M., Dehn, J., Rothery, D. A., and Calvari, S. (2007). Strombolian explosive styles and source conditions: insights from thermal (flir) video. *Bulletin of volcanology*, 69(7):769–784.

Patrick, M. R., Swanson, D., and Orr, T. (2019). A review of controls on lava lake level: insights from halema ‘uma ‘u crater, kīlauea volcano. *Bulletin of Volcanology*, 81(3):13.

Peña Fernández, J. J., Cigala, V., Kueppers, U., and Sesterhenn, J. (2020). Acoustic analysis of starting jets in an anechoic chamber - implications for volcano monitoring. *Scientific Reports*.

Peña Fernández, J. J. and Sesterhenn, J. (2017). Compressible starting jet: pinch-off and vortex ring–trailing jet interaction. *Journal of Fluid Mechanics*, 817:560–589.

Rice, E. J. and Raman, G. (1993). Supersonic jets from bevelled rectangular nozzles. *ASME Winter Annu. Mtg.*

Ripepe, M., Donne, D. D., Harris, A., Marchetti, E., and Ulivieri, G. (2008). Dynamics of strombolian activity. *Washington DC American Geophysical Union Geophysical Monograph Series*, 182:39–48.

Rittmann, A. (1931). Der ausbruch des stromboli am 11 september 1930. *Zeitschrift für Vulkanologie*, 14:47–77.

Romero, J. E., Amin Doulillet, G., Vallejo Vargas, S., Bustillos Arequipa, J. E., Troncoso, L., Díaz Alvarado, J., and Ramón, P. (2017). Dynamics and style transition of a moderate, vulcanian-driven eruption at tungurahua (ecuador) in february 2014: pyroclastic deposits and hazard considerations. *Solid Earth*, 8:697–719.

Rosi, M., Bertagnini, A., and Landi, P. (2000). Onset of the persistent activity at stromboli volcano (italy). *Bulletin of volcanology*, 62(4-5):294–300.

Saad, M. A. (1985). Compressible fluid flow. *Englewood Cliffs, NJ, Prentice-Hall, Inc., 1985. 570 p.*

Saffaraval, F., Solovitz, S. A., Ogden, D. E., and Mastin, L. G. (2012). Impact of reduced near-field entrainment of overpressured volcanic jets on plume development. *Journal of Geophysical Research: Solid Earth*, 117(B5).

Salvatore, V., Silleni, A., Corneli, D., Taddeucci, J., Palladino, D. M., Sottili, G., Bernini, D., Andronico, D., and Cristaldi, A. (2018). Parameterizing multi-vent activity at stromboli volcano (aeolian islands, italy). *Bulletin of Volcanology*, 80(7).

Saunderson, H. C. (2008). Equations of motion and ballistic paths of volcanic ejecta. *Computers & geosciences*, 34(7):802–814.

Scharff, L., Hort, M., and Varley, N. (2015). Pulsed vulcanian explosions: A characterization of eruption dynamics using doppler radar. *Geology*, 43(11):995–998.

Schmid, M., Kueppers, U., Cigala, V., Sesterhenn, J., and Dingwell, D. B. (2020). Release characteristics of overpressurised gas from complex vents: implications for volcanic hazards. *Bulletin of Volcanology*, 82(11):1–12.

Schmid, M., Kueppers, U., Civico, R., Ricci, T., Taddeucci, J., and Dingwell, D. B. (2021). Characterising vent and crater shape changes at stromboli: implications for risk areas. *Volcanica*, 4(1):87–105.

Sherwood, A. E. (1967). Effect of air drag on particles ejected during explosive cratering. *Journal of Geophysical Research*, 72(6):1783–1791.

Sim, S. and Ogden, D. (2012). Effects of vent asymmetry on explosive eruptions. In *AGU Fall Meeting Abstracts*, volume V41B-2791.

Simons, B. C., Cronin, S. J., Eccles, J. D., Bebbington, M. S., and Jolly, A. D. (2020). Spatiotemporal variations in eruption style, magnitude and vent morphology at yasur volcano, vanuatu: insights into the conduit system. *Bulletin of Volcanology*, 82(8):1–22.

Solovitz, S. A., Ogden, D. E., Kim, D., and Kim, S. Y. (2014). Coupled fluid and solid evolution in analogue volcanic vents. *Journal of Geophysical Research: Solid Earth*, 119(7):5342–5355.

Sommerfeld, M. (1994). The structure of particle-laden, underexpanded free jets. *Shock waves*, 3(4):299–311.

Sparks, R., Wilson, L., and Hulme, G. (1978). Theoretical modeling of the generation, movement, and emplacement of pyroclastic flows by column collapse. *Journal of Geophysical Research: Solid Earth*, 83(B4):1727–1739.

Sparks, R. S. J. (2003). Forecasting volcanic eruptions. *Earth and Planetary Science Letters*, 210(1):1–15.

Spieler, O., Kennedy, B., Kueppers, U., Dingwell, D. B., Scheu, B., and Taddeucci, J. (2004). The fragmentation threshold of pyroclastic rocks. *Earth and Planetary Science Letters*, 226(1-2):139–148.

Suzuki, Y. J., Costa, A., and Koyaguchi, T. (2020). Control of vent geometry on the fluid dynamics of volcanic plumes: insights from numerical simulations. *Geophysical Research Letters*, 47(10).

Taddeucci, J., Alatorre-Ibargüengoitia, M. A., Cruz-Vázquez, O., Del Bello, E., Scarlato, P., and Ricci, T. (2017). In-flight dynamics of volcanic ballistic projectiles. *Reviews of Geophysics*, 55(3):675–718.

Taddeucci, J., Palladino, D. M., Sottili, G., Bernini, D., Andronico, D., and Cristaldi, A. (2013a). Linked frequency and intensity of persistent volcanic activity at stromboli (italy). *Geophysical research letters*, 40(13):3384–3388.

Taddeucci, J., Scarlato, P., Capponi, A., Del Bello, E., Cimarelli, C., Palladino, D. M., and Kueppers, U. (2012). High-speed imaging of strombolian explosions: The ejection velocity of pyroclasts. *Geophysical Research Letters*, 39(2).

Taddeucci, J., Valentine, G. A., Sonder, I., White, J. D. L., Ross, P., and Scarlato, P. (2013b). The effect of pre-existing craters on the initial development of explosive volcanic eruptions: An experimental investigation. *Geophysical Research Letters*, 40(3):507–510.

Toyos, G. P., Cole, P. D., Felpeto, A., and Marti, J. (2007). A gis-based methodology for hazard mapping of small volume pyroclastic density currents. *Natural Hazards*, 41(1):99–112.

Tsuji, Y., Morikawa, Y., and Shiomi, H. (1984). Ldv measurements of an air-solid two-phase flow in a vertical pipe. *Journal of Fluid Mechanics*, 139:417–434.

Turner, N., Houghton, B., Taddeucci, J., von der Lieth, J., Kueppers, U., Gaudin, D., Ricci, T., Kim, K., and Scarlato, P. (2017). Drone peers into open volcanic vents. *Eos*.

Valade, S., Lacanna, G., Coppola, D., Laiolo, M., Pistolesi, M., Delle Donne, D., Genco, R., Marchetti, E., Ulivieri, G., and Allocca, C. (2016). Tracking dynamics of magma migration in open-conduit systems. *Bulletin of Volcanology*, 78(11):78.

Valentine, G. A. (1997). Eruption column physics. *No. LA-UR-97-83; CONF-970160-1.*

Valentine, G. A., White, J. D., Ross, P.-S., Amin, J., Taddeucci, J., Sonder, I., and Johnson, P. J. (2012a). Experimental craters formed by single and multiple buried explosions and implications for volcanic craters with emphasis on maars. *Geophysical Research Letters*, 39(20).

Valentine, G. A., White, J. D. L., Ross, P., Amin, J., Taddeucci, J., Sonder, I., and Johnson, P. J. (2012b). Experimental craters formed by single and multiple buried explosions and implications for volcanic craters with emphasis on maars. *Geophysical Research Letters*, 39(20).

Vallance, J. W., Schneider, D. J., and Schilling, S. P. (2008). *Growth of the 2004–2006 lava-dome complex at Mount St. Helens, Washington*, volume 1750, pages 169–207. US Geological Survey Professional Paper 1750.

Vanderkluysen, L., Harris, A. J. L., Kelfoun, K., Bonadonna, C., and Ripepe, M. (2012). Bombs behaving badly: unexpected trajectories and cooling of volcanic projectiles. *Bulletin of Volcanology*, 74(8):1849–1858.

Viccaro, M., Cannata, A., Cannavò, F., De Rosa, R., Giuffrida, M., Nicotra, E., Petrelli, M., and Sacco, G. (2021). Shallow conduit dynamics fuel the unexpected paroxysms of stromboli volcano during the summer 2019. *Scientific Reports*, 11(1):1–15.

Wallace, P. J., Plank, T., Edmonds, M., and Hauri, E. H. (2015). *Volatiles in magmas*, pages 163–183. Elsevier.

Washington, H. S. (1917). Persistence of vents at stromboli and its bearing on volcanic mechanism. *Bulletin of the Geological Society of America*, 28(1):249–278.

Williams, G. T., Kennedy, B. M., Wilson, T. M., Fitzgerald, R. H., Tsunematsu, K., and Teissier, A. (2017). Buildings vs. ballistics: Quantifying the vulnerability of buildings to volcanic ballistic impacts using field studies and pneumatic cannon experiments. *Journal of Volcanology and Geothermal Research*, 343:171–180.

Wilson, L. (1972). Explosive volcanic eruptions-ii the atmospheric trajectories of pyroclasts. *Geophysical Journal International*, 30(4):381–392.

Wilson, L. and Head, J. W. (1981). Ascent and eruption of basaltic magma on the earth and moon. *Journal of Geophysical Research: Solid Earth*, 86(B4):2971–3001.

Wilson, L., Sparks, R. S. J., and Walker, G. P. (1980). Explosive volcanic eruptions—iv. the control of magma properties and conduit geometry on eruption column behaviour. *Geophysical Journal International*, 63(1):117–148.

Woods, A. W. (1988). The fluid dynamics and thermodynamics of eruption columns. *Bulletin of Volcanology*, 50(3):169–193.

Woods, A. W. (1995). A model of vulcanian explosions. *Nuclear Engineering and Design*, 155(1):345–357.

Woods, A. W. (2010). Turbulent plumes in nature. *Annual Review of Fluid Mechanics*, 42:391–412.

Woods, A. W. and Bower, S. M. (1995). The decompression of volcanic jets in a crater during explosive volcanic eruptions. *Earth and Planetary Science Letters*, 131(3):189–205.

Woods, A. W. and Caulfield, C. P. (1992). A laboratory study of explosive volcanic eruptions. *Journal of Geophysical Research: Solid Earth*, 97(B5):6699–6712.

Yamaoka, K., Geshi, N., Hashimoto, T., Ingebritsen, S. E., and Oikawa, T. (2016). Special issue "the phreatic eruption of mt. ontake volcano in 2014". *Earth, Planets and Space*, 68(1):1–8.

Yin, S., Meyer, M., Li, W., Liao, H., and Lupoi, R. (2016). Gas flow, particle acceleration, and heat transfer in cold spray: a review. *Journal of Thermal Spray Technology*, 25(5):874–896.

Zanon, V., Neri, M., and Pecora, E. (2009). Interpretation of data from the monitoring thermal camera of stromboli volcano (aeolian islands, italy). *Geological Magazine*, 146(4):591–601.

Zorn, E. U., Walter, T. R., Heap, M. J., and Kueppers, U. (2020a). Insights into lava dome and spine extrusion using analogue sandbox experiments. *Earth and Planetary Science Letters*, 551:116571.

Zorn, E. U., Walter, T. R., Johnson, J. B., and Mania, R. (2020b). Uas-based tracking of the santiaguito lava dome, guatemala. *Scientific Reports*, 10(1).

Danksagung

Ulli, I can not thank you enough for all that you have done. You got me hooked on volcanoes during the Bachelor thesis, you helped me organizing field work to Etna during my time in Bremen and you supported and encouraged me when I tried to come back to Munich for a PhD. Thank you for all the advice, discussions and the help during the last years. You have been a huge inspiration and I learned a lot from you! And thank you for providing me with the opportunity to achieve a bucket list item: Flying drones on a volcano!

Thank you Don, for your support and your open door when I needed your advice. Thank you for your input as a Co-Author, your comments always drastically improved the manuscripts. Also, I am really grateful that you provided the opportunity for me to work here after my proposals were unsuccessful. Thank you Vale, without your work my research would not have been possible. You were always available and ready to give great advice!

I would like to thank Corrado and Caron for bringing me along for fieldwork and for giving me a glimpse into the field of volcanic lightning. Thanks to my coffice mates Pancho and Christina it was a great pleasure to share the office with you. A big thank you to my PhD fellows and colleagues for UFO lunches, coffee breaks and balcony breaks: Pancho, Christina, Ana, Daniel, Lukas, Jérémie, Cristian, Mathieu, Caron, Sid, Joanna, Zeynep, Steffi, Diana, Kai, Iphi, Adrian, Arianna, and all those that I am forgetting right now. Thank you Betty for your advice and thanks to Margot, Rike and Rosa for keeping everything running smoothly. Thanks to all of the LMU staff for providing such a pleasurable work environment.

Thanks to the colleagues of INGV for organizing the BAcIO campaigns and the great collaboration. Field work with you is always great! I also want to thank Florian and Fabian for bringing me to Stromboli for the first time and for providing me with the best side hustle imaginable.

Vielen Dank an meine Freunde, die mich seit vielen, vielen Jahren begleiten: Jona, Chris, Rita, Maria, Michi, Totti, Stefan und Flo. Danke für die unzähligen gemeinsamen Stunden und dafür, dass ihr eine Konstante in meinem Leben seid! Cati, danke für deine Unterstützung und danke, dass du so bist, wie du bist.

Zu guter Letzt möchte ich meiner Familie danken. Ein rießiges Dankschön an meine Eltern, für ihre unendliche Geduld und für die Freiheit die sie mir ermöglicht haben. Ohne euch wäre ich nie so weit gekommen. Vielen Dank auch an meine Schwester und meine Großeltern. Durch euch ist mein Leben bis jetzt immer unbeschwert und glücklich gewesen.